University of Nottingham
UK | CHINA | MALAYSIA

High-performance, multifunctional flexible electronic devices

Thesis submitted to University of Nottingham for the degree of

Doctor of Philosophy, July 2023.

Jin Xu, Meng, BEng

Supervised by

Guang Zhu

Mengxia Xu

George Chen

ABSTRACT

Wearable sensing electronics capable of detecting and differentiating multiple mechanical stimuli are critical and promising devices in the applications of healthcare monitoring, robotics, and human-machine interface. Compared with commercial wearable electronic devices features with rigid and discomfortable, the flexible, stretchable, ultrathin, attachable and wearable sensors are more desirable to attach to human skin. Based on different working mechanisms, wearable sensors can generally be divided into resistive, capacitive, piezoelectric and triboelectric types. Among these pressure sensors, piezoresistive sensors which transfer mechanical information into resistance variation, have multiple advantages, including high sensing performance, low energy consumption, ease of device assembly, simple signal acquisition, etc. There are a lot of piezoresistive pressure sensors developed by many fabrication methods, such as the template method, 3D printing, etc.; however, most of the developed sensors suffer from low sensitivity and poor linearity over a broad range. Although a lot of strategies are reported to improve the sensitivity and sensing range, such as fabricating micro/nano structure, porous structure, hierarchical structure, etc., the piezoresistive pressure sensor fabricated by these methods still can’t achieve a high sensitivity and broad linear sensing range simultaneously. Hence, there is a strong need to develop a method to fabricate a piezoresistive pressure sensor with both high sensitivity and broad linear sensing range. In addition, most existing types of wearable sensors are designed and optimized for detecting only uniaxial

mechanical stimuli and cannot monitor and differentiate multiple mechanical stimuli, which severely hinders their use in real-world applications, which always involve very complex mechanical stimuli. The sensing features of these sensors present the same electrical output trend under different mechanical stimuli such as pressure, stretching, bending and twisting. As a result, the measurement of one directional mechanical stimulus will be interfered by mechanical stimuli coming from other directions, indicating the inability to sense and differentiate between multiple mechanical stimuli. Thus, it is necessary to develop a multifunctional wearable sensor capable of detecting and differentiating multiple mechanical stimuli including pressure, stretching, convex and concave bending.

Firstly, a hierarchical in-situ filling porous piezoresistive sensor (HPPS) is fabricated by direct ink writing (DIW) printing and curing of carbon nanofibers (CNFs)/polydimethylsiloxane (PDMS) emulsion template method. Hierarchical porous geometry significantly increases the contact area, distributes stress to multilayered lattice and internal porous structure, resulting in a broad sensing range. Moreover, unlike conventional hollow porous structure, the in-situ filling porous structure is formed by the solidification of CNFs/PDMS and evaporation of emulsified water, while the CNFs dispersed in emulsified water remain inside the pores, forming CNFs networks embedded in the pores. The CNFs networks in-situ filling porous structure generates more contact sites and conductive pathways during compression, thereby achieving high sensitivity and linearity over the entire sensing range. Therefore, the optimized HPPS achieves high sensitivity (4.7 kPa^{-1}) and

linearity (coefficient of determination, R^2 = 0.998) over a broad range (0.03–1000 kPa), together with remarkable response time and repeatability. Benefiting from its high sensitivity and broad linear sensing range, the prepared sensor also exhibits high pressure resolution. Then the sensor is demonstrated in detecting various stimuli from low pressure, such as pulse detection, voice recognition, to high pressure, such as human foot motion and tire pressure detection.

Secondly, a wing-like structure with a pressure sensing module in the middle and stretching sensing module in both wings is fabricated with the capability of detecting and differentiating multiple mechanical stimuli, including pressure, stretching, and convex and concave bending. The wing-like multifunctional sensor (WMS) is designed with a hierarchical in situ filling porous structure as the pressure sensing layer and wrinkled CNTs/Ag nanoflakes hybrid film as stretch sensing layer, resulting in excellent pressure and stretch sensing performance. When measuring the pressure, the signal of the pressure sensing module is not interfered by the external stretching because the lower Young's modulus stretch sensing module in both wings bears all the stretch without deforming the pressure sensing module. In stretch sensing, the response of the stretch sensing module will not be disturbed by external normal pressure because of the higher thickness and high compressibility of the hierarchical porous sensing layer that withstands the entire pressure. In addition, the WMS sensor could detect and differentiate convex and concave bending based on the breakage and overlap of the CNTs/Ag nanoflakes in the stretch sensing module. Then WMS is demonstrated for accurately detecting of human kinesthesia, recognizing various types

and sizes of objects with a robotic gripper, monitoring locomotion and perceiving environmental information by a crawling robot, and human-machine interaction.

In summary, we developed a high sensing performance piezoresistive pressure sensor with high sensitivity over a broad linear sensing range by 3D printing technique and the emulsion template method. We reported a multifunctional sensor with the capability to detect and differentiate multiple mechanical stimuli by a wing-like structure with a mismatch of Young's modules and thickness between the pressure and stretch sensing module. The developed sensor is demonstrated in the applications of health monitoring, human motion recognition, robotic and human-machine interface.

ACKNOWLEDGEMENTS

First and foremost, I want to send my most sincere respect and thanks to my first advisor, Prof. Guang Zhu, for all the support and guidance he provided in my Ph.D. research. In the past four years, he has spent countless hours helping and supporting my research, discussing and giving suggestions for my project, revising my paper, etc. I am always motivated and inspired by his enthusiasm for the research, deep thoughts about the problem, hardworking to the working, etc. I would like to express my sincere gratitude to Prof. Mengxia Xu, who is my second supervisor. He discussed research topics with me regularly and provided me with a lot of suggestions for my research. I would like to express my deep gratitude to my external assessor, Prof. Zhaolin Li, and my internal assessor, Prof. Bo Li. They provided me with a lot of instructions, guidance and suggestions for my thesis.

I want to send my deeply gratitude to Dr. Huayang Li, who spent so much time and effort to help my research, teach my experiment skills, discuss my research, give suggestions for my paper, etc. I would like to express my heartfelt thanks to my labmates: Dr. Chen Zhang, Dr. Fei Liang, Dr. Xin Li, Dr. Shu Liu, Dr. Yiming Yin, Dr. Jinwei Cao, Hanfang Feng, Chunlin Luo, Gang Yang and Jianchen Lai, for teaching me experimental skills, discussing experiment results with me, supporting my research, and providing guidance for life in the past four years.

I would like to thank Prof. Guang Zhu and Yisi Lu for providing me the opportunity to be an intern at LuxCreo Inc. and YONGJIANG Laboratory. I learned a

lot of knowledge and got a lot of experimental skills and work experience. I am very happy and thankful to meet some colleagues, Yanhui Guo, Hu Wang, Zhongming Ye, Dr. Menglong Hu, Jie Gao, Lili Ling, Dr. Wen Fan, and Jie Chen, for their continuous help and support to my project. I would like to thank all the hard work of my summer interns: Binran Zhang, Shuinan Liu, Hao Tan, Fanyuan Xiao and luohaoran Wang for their time and effort.

Lastly, I want to give thanks to my family from the bottom of my heart. My parents always provide me with unconditional and endless love. I can always find ease, happiness and peace with them. I deeply thank my wife, Wandi Bao, who is always by my side and enlightens me when I feel upset. She always patiently guides and helps me, and she always gives me the biggest courage to overcome any problems.

Table of Contents

Chapter 1. Introduction

1.1 Research background

Wearable electronic devices refer to the devices that are designed to be worn on human body and provide intelligent assistance, including detecting, analyzing, transmitting and processing information or data to the wearer.[1,2] However, most commercial wearable electronic devices, such as watches, wristbands, or belts, are fabricated by fully or partly integrating bulk and rigid conventional electronic components. These rigid commercial wearable electronic devices feature discomfortable, poor conformal and adhesion properties that limit their application in wearable scenarios.[3] In addition, the mismatch of physical properties at the electronic-skin interface creates huge challenges in the development of next-generation, skin-integrated electronics.[4] Inspired by human skin's capability to perceive surroundings, such as object shape, texture, hardness, temperature, and humidity, wearable flexible electronic devices have attracted increasing attention. Compared to traditional rigid and bulk electronic devices, wearable flexible electronic devices have a lot of advantages, such as being ultra-thin, lightweight, flexible, stretchable, biocompatible and breathable, which make them more suitable to equip on the human body.

There are a lot of reports about different types of wearable flexible electronics, such as stretchable electronics, implant electronics, temperature sensors, electrochemical sensors, wearable self-power systems, etc., as shown in Figure 1.1. Flexible wearable sensing electronics with the capacity of transducing multiple mechanical stimuli into

electric signals have attracted tremendous interest. Typically, flexible wearable sensors are categorized into four types based on the sensing mechanism: piezoresistive type,[5,6] capacitive type,[7,8] piezoelectric type [9,10] and triboelectric type.[11,12] Among various types of flexible wearable sensors, resistive types of wearable sensors have multiple advantages, including ease of device fabrication, low energy consumption, simple signal acquisition, etc. The resistive types of sensors refer to the sensors that transfer mechanical stimuli, including pressure, stretching, bending and twisting, into resistance variation.

Figure 1.1 Summarized key properties of advanced wearable electronic devices.[3]

For steadily and accurately perceiving physical signals, a series of significant progress has been made in developing high-performance wearable sensors with high stretchability,[13,14] robustness,[15,16] fast response, low detect limitation,[17,18] etc.[19,20] However, most published resistive types of sensors suffer from poor sensing performance, specializing in sensitivity and sensing range. To be widespread in more application scenarios, the ideal pressure sensors require high sensitivity and high linearity over a broad sensing range.

Another important challenge of flexible and wearable electronic devices is the

difficulty of detecting and distinguishing multiple mechanical stimuli, including stretch, pressure and bending. For most of the developed wearable sensors, they are optimized for detecting only uniaxial mechanical deformation (such as lateral stretch or pressure) and cannot monitor and differentiate multiple mechanical stimuli. Under different mechanical stimuli, such as pressure, stretching, bending, and twisting, these sensors exhibit similar electrical output tendencies. Because of this, one direction of mechanical stimulus will be interfered with by other directions of mechanical stimulus, indicating an inability to distinguish between them. This severely limits its use in practical applications where the detection and differentiation of a variety of complex mechanical stimuli are essential. Thus, there is strongly needed to develop a multifunctional flexible and wearable sensor with the capabilities to detect and differentiate multiple mechanical stimuli.

1.2 Aims and objectives

The main aims and objectives of this research involve:

(a) Fabrication and optimization of hierarchical in-situ filling porous piezoresistive sensor

(b) Electromechanical characterization and mechanism studies of HHPS

(c) Applications of HPPS in diverse pressure scenarios and healthcare monitoring

(d) Fabrication and optimization of wing like multifunctional resistive sensor

(e) Electromechanical characterization of the pressure and stretching sensing module

of WMS and study of multiple mechanical stimuli differentiating sensing mechanism

(f) Applications of WMS in monitoring human kinesthesia, robotics and human-machine interaction.

1.3 Thesis Structure

Chapter 1 introduces the background, research aims and objectives.

Chapter 2 is a literature review of the different types of flexible sensing electronic devices: capacitive type, piezoelectric type, triboelectric type, and resistive type. Different applications of flexible sensing electronic devices. The literature review of multifunctional sensors for detecting multiple mechanical stimuli.

Chapter 3 introduces the fabrication process of HPPS and the fabrication parameter optimization of the sensing layer in HPPS.

Chapter 4 evaluates the electromechanical performance of HPPS and explores its potential applications in health monitoring, high-pressure resolution demonstration.

Chapter 5 introduces the fabrication process of WMS and the fabrication parameter optimization of the pressure and stretch sensing module in WMS.

Chapter 6 evaluates the electromechanical performance of WMS and demonstrates its in accurate detection of body kinesthesia, recognition of different types and sizes of objects by a WMS-integrated robotic gripper, locomotion monitoring and environment perception by a WMS-integrated crawling robot, and human-machine interaction.

Chapter 7 is the conclusion of the thesis and future expectations.

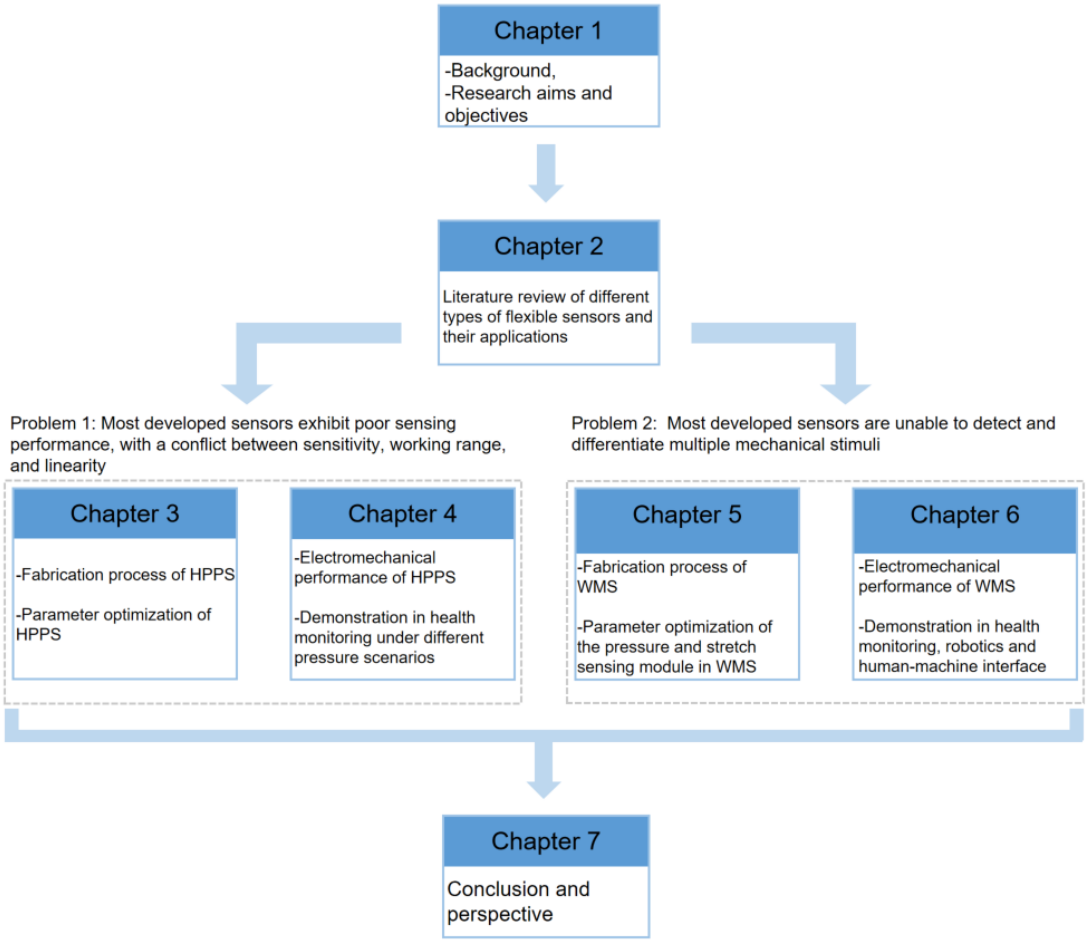

Figure 1.2 Thesis structure.

Chapter 2. Literature review

2.1 Overview

Flexible wearable sensors are a class of wearable electronic devices that can detect external mechanical stimuli such as pressure, tension, vibration, bending and shear, and convert these mechanical signals or mechanical deformations into electrical signals. The flexible, ultrathin, lightweight, small and portable wearable sensor can conformally attach to the surface of any shape of object, especially human skin. According to the different working mechanisms, flexible wearable flexible mechanical sensitive sensors can be divided into four main types, including resistive, capacitive, piezoelectric and triboelectric nanogenerators. The resistive type of sensor has the advantages of ease of device fabrication, low energy consumption, and simple signal acquisition. The resistive type of sensor is designed and developed for different types of sensors, including strain resistive sensors, piezoresistive sensors, and bending resistive sensors, based on the different working scenarios. The piezoresistive sensor, as one of the most common resistive types of sensors, has attracted tremendous attention, and there are a lot of reports about optimizing the high sensing performance of piezoresistive sensors through material selection and structure design. However, most of the single functional resistive types of sensors, such as piezoresistive sensor and strain resistive sensor cannot differentiate the multiple mechanical stimuli from different directions, which severely limits their application. Thus, there are also some reports about developing a multifunctional sensor capable of detecting and differentiating multiple mechanical stimuli.

2.2 Sensing mechanisms and classification of flexible wearable sensor

The flexible wearable sensor is the electronic device that detects the electric signal such as resistance, capacitance, voltage, etc. in response to different types of mechanical stimuli such as pressure, stretch, bending and twisting. According to the different sensing mechanisms and measured electric signal, the commonly flexible wearable sensor can be divided into resistive sensor, capacitive sensor, piezoelectric sensor, and triboelectric nanogenerator (Figure 2.1). Each type of sensor can also be divided into different kinds of sensors that are used to detect different mechanical stimuli, such as pressure sensor, stretch strain sensor, bending sensor, etc. In all these types of sensors, the geometry design of the active layer and the functional material selection have significant effects on the sensing performance (Figure 2.2).

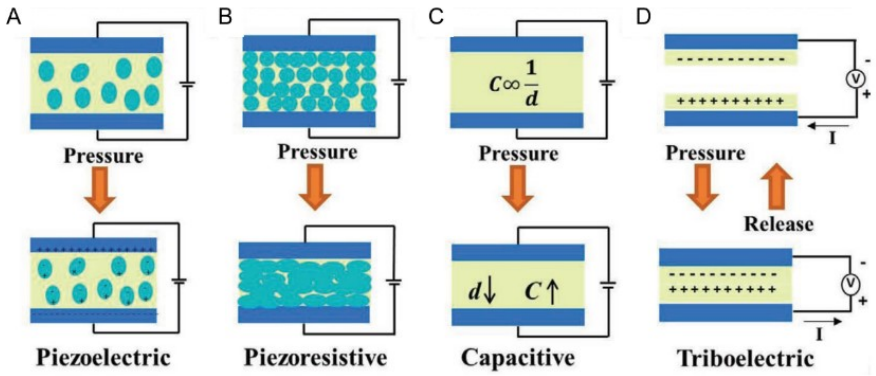

Figure 2.1 Schematic diagrams of pressure sensors based on different working mechanisms: (A) piezoelectric, (B) piezoresistive, (C) capacitive, and (D) triboelectric-based sensors. [21]

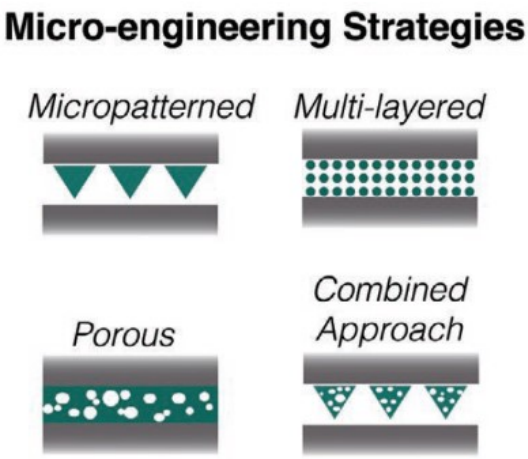

Figure 2.2 Microengineering is used to improve the sensing performance of wearable sensors.[21]

2.2.1 Capacitive sensor

Flexible capacitive sensor is the type of sensor that detects mechanical signals such as pressure and stress through the changes in capacitance. As one most commonly capacitive sensors, the parallel plate capacitive sensor is characterized by two planar electrodes on the upper and lower sides, sandwiching the dielectric layer in the middle. The mechanical deformation in the spatial structure between the two electrodes caused by external stress, stretch or bending leads to a change in capacitance. The capacitance of a parallel plate capacitor can be calculated by the formula (1):

$$C = \frac{\varepsilon_r \varepsilon_0 A}{d}$$

where C is the capacitance, A is the overlapping area between the two electrodes or the effective area of the capacitor, ε_0 is the permittivity of free space, ε_r is the relative permittivity of the dielectric material between the two plates, and d is the distance

between the two electrodes. The capacitance depends on the spacing between the two plates, contact surface, and effective dielectric constant affected by deformation under mechanical stimuli. When external stretch or compressive strain is applied to the sensor, S or d changes, resulting in a change in capacitance, which can reflect the magnitude of the pressure or stretch.

Flexible capacitive sensors have several advantages. From a performance point of view, they exhibit high sensitivity, stable sensing performance, good dynamic response and fast response time, which can detect extremely small static force. Moreover, capacitive pressure sensors have low power consumption and can be made temperature independent.[21] However, capacitive pressure sensors have high hysteresis from unstructured rubber dielectrics due to their viscoelastic nature. Capacitive pressure sensors are susceptible to external noise sources from electromagnetic waves and high hysteresis due to their viscoelasticity, from unstructured rubber dielectric. Although the capacitive pressure sensor has good sensing linearity, its sensing range is relatively narrow.

Proper material selection can enable capacitive sensors to achieve high sensing functionality such as broad sensing range, high stretchability, good sensing linearity, and faster response and recovery times.[22] Various conductive materials and composites have been developed as parallel electrode materials for capacitive sensors, including Au film, Ag NWs, Ag NPs, CNTs, graphene, MXene nanosheets, PEDOT: PSS, and ionically conductive hydrogel. Different types of low-modulus dielectric materials, such as polyvinylidene fluoride (PVDF), Ecoflex, polydimethylsiloxane

(PDMS), polyurethane (PU), and ionic liquid or gels (1-ethyl-3-methylimidazolium trifluoromethanesulfonate ([EMIM][OTF]), PVA/H_3PO_4), have been developed as dielectric media. According to different sensing scenarios, capacitive sensor is generally divided into pressure and stretch types of capacitive sensor, and the research on these two kinds of capacitive sensor is reviewed in chapter 2.2.2.1 and 2.2.2.2.

2.2.1.1 Capacitive pressure sensor

As one of the most common mechanical stimuli, pressure is measured by the capacitive pressure sensor caused by the change of distance between the two electrodes. The sensitivity of a capacitive sensor is defined as formula (2):[23]

$$S = \frac{\Delta C / C_0}{\Delta P}$$

where S represents sensitivity, ΔC is the change in capacitance, C_0 is the initial capacitance when no pressure is applied, and ΔP represents the applied pressure.

There are a lot of reports about improving the sensing performance of the capacitive pressure sensor. A typical approach to improve the sensing performance is to manipulate the geometry of the pressure-sensitive materials to enhance the compressibility of the dielectric layer. Several microengineering designs have been implemented for different applications, including porous layers, micropatterned structures, multi-layered structures and combination methods. Bao et al. reported micropatterning pyramid PDMS dielectrics by molding a surface topology into the PDMS films, which has been demonstrated to improve sensitivity by over 30 times

compared to non-patterned PDMS layers of equivalent dimensions (Figure 2.3A).[24] As shown in Figure 2.3B, a capacitive sensor with a tilted micropillar array-structured dielectric layer was developed by Lu et al. The tilted micropillars undergo bending deformation rather than compression deformation; the distance between the electrodes is easier to change, thus resulting in high pressure sensitivity (0.42 kPa^{-1}) and very small detection limit (1 Pa).[25] Beside fabricating the micropatterning structure in dielectric layer, there is also some research about fabricating the microstructures on the electrode. Compared with planar electrodes, micropatterned electrodes can improve compressibility under the same external pressure. Several micropattern structures have been used in capacitive pressure sensors, including microtowers, microdomes, wrinkled line patterns, and cylinder shapes. As shown in Figure 2.3C, Wong et al. developed a highly sensitive flexible capacitive pressure sensor with micro-array PDMS electrode and PVDF as the dielectric layer. The microarray electrode causes a significant increase in effective permittivity and the change of the distance between electrodes under pressure, which results in excellent pressure sensitivity of 2.94 kPa^{-1} (0−2 kPa) and 0.75 kPa^{-1} (2−6.7kPa) as well as an ultralow low detection limit (< 3 Pa).[26] Besides the micropatterned structures, porous layers is another main structure to improve the sensing performance. A droplet-based microfluidic assisted emulsion self-assembly technique was used to fabricate a 3D microstructured PDMS layer that is utilized to fabricate high-performance capacitive pressure sensor, according to Park et al. (Figure 2.3D).[27] The micropore size can be controlled by adjusting the flow rates of the oil-water solutions. These porous

structure capacitive sensors exhibit relatively high sensitivity (0.86 kPa^{-1}) and spatial uniformity. In recent years, the combination of different approaches to fabricating a hierarchical structure has been proven to further improve the sensing performance of the capacitive pressure sensor. As shown in Figure 2.3E, Guo et al. reported an intrafillable microstructure which significantly improves the sensitivity and broadens the pressure response range. The intrafillable microstructures feature undercuts and grooves that accommodate deformed surface microstructures, effectively enhancing the structural compressibility and the pressure-response range.[7] The capacitive sensor with the intrafillable microstructure exhibits an unprecedentedly high sensitivity ($S > 220\ kPa^{-1}$) over a broad pressure regime (0.08 Pa–360 kPa). As shown in Figure 2.3F, Zhou et al. developed a novel hybrid dielectric consisting of micro-cilia array with a low-permittivity (low-k), a rough surface with high permittivity (high-k), and micro-dome array. The gradient compressibility of hybrid dielectrics enabled linear behavior of elastic modulus with pressure, which results in a ultrawide linearity range up to 1000 kPa and a high sensitivity of 0.314 kPa^{-1}.[8]

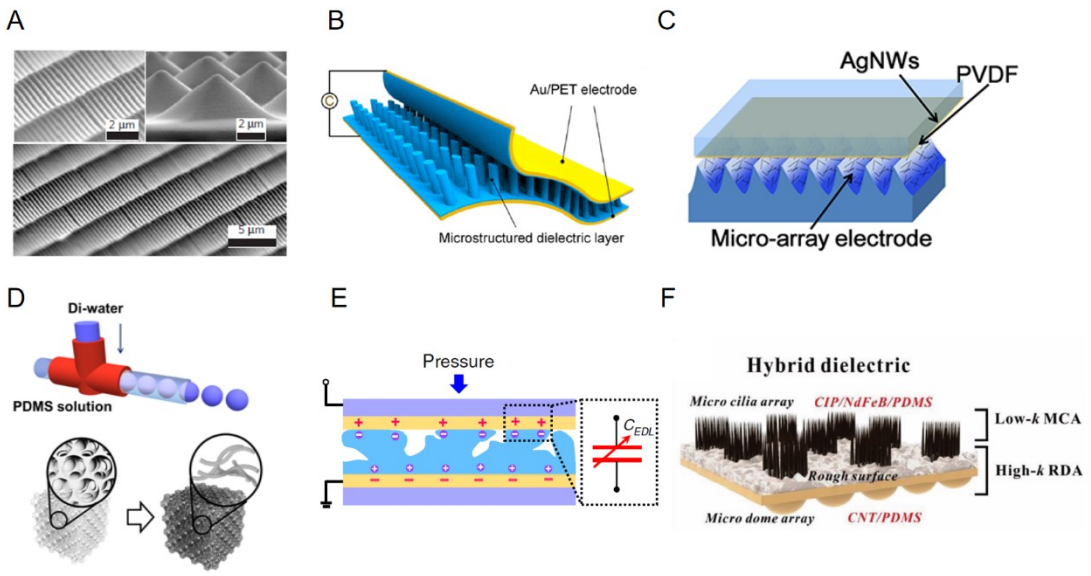

Figure 2.3 (A) SEM images of the microstructured pyramid PDMS films.[24] (B) Schematic illustration of the capacitive pressure sensor.[25] (C) Schematic of capacitive pressure sensor with the microarray PDMS bottom electrode embedded with AgNWs.[26] (D) Schematic of 3D microstructured PDMS fabrication by droplet-based microfluidic assisted emulsion self-assembly.[27] (E) Schematic illustration of the graded intrafillable architecture iontronic pressure sensor.[7] (F) Schematic illustration of the structure and features of bio-inspired hybrid dielectric.[8]

2.2.1.2 Capacitive stretch sensor

Beside the capacitive pressure sensor, another commonly studied capacitive stretch sensor has attracted tremendous attention. When stretched, a capacitive sensor maintains a change in capacitive area, and a reduction in the thickness of the dielectric layer results in an increase in capacitance. The initial capacitance is given by following equation (3):

$$C_0 = \varepsilon_r \varepsilon_0 \frac{l_0 w_0}{d_0}$$

where l_0 and w_0 is the initial length and width of the parallel plate. When the capacitive sensor is stretched to a strain ε, the length of the capacitive sensor increases to $(1+\varepsilon)l_0$, the width of dielectric layer decreases to $(1-v_{electrode})w_0$, the thickness of the dielectric layer decreases to $(1-v_{dielectric})d_0$, where the $v_{electrode}$ and $v_{dielectric}$ are the Poisson's ratios for the stretchable electrodes and dielectric layer, respectively. In addition, the electrode and dielectric layer are usually assumed to have the same Poisson's ratio. Then, the capacitance under stretching is calculated as follows (4):[28,29]

$$C = \varepsilon_r \varepsilon_0 \frac{(1+\varepsilon) l_0 (1 - v_{electrode}) w_0}{(1 - v_{dielectric}) d_0} = \varepsilon_r \varepsilon_0 \frac{(1+\varepsilon) l_0 w_0}{d_0} = (1+\varepsilon) C_0$$

The sensitivity of capacitive stretch sensor is defined as the gauge factor in the following equation (5):

$$\mathrm{GF} = \frac{\Delta C / C_0}{\varepsilon}$$

The GF value is highly related to the material selection and micro/nano structure of the capacitive sensor. For capacitive stretch sensor, the main problem is that traditional metal electrodes cannot undergo large stretch deformations. Thus, there have been a lot of studies about the electrode layer's capability to sustain large deformations.[30] The wave/wrinkle/buckling structure of the electrode layer can endow the hard metal electrodes with the capability to bear the deformation. As shown in Figure 2.4A, Someya et al. reported a capacitive strain sensor utilizing an ultrathin wrinkled gold film electrode, which was generated by transferring ultrathin gold film electrodes to the top and bottom of a prestretched adhesive dielectric layer. With this

wrinkled structure design, the capacity strain sensor achieves a gauge factor of 3 and negligible hysteresis over a high linearity range with strain of 140%.[31] However, the wrinkle structure could only stretch along the direction of fold, which cannot stretch in other directions. Then the serpentine structure is developed, which is able to bear biaxial strain or even distortion. As shown in Figure 2.4B, Pan et al. fabricated a PDMS/Ag/Ecoflex/Ag/PDMS sandwich-structured sensor array composed of PET-based Ag serpentine-shaped electrodes, which possesses impressive stretchability, low detection limitation and fast response. Through monitoring the capacitance changes of the sensor array, a linear response to external pressures is derived based on the capacitive sensing mechanism.[32] Then the 2D mesh structure was developed by orthogonally aligning the serpentine electrodes, which further improves the stretchability in different directions. A skin-inspired stretchable matrix network as a multi-sensory e-skin was developed by Wang et al. (Figure 2.4C). The matrix network structure has 100 winding wires connecting the sensing nodes to achieve multifunctional sensing capabilities.[33] The capacitive sensor based on textile/woven fiber structure has many advantages, such as ductility, mechanical toughness, breathability, softness, and comfort. As shown in Figure 2.4D, Cooper et al. injected liquid metal into hollow elastic capillaries, resulting in fibers that can integrate with textiles. The fibers were intertwined into a helix to fabricate capacitive sensors with the sensing capabilities of torsion, strain, and touch.[34]

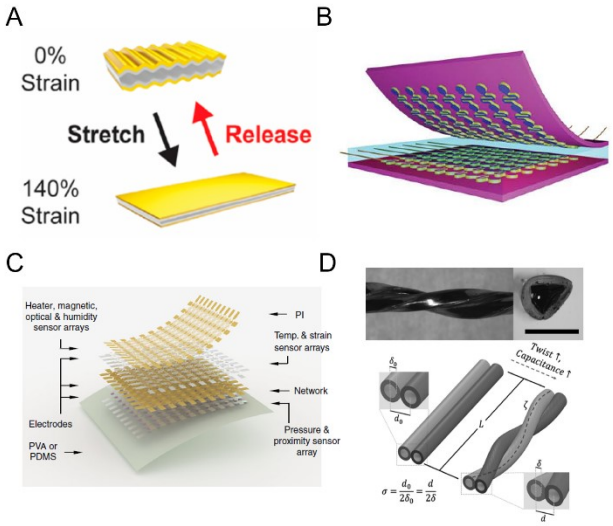

Figure 2.4 (A) Schematic of the assembly and structure of the Au film strain sensor.[31] (B) Schematic illustration of wearable multifunctional sensor array composed of PET-based Ag serpentine-shaped electrodes.[32] (C) Schematic layout of an SCMN-an integrated sensor array with eight functions.[33] (D) Schematic of the twisted fibers and torsion sensing mechanism.[34]

2.2.2 Triboelectric nanogenerator

Triboelectric nanogenerator have been extensively studied in recent years, as reported by Wang and colleagues in 2012. The basic working mechanisms of triboelectric nanogenerators are based on the coupling effect of contact electrification and electrostatic induction. When two different materials are brought into contact by mechanical stimuli, triboelectric charges are generated on the surfaces of these materials due to contact electrification. The charge then moves from one material to the other to balance the electrochemical potential difference. These materials in contact separate from each other as the applied force decreases, and the triboelectric

charge induces a potential difference at the upper and lower electrodes. Then, the induced potential difference will drive electrons to flow into the external circuit to generate current to balance the potential drop.[35,36] Based on the above working mechanism, TENG can be divided into four types according to different working modes: vertical contact-separation mode, lateral sliding mode, single-electrode mode, and freestanding triboelectric-layer mode. The TENG with the capability to harvest mechanical stimuli including impact, linear sliding, rotation, vibration and convert them into electricity, could not only act as an energy harvester but also as a self-power sensor.

Compared with most sensors, such as capacitive and resistive types of sensors, which need power sources for operation, the TENG sensor can harvest energy from external mechanical stimuli by itself. Thus, the triboelectric nanogenerator is considered to be a promising field of wearable sensor due to its high power output at low frequency mechanical energy (< 5 Hz) low cost, high power density, and simple design.

There is increasing interest in improving the sensing performance of the TENG self-power sensor. The two main strategies are regulating the material composition, and the fabrication of micro/nano structures. Many materials with high output performance have been used in triboelectric pressure sensors, such as poly-ε-caprolactone, nylon, Kapton, PTFE, PDMS, polyvinyl chloride (PVC), cotton acrylic, FEP, PU, etc. These materials have an overall trend of friction polarity of positive triboelectric material series of PU > hair > nylon > pine wood > cotton >

nitrile rubber, negative triboelectric material series of acrylic < PI < silicones < PE < PVC < PTFE. Another effective way is to fabricate microstructure in the active layer. Because charges are generated through contact electrification, the surface structure is integral to improving sensor performance.

2.2.2.1 TENG pressure sensor

Based on the above working principle of the TENGs, the output open-circuit voltage and short-circuit current are largely affected by external mechanical stimuli. The most common application for a TENG-self powered sensor is monitoring pressure. The vertical contact separation mode is the most commonly used in demonstrate the pressure sensing capabilities. In this case, the sensitivity *S* of the TENG sensors is given by the equation (6):

$$S = \frac{d_{\mathrm{v(p)}}}{d_{\mathrm{p}}} = \frac{\sigma_0}{\varepsilon_0} * \frac{d_0}{Y}$$

Where the σ_0 is the triboelectric charge density, ε_0 is the permittivity, Y is the Young's modulus and the d_0 is the gap of the active layer. According to the above formula, the Young's modulus and the initial distance of the interstitial layer play an important role in improving the sensitivity of the sensor. The introduction of the microstructure of the dielectric layer can be considered as an increase of gap layer $d_{0,}$ which could improve the sensing performance.

As shown in Figure 2.5A, Zhou et al. developed a flexible hierarchical elastomer-tuned self-powered pressure sensor that achieves both high sensitivity and

wide pressure range (7.989 V kPa^{-1}, 0.1–60 kPa) simultaneously.[37] The hierarchical elastomer microstructure (HEM) was sandwiched by two ultrathin films as a supporting structure to generate a tunable gap. The deformation caused by different Young's moduli is another important factor in determining the performance of self-powered pressure sensors. According to Ko et al., skin-inspired layered polymers with gradient elastic modulus enhance compressibility and contact area differences due to the effective transfer of external stress from the hard to the soft layers, resulting in highly sensitive triboelectric sensors (Figure 2.5B).[38] The hierarchical structure of nanoporous and interlocking micro-ridge-structured polymers can improve the effective variation of gap distances between interlocking layers without the need for large amounts of additional spacers, which allows for ultra-thin and highly flexible designs for wearable devices. The shape of the microstructure will also affect the pressure sensing performance. As shown in Figure 2.5C, Zu et al., studied the effect of the structural parameter on the TENG sensor sensitivity, and the output followed the following relationship: flat structure < line structure < cube structure < yramid structure.[39] Then Li et al. developed bendable and slidable fish-scale-like microstructures that took the advantage of bending and sliding movements. The prepared TENGs delivered open-circuit voltages to 470 V and a short-circuit current density of 45 $\mu A/cm^2$. The improvement of triboelectrification effect resulted from the bending and sliding of the fish-scale-like microstructures, which extended the triboelectric interfaces from the tops to the sidewalls of the unique microstructures (Figure 2.5D).[40]

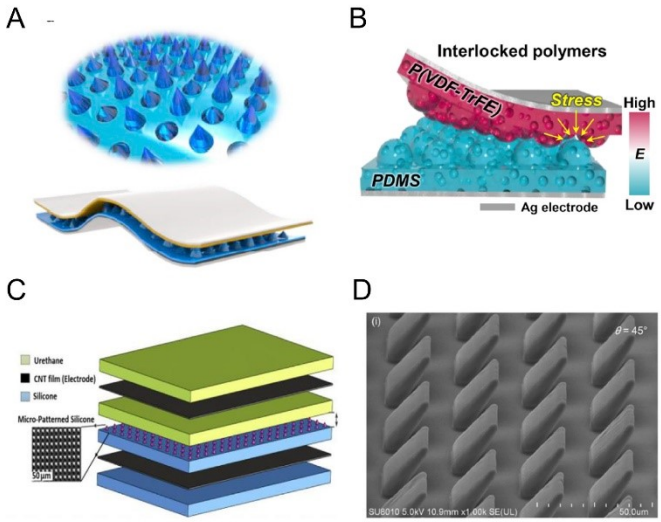

Figure 2.5 (A) Schematic structure of HSPS.[37] (B) Hierarchical and interlocked microridge structured P(VDF-TrFE) and PDMS-based TESs.[38] (C) Structural design of the stretchable TENG pressure sensor.[39] (D) SEM images of fish-scale-like microstructures with an acute angle of $\theta = 45°$.[40]

2.2.2.2 TENG for other types of self-power sensor

Beside measuring pressure, the TENG could also be developed for other types of self-power sensors such as strain sensor, proximity sensor, acoustic sensor, vibration sensor, etc. Wang et al. developed a stretch type of rubber-based triboelectric nanogenerator consisting of elastic rubber and aluminum film that acts as the electrode. The stretching of the rubber brings about a planar charge separation between the rubber and the aluminum, which induces an electric potential difference between the aluminum electrode and the ground. The potential difference between the aluminum electrode and the ground induces the charge transfer between the aluminum electrode and the ground. On the basis of its stretch sensing capability, the TENG can

be mounted onto a human body for detection of physiological activities and joint movements (Figure 2.6A).[41] The electrostatic induction effect of TENG can also allow the detection of noncontact motions. As shown in Figure 2.6B, Chen et al. reported a bionic-antennae-array sensor based on the single electrode-type TENG to detect noncontact motions. The antennae array was fabricated by conductive fibers on the triboelectric dielectric film, and the electrostatic balance between fibers and dielectric film can be employed to detect the noncontact motion.[42] Then the TENG can also be used to detect the minor vibrations caused by acoustic wave. An artificial basilar membrane based on TENG was developed by Choi et al., and the acoustic-to-electric transduction was implemented by triboelectrification between Kapton film and aluminum foil (Figure 2.6C). In addition, the artificial basilar membranes were to generate auditory evoked potential to realize cochlear tonotopy using an animal model.[43] Based on the lateral sliding mode of TENGs, the disk like TENG with segmental structures for harvesting rotational mechanical energy can be utilized as the rotation or angle sensor. As shown in Figure 2.6D, Wang et al., designed a quasi-static tribo-electric sensor based on a periodic contact/separation between foam with Cu material and a fluorinated ethylene propylene (FEP) film. The sensor can measure the absolute angular position, angular velocity, and acceleration regardless being continuously monitored or segmented monitored.[44] By the capability of detecting mechanical stimuli, the TENG could also design to different functional mechanical stimuli sensor in such as vibration sensor, displacement sensor, rotation sensor, acceleration sensor, etc.

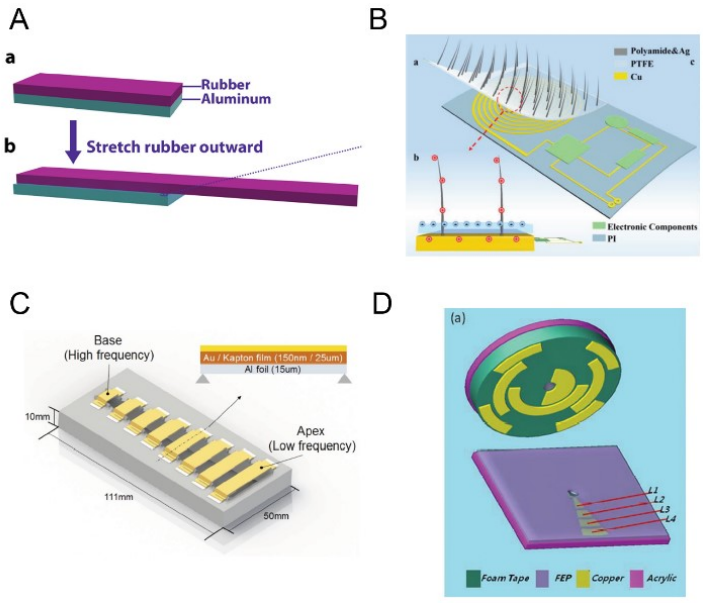

Figure 2.6 (A) Schematic diagram of the stretch rubber based TENG.[41] (B) Basic structure scheme of the bionic-antennae-array sensor.[42] (C) Schematic drawing of the triboelectric-based artificial basilar. membranes with eight beams. Each beam is fixed with Kapton film and aluminum foil.[43] (D) Schematic illustrations of the self-powered angel sensor, which has two parts, that is, a rotator and a stator.[44]

2.2.3 Piezoelectric sensor

The piezoelectric sensor operates based on the principle of piezoelectricity, which responds to external mechanical stimuli by generating instantaneous electrical signals. The piezoelectric effect includes two types: the direct piezoelectric effect and the inverse piezoelectric effect.[45–47] The inverse piezoelectric effect is that the piezoelectric materials can generate mechanical deformation resulting from an electric field. The direct piezoelectric effect is the process that when external mechanical stimuli applied to a crystal in a certain direction, electric polarization is generated

inside the crystal, positive and negative electric charges are generated at the two surfaces of the crystal, after the external force is removed, the crystal returns to an uncharged state. The direction of the electric charge coincides with the direction of the external force, and the amount of charge produced by the crystal is proportional to the magnitude of the external force. Most piezoelectric sensors are based on the direct piezoelectric effect. The piezoelectricity of a material depends on the non-centrosymmetric crystal. Taking quartz crystal as an example, the Si^{4+} and O^{2-} are symmetric with the overlapped positive and negative charge centers. The compression results in the shift of ions caused by the deformation of the crystal lattice, resulting in the malposed positive and negative charge centers. Then the surface A of the quartz crystal presents negative charges, while surface B presents positive charges. When stretch is applied along the x-direction, the malposed positive and negative charge centers make surface A present positive charges and surface B present negative charges.

Piezoelectric sensor does not require an external power source to drive the sensor layer to operate. Piezoelectric sensor is widely used to detect pressure and high-frequency vibration dynamically because of their high sensitivity, high signal-to-noise ratio and fast response ability. However, it is more suitable for dynamic sensing and is subject to temperature sensitivity and higher drift in response over time. Sensitivity and a higher responses drift over time.

The sensing performance of the piezoelectric sensor can be greatly improved by the material selection and microengineering of the active layer. Commonly used

piezoelectric materials such as lead zirconium titanate (PZT), $BaTiO_3$ (BTO), zinc oxide (ZnO), aluminum nitride (AIN), and fluorinated ethylene propylene (FEP) have been utilized owing to their high piezoelectric constant. However, inorganic piezoelectric materials cannot undergo large deformations. Thus, the flexible piezoelectric sensor can be fabricated by combining inorganic piezoelectric materials with flexible materials or using flexible organic piezoelectric materials such as PVDF, poly (vinylidene fluoridetrifluoroethylene) (PVDF-TrFE), etc. In addition, micropatterning of the piezoelectric active material can enhance the performance of piezoelectric pressure sensors due to a large degree of deformation.

2.2.3.1 Piezoelectric pressure sensor

The piezoelectric pressure sensor responds to external pressure by generating instantaneous electrical signals. Piezoelectric materials are attractive because they can generate electrical charges under mechanical stress and can therefore be used for force/pressure sensing applications. The commonly used piezoelectric materials, including lead zirconate titanate (PZT), lithium niobate, etc., exhibit strong piezoelectric properties, but they are toxic, nonrenewable, and nonbiodegradable components. From the perspective of material selection, the piezoelectric materials can typically be divided into inorganic piezoelectric material and organic piezoelectric materials, and the organic piezoelectric materials are more flexible than their inorganic counterparts, so they can deform under smaller applied forces.

Zhang et al. developed a flexible hybrid device that can be conformally attached to a soft surface like human skin to harvest diversity touch energies based on electrospun nanofiber mat. The structure integrated conductive nanomaterials coated nanofibers as electrodes, P(VDF-TrFE) nanofibers as a piezoelectric function layer, and PDMS as the friction layer. By combining single-electrode TENG and fiber-based PENG vertically together, the device can generate electricity not only during the contact-separation process but also during the continuous deformation process.[48] Cakmak et al. reported a method to prepare sensitive, flexible, and transparent piezoelectric materials where both lead zirconate titanate nanoparticles, and graphene nanoplatelets are aligned together in polydimethylsiloxane under an AC electric field. The strategy of alignment by electric field improves the piezoelectric response and transparency. The prepared piezoelectric film can sense the tiny pressure of a bird feather (1.4 mg), whereas at the touch of a fingertip, it can generate up to 8.2 V signal (Figure 2.7A).[49] As shown in Figure 2.7B, Rogers et al. introduced a large area, flexible piezoelectric material consisting of electrospun fibers of poly(vinylidenefluoride-co-trifluoroethylene) onto a fast-rotating collector. The prepared material provides outstanding piezoelectric characteristics, to enable ultra-high sensitivity for measuring a tiny pressure of 0.1 Pa.[50] Beside the proper material selection, the introduction of microstructure is also playing a key role in improving the piezoelectric sensing performance. As shown in Figure 2.7C, Cheng et al. introduced a gradient porous PZT ceramics with a cellular region, transition region, progressive lamellar region and homogeneous lamellar region that were prepared *via*

the freeze casting method. The porous gradient structure benefits the stress transfer and improves the efficiency of electromechanical conversion. The PENG exhibited outstanding performance with the output voltage of 152 V and current of 17.5 mA, which are much higher than those of piezoelectric composites with randomly dispersed PZT ceramic particles under the same external mechanical stress.[51]

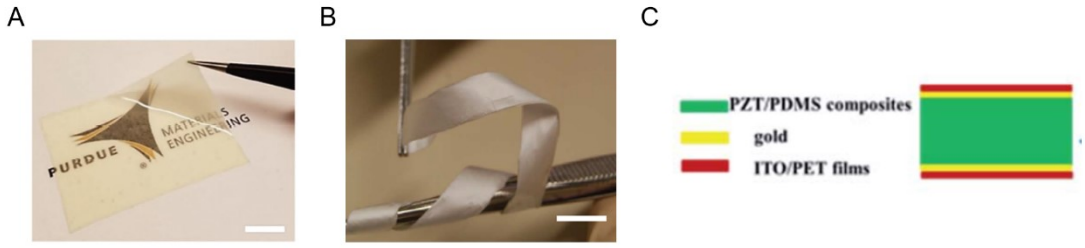

Figure 2.7 (A) Photograph of a free-standing 150 μm thick and electric field aligned (at 1000 V mm^{-1}) 0.5 vol% PZT/PDMS film (scale bar is 1 cm).[49] (B) Photograph of a free-standing film of highly aligned piezoelectric fibers. Scale bar: 1 cm.[50] (C) Schematic diagram of the PZT/PDMS composite-based PENG.[51]

2.2.3.2 Piezoelectric strain sensor

Piezoelectric polymers have been used in the development of stretchable sensors. Polyvinylidene (PVDF) is the piezoelectric polymer material with high piezoelectric performance, ductility, flexibility, and biocompatibility, but a relative low stretchability. Thus, structure design is to be applied to increase stretchability such as kirigami, honeycomb, helical structures, and metamaterials. According to Ahn, a stretchable piezoelectric strain sensor was developed by introducing a kirigami pattern to increase the stretchability of PVDF film. The piezoelectric kirigami sensor has a

sensitivity of 9.86 V/cm^2 and a stretchability of 320.8%, much higher than those of previously reported kirigami piezoelectric strain sensors (Figure 2.8A).[52] As shown in Figure 2.8B, Rossiter et al. also introduced a kirigami approach to fabricating stretchable strain sensor is through a network of cut patterns in a piezoelectric thin film. The power output was enhanced by the mechanoelectric piezoelectric sensing effect by introducing an intersegment, through-plane, electrode pattern. Then the kirigami stretchable piezoelectric sensor was applied in cardiac monitoring and wearable body tracking applications.[53] Besides the stretching measurement, the flexible self-powered piezoelectric sensor (PES) for the quantitative measurement of bending angle was reported by Yang et al. The PES was fabricated from cowpea structured PVDF/ZnO nanofibers through electrospinning technique. The bending sensitivity of the fabricated PES could achieve up to 4.4 mV deg^{-1} with response time of 76 ms, respectively. The PES could be conformably covered on different curve surfaces, demonstrated accurate detection of bending angle and fast recognition for realizing intelligent human-machine interaction (Figure 2.8C).[54] Benefiting from the high sensitivity properties, the piezoelectric sensor can also apply acoustic sensing. As shown in Figure 2.8D, Lee et al. introduced a self-powered flexible piezoelectric acoustic sensor (f-PAS) inspired by the basilar membrane in the human cochlea. The flexible PZT membrane on the plastic substrate was fabricated through inorganic-based laser lift off (ILLO) by mimicking the BM curved structure. The sensor achieved acquisition of the voice signal between 100 Hz and 4 kHz by a low quality factor (Q factor) and a multitoned band of the resonance frequencies.[55]

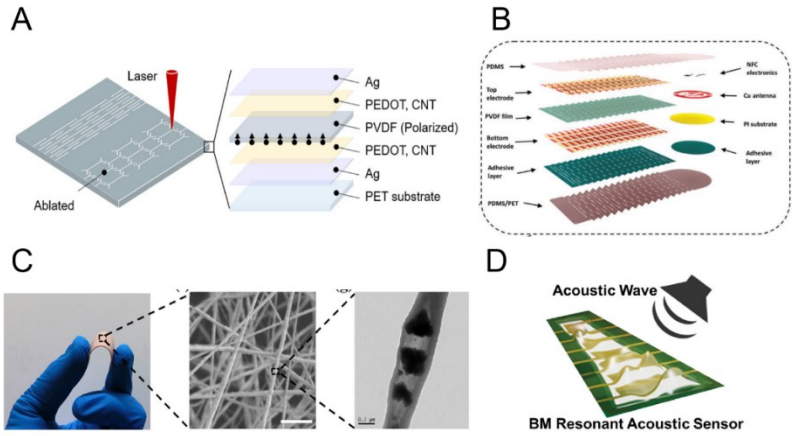

Figure 2.8 (A) Laser cutting process and layer structure of the sensor.[52] (B) Schematic illustration of the integrated device with multilayered structures between two subsystems: the stretchable sensor and wireless patch and enlarged electrode patterns.[53] (C) The photograph of the fabricated sensor under bending mode, and SEM and TEM images of the PVDF/ZnO nanofiber.[54] (D) Schematic illustration of the overall concept of the basilar membrane-inspired flexible piezoelectric acoustic sensor.[55]

2.2.4 Resistive sensor

Resistive type sensors transduce the applied mechanical stimuli into a change in the electrical resistance signal. A simple resistive sensor model is built as the whole resistance (R) of the device is the sum of R_e (the resistance of the electrodes) and R_a (the resistance of the active material), as given in the following equation (7):[23,56,57]

$$R = R_e + R_a$$

And the resistive change of active material can be described according to the

equation (8):

$$R_{\mathrm{a}} = \frac{\rho L}{A}$$

Where R is the resistance, ρ is the resistivity, L is the length, and A is the cross-sectional area. When the sensor is deformed under mechanical stimuli including pressure, stretching, bending or twisting, the contact area of the conductive material in the sensor changes, resulting in a change of conductive pathways and thus a change in resistance. From the formula, we can conclude that the variation of R comes from three main factors. First, the structure deformation of the active sensing layer causes the L and A parameters to change, leading to a variation of resistance value. Second, the resistivity of semiconductor filters and conductor filters owing to changes in the semiconductor band structure and interparticle separation. In these situations, a low compressive modulus of the active sensing layer is beneficial in improve the sensitivity because of the large deformation at a given pressure. Thus, the introduction of microstructure, including micropyrimid, microdome, porous structure, etc., can decrease the modulus to achieve a large deformation under a given pressure. The more a structure can deform to increase the contact area, the higher the sensitivity. Thirdly, the large contact resistance change can further increase the sensitivity, and the microstructure is one of the most commonly used techniques to improve the contact resistance of pressure sensor. The typical resistive pressure sensor with high contact resistance is constructed by two face-to-face microstructured elastomers. The advantage of this symmetrical face-to-face structure sensor is that it provides ultrahigh sensitivity in the low pressure range.

Compared with other types of flexible wearable sensors, the resistive type sensor has the advantages of their simple structure, simple readout principle, simple working mechanism, relatively simple fabrication process, low cost, excellent durability, fast response and recovery time, etc. And the sensing performance, such as sensitivity and sensing range can be further improved by proper material selection and micro/nano structure design.

From the perspective of material selection as the sensing material for resistive sensor, that can generally be divided into three main kinds, which are carbon-based materials, metal materials and conductive polymer materials. Carbon-based materials include carbon nanotubes, carbon nanofibers, graphene and graphene oxide, carbon black (CB), carbonized silk, carbonized wood, and carbonized crepe paper. Metal materials include metal nanowire (Au, Ag, Cu, etc.), metal nanoparticle (Au, Ag, Pd, etc.), metal nanoflake (Au, Ag, etc.), metal film (Pt, Ag, etc.), metal oxide, liquid metal, etc. Conductive polymer materials include polyaniline (PANI), polypyrene (PPy), (poly(3,4-ethylenedioxythiophene): poly(styrenesulfonate) (PEDOT:PSS), etc. Besides these three main kinds of sensing materials, there are still a lot of materials are used such as Mxene, metal-organic frameworks, etc. The internal microstructure of the sensing material and the electrode includes cracks, micro-rough structures, porous hierarchical structures, and multiscale hierarchical structures. These structures improve the sensing performance by increasing the space of contact change, decreasing the modulus and delaying contact saturation. Typically, the resistive type of sensor can be mainly divided into the piezoresistive pressure sensor, which is used

to measure pressure and touch, and the resistive strain sensor, which is used to measure the stretching process.

2.2.4.1 Piezoresistive pressure sensor

Typically, the basic principle of piezoresistive pressure sensor is to transduce the external pressure stimuli applied to the device into a recordable resistance value. The sensitivity (*S*), one of the most important parameters in evaluating the sensing performance, is a measure of the ability of sensors to convert external stimuli into electrical signals, which is defined according to the equation (9):

$$S = \frac{\Delta R/R_0}{\Delta P}$$

R is the resistance without applied pressure, the ΔR is the resistance variation between with and without the applied pressure, ΔP is the pressure variation. Besides the sensitivity, the sensing range, sensing linearity, selectivity, durability, detection limit, response and recovery time should also be taken into account. Here, we review the strategies to improve the sensing performance from the perspectives of material selection and structure design.

Material selection

Carbon based materials, such as CNTs, graphene, and carbon black, have been noted for their good electronic and mechanical properties. As shown in Figure 2.9A, Zhong et al. fabricate a high-performance and lightweight CNT/rGO-CNF carbon

aerogel. Benefiting from the synergistic effect of CNTs and cellulose nanofibers, the carbon aerogel presents superior elasticity (94.6% height retention for 50000 cycles), ultrahigh compressibility to 95% strain, high sensitivity, and an ultralow detection limit for pressure of 0.875 Pa.[58] As shown in Figure 2.9B, Shen et al. introduced a highly compressible waterborne polyurethane (WPU)/carbon nanotube (CNT) composite foam with excellent compressibility and stable piezoresistive sensing under 80% compression due to the porous structure and good elasticity of WPU. The fabricated sensor displayed a fast response time of 30 ms and good durability and reproductivity over 1000 compression cycles.[59]

Metal materials, including metal nanoparticles, nanowires, nano-thin films, and liquid metal, have been widely used in fabricated piezoresistive sensors. As shown in Figure 2.9C, Liu et al. fabricated a bio-based flexible piezoresistive sensor based on the "dynamic bridging effect" of silver nanowires (AgNWs) and reduced graphene oxide (rGO). The highly conductive AgNWs networks cross and bridge the neighboring high-resistive grain boundaries and rGO contacts when applied with pressure. The fabricated piezoresistive sensor showed high sensitivity (5.8 kPa^{-1}), fast response and relaxation properties of 29.5 ms and 15.6 ms, respectively, low detection limit (0.125 Pa), and outstanding durability of more than 10000 loading/unloading cycles.[60] As shown in Figure 2.9D, Park et al. introduced a 3D-printed rigid microbump-integrated liquid metal-based soft piezoresistive pressure sensor (3D-BLiPS). Galinstan, a eutectic metal alloy of gallium, indium, and tin, has the advantages of high electrical conductivity (3.4*106 Sm^{-1}), self-healing properties,

unlimited reversible strain range, and nontoxicity. The proposed pressure sensor had an extremely low detection limit (16 Pa) and a high sensitivity in the low pressure range (0.158 kPa^{-1} at the pressure of 50 kPa).[61]

The conductive polymer materials include polypyrrole (PPy), polyaniline (PANI), and PEDOT: PSS are the other conductive filler elements used in the fabrication of piezoresistive sensor. As shown in Figure 2.9E, Hsu et al. fabricated a piezoresistive pressure sensors with PEDOT: PSS/GO composite films. The miniaturized flexible piezoresistive pressure sensors with PEDOT: PSS/GO composite films were used to monitor the brain pressure of intracranial surgery of a rat and recognize different styles of music in hearing aids.[62] According to Abad et al., acrylic composites filled with 0–3 wt% polyaniline/multiwalled carbon nanotubes (PANI/MWCNT) were fabricated by Digital Light Processing (DLP) with tailored morphology, mechanical, and electromechanical properties. The structure is printed by DLP of conductive acrylic composite resins filled with up to 3 wt% PANI/MWCNTs. The composites display excellent piezoresistive sensing performance, no hysteresis, and stability for over 400 compression cycles (Figure 2.9F).[63]

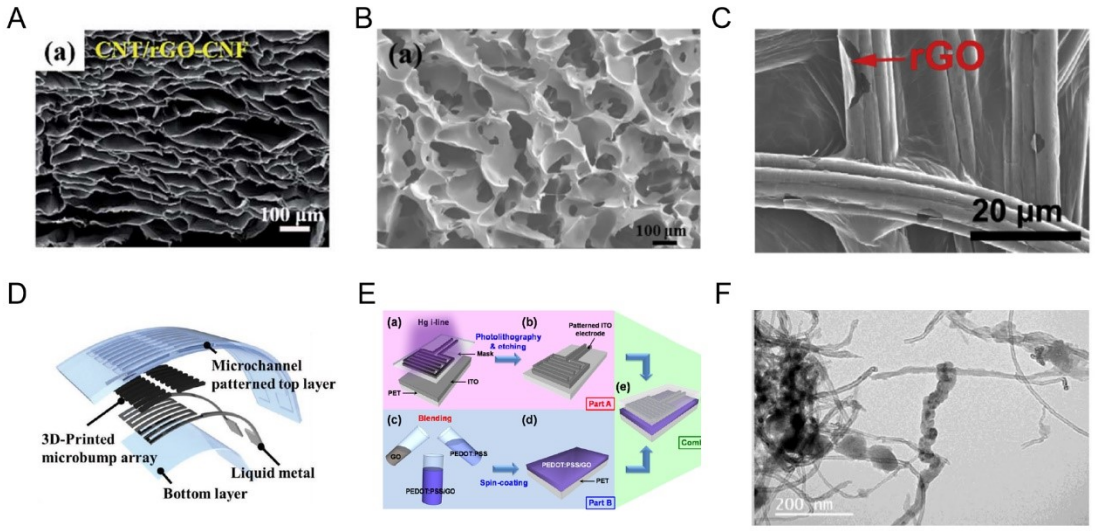

Figure 2.9 (A) SEM images of CNT/rGO–CNF aerogel.[58] (B) SEM images of waterborne polyurethane/carbon nanotube composite foam.[59] (C) conductive cotton fiber decorated with rGO.[60] (D) Schematic view of the proposed 3D-printed rigid microbump-integrated liquid metal-based pressure sensor.[61] (E) Fabrication procedures of piezoresistive pressure sensing devices with the interdigitated electrode structure.[62] (F) SEM image of polyaniline/multiwalled carbon nanotubes.[63]

Structure design and fabrication techniques

Micropatterned structure can bring air gap to the active layer or to the interface between active layer and electrode, which enable a high compressibility under a given applied pressure. The commonly used micropatterned structures include the microhemisphere, microdom, micropyramid, micropillar, nanowire, etc. As shown in Figure 2.10A, Duan et al. developed a highly sensitive and robust flexible pressure sensors based on conductive micropyramid polydimethylsiloxane/carbon nanotube composites. The microstructured conductive film was fabricated by drop-casting the PDMS/CNT solution in a prefabricated silicon mold. The prepared sensor presented

high sensitivity in both low and medium pressure regimes, high mechanical robustness, linear response, low hysteresis, fast response, low operating voltage, and low power consumption.[64] According to Cho, an internal popping of microspheres method was used to generate 3D and irregular microdome structures for flexible pressure sensors. The sensor exhibited high sensitivity (−50.45 kPa^{-1}) due to the heterogeneous contact change between the irregular microdome structure and a laser-induced graphene electrode. The sensor also had a short response time (τ(10–90%) ≈ 39 ms), excellent repeatability, and high reliability (Figure 2.10B).[65] To generate micropattern elastomers, the commonly used approaches can be classified as either using a mold to make the final structure or directly fabricating micropattern on the active layer. In the former method, a mold with a micropattern structure can be fabricated by photolithography, etching, etc. In addition, some biological materials, such as plant leaves, and commercial products, such as abrasive paper, can be used as mold. As shown in Figure 2.10C, Ha et al. used photolithography to fabricate micropores on silicon wafers and poured PDMS on the module to obtain the films with cylindrical microstructures. The proposed pressure sensor consists of the top layer of Au-deposited PDMS micropillars and the bottom layer of conductive polyaniline nanofibers on a polyethylene terephthalate substrate. The fabricated pressure sensor exhibited a sensitivity of 2.0 kPa^{-1} in the pressure range below 0.22 kPa, a low detection limit of 15 Pa, a fast response time of 50 ms, and excellent durability over 10000 cycles.[66] Compared with the complex process of replicated pattern from a model, some researchers directly pattern the elastomer surface. The

micropattern structure can be directly patterned by some technique such as directly laser micropatterning, prestretch-release treatments, etc. According to Wang et al., the piezoresistive pressure sensor based on a wavy-structured single-walled carbon nanotube/graphite flake/thermoplastic polyurethane (SWCNT/GF/TPU) composite film was fabricated by a prestretching process. The prepared sensor displays a low detection limit of 2 Pa, a wide sensing range of 0–60 kPa, and a high sensitivity of 5.49 kPa^{-1} for 0–50 Pa (Figure 2.10D).[67]

Porous structure has also been widely used to improve the sensitivity of resistive pressure sensors. The porous structure is more deformable than its equivalent bulk material. One simple way of fabricating porous active materials as piezoresistive sensors is to take an already porous material and coating with conductive material, such as melamine, polyurethane sponge, etc. According to Zhang et al., a highly sensitive and broad range pressure sensor was fabricated by sandwiching the interconnected nanocomposites of carbonized metalorganic framework (C-MOF) and polyaniline nanofiber (PANIF) on polyurethane (PU) sponge (C-MOF/PANIF@PU) between a breathable fabric and an interdigitated electrode-coated fabric. The interconnected nanocomposites of C-MOF/PANIF are obtained by coating the PU sponge with a mixture of C-MOF and PANIF solutions. The assembled sensor exhibited a broad sensing range to 60 kPa, high sensitivity of 158.26 kPa^{-1}, fast response and recovery time of 22 ms and 20 ms, breathability, and excellent durability over 15000 cycles (Figure 2.10E).[68] Another method to fabricate the porous structure is to either fabricate a 3D template structure and subsequently etch away the template

or to cure the active material around a material that can be subsequently etched away. As shown in Figure 2.10F, Zhang et al. proposed a highly sensitive piezoresistive pressure sensor based on hybrid porous microstructures. The porous structure in PDMS was fabricated by the sugar template method. The prepared pressure sensor presented a high sensitivity of 83.9kPa^{-1} (< 140 Pa) with a detection limit of 0.5 Pa and excellent stability.[69] The 3D printing technique was widely used to fabricate the porous structure due to the uniform porous structure design by the 3D printer. According to Zhu et al., the designable lattice structure pressure sensor was fabricated by digital light processing (DLP) 3D printing technique. The electrical sensitivities and mechanical properties of LPS can be accurately controlled by printed different lattice types and thicknesses (Figure 2.10G).[70]

There has been increased interest in the fabrication of hierarchical structures as the active layer. The common hierarchical structures include multilayered structure, hierarchical porous structure, hierarchical micropattern structure, etc. As shown in Figure 2.10H, Peng et al. fabricated a stretchable piezoresistive sensor (SPS) by combining a hierarchically porous sensing element with a multimodulus device architecture *via* 3D printing. The hierarchically porous structure was fabricated by 3D printing premixed inks of NaCl particles and polymer ink, followed by washing away the NaCl particles. The sensor exhibited high sensitivity of 5.54 kPa^{-1} over the sensing range from 10 Pa to 800 kPa, limited cross-correlation, and excellent durability.[71] As shown in Figure 2.10I, Zeng et al. prepared multilayer-structure piezoresistive pressure sensors with an in situ generated thiolated graphene@polyester

(GSH@PET) fabric. Benefiting from the spacing among the rough fabric layers and the highly conductive GSH, the prepared sensor exhibited a high sensitivity of 8.36 and 0.028 kPa^{-1} in the ranges of 0−8 and 30−200 kPa.[72]

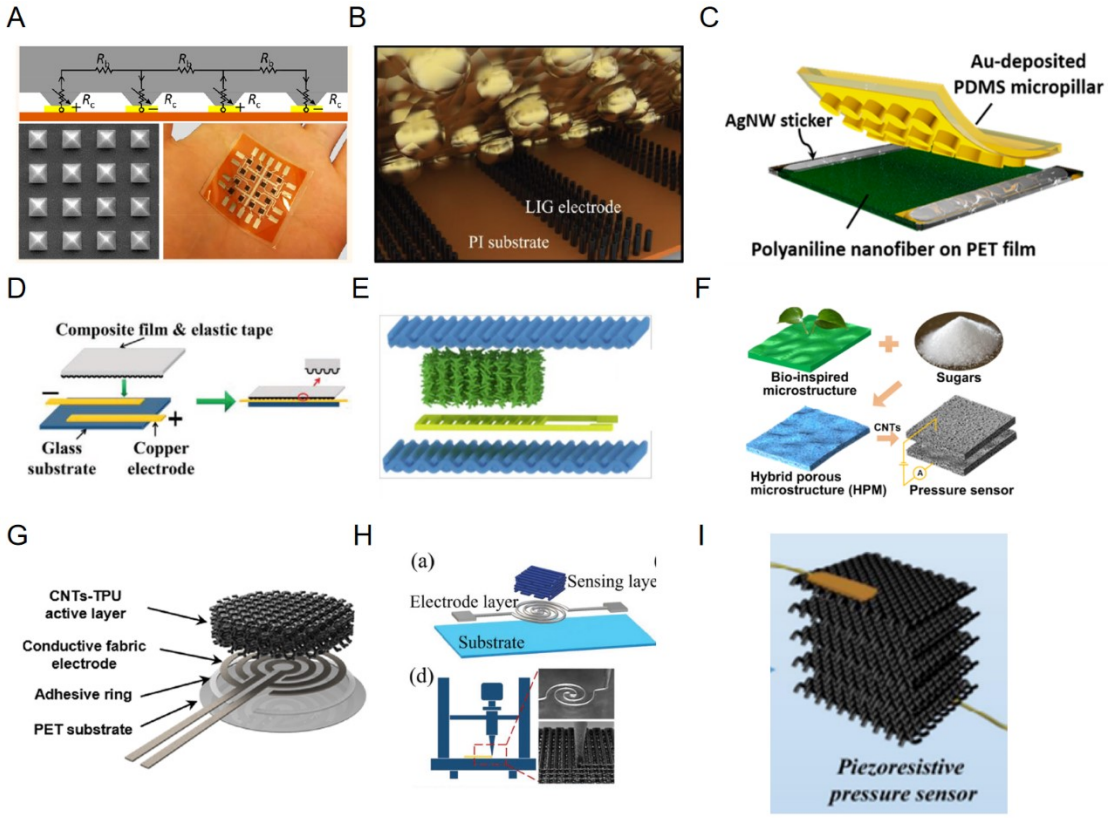

Figure 2.10 (A) SEM image and photograph of conductive micropyramidal film made of a PDMS/CNT composite.[64] (B) Schematic illustration of the pressure sensor with metal-deposited composite film with irregular microdome structure on the top active layer and interdigitated LIG on the bottom sensing electrode.[65] (C) Schematic illustration of the biaxially stretchable pressure-sensor array on a deformable substrate.[66] (D) Schematic illustrations of wavy-structured SWCNT/GF/TPU film.[67] (E) The assembly of the C-MOF/PANIF@PU based flexible wearable pressure sensors.[68] (F) Fabrication process of the pressure sensor based on HPM-PDMS.[69] (G) Schematic diagram of the assembled LPS.[70] (H) The design of SPS.[71] (I) Schematic

illustration of GSH@PET fabric-based piezoresistive pressure sensor.[72]

2.2.4.2 Resistive strain sensor

Resistive strain sensor converts the stretching deformation into resistance signal. The main parameters for flexible tensile strain sensors are stretchability and sensitivity, which are determined by the material selection and structures of conductive networks. The sensitivity of the resistive strain sensor is evaluated by the change of relative resistance under the applied strain, which is defined as the following equation (10):

$$\mathrm{GF} = \frac{\Delta R/R_0}{\varepsilon}$$

Where ε is the strain, ΔR is the resistance change during the stretching strain, and R_0 refers to the initial resistance value. Other parameters, including stretchability, reliability under repeated cycling, linearity, hysteresis, response and recovery time, etc., should also be taken into account to evaluate the strain sensor. In this part, the fabrication of high sensing performance strain sensor is reviewed from the perspectives of material design and structure design.[73]

Material selection

One of the most commonly used materials in strain sensor is elastomer-based stretchable electronics. And the most effective fabrication method is directly embedding conductive materials inside an elastomeric matrix by shear mixing,

ultrasonication, homogenization, and in situ synthesis. Elastomers serve as the strain carrier, while the conductive fillers offer electrical function. As shown in Figure 2.11A, Kim et al. reported an Ag-Au nanocomposites composed of ultralong gold-coated silver nanowires in an elastomeric block-copolymer matrix. The nanocomposites exhibited an optimized conductivity of 41850 S cm^{-1} due to the high aspect ratio and percolation network of the Ag-Au nanowires and exhibited an excellent stretchability of 266%.[74] However, the direct mixing strategy cannot fabricate homogenous conductive composites due to the low compatibility between the fillers and matrix. Then some researchers reported the design of a segregated electrically conductive network to solve the problem. As shown in Figure 2.11B, Liu reported an ice-templating strategy to fabricate graphene-based elastomer composites with a segregated nanostructured graphene network. The construction of a segregated GE network throughout the composites dramatically enhanced the electrical conductivity and reduced the electrical percolation threshold. The resulting composites, containing only 0.63 vol% graphene, present high liquid sensing responsivity and good reproducibility.[75] Depositing or transferring conducting materials onto an elastic polymer substrate is another commonly used method to fabricate thin electronic materials. As shown in Figure 2.11C, Wang et al. fabricated the strain sensor by directly coating super-aligned carbon nanotube (SACNT) films on PDMS substrates. The strain sensors presented a high sensing range of 400%, a fast response of less than 98 ms, and a low creep of 4% at 400% strain.[76]

Hydrogels with excellent flexibility and stretchability are favorable candidates for

wearable electronic devices. However, hydrogels are usually soft, weak, and brittle, which largely limits their applications. Some tough hydrogels with dual networks or multiple coordination bonds have been developed. As shown in Figure 2.11D, Zhao et al. constructed a dually synergetic network hydrogel by a versatile and topological co-cross-linking approach. The poly(N-isopropylacrylamide) PNIPAAm network is cross-linked by double-bond end-capped Pluronic F127 (F127DA), and PANI network is doped and cross-linked by phytic acid. The strain sensors exhibited a gauge factor of 3.92 when the applied strain is 0−120%, and a fast response time of 0.4 s.[77]

Intrinsically stretchable conducting polymer is another good candidate for strain sensor because of the flexibility in tuning the molecular structures and electrical and mechanical properties. As shown in Figure 2.11E, Bao et al. fabricated highly stretchable and conductive PEDOT films with high cycling stability by incorporating ionic additives–assisted stretchability and electrical conductivity (STEC) enhancers. The resulting PEDOT:PSS films exhibited both high conductivity of 4100 S/cm and stretchability of 100% strain.[78]

Textile based electronics attract tremendous interest since they provide higher durability and wear comfort. There are many methods to prepare conductive textiles, such as integrating metal filaments with yarns, coating fibers with a thin layer of conductive materials (metal nanoparticles/nanowires, carbon nanotubes, graphene,etc.), direct patterning of conducting polymers, and inkjet/stencil/screen/nozzle printing of conductive materials onto textiles. As shown in

Figure 2.11F, Wang et al. fabricated flexible strain sensing fabrics (FSSFs) by coating graphene oxide (GO) nanosheets on elastic nylon/polyurethane (nylon/PU) fabric, followed by reduction of GO with sodium borohydride. The fabricated strain sensor exhibited high sensitivity over a large workable strain range to 30%, fast response and great stability.[79]

Liquid metals are metals/alloys remain liquid state at room temperature. Liquid metals, such as gallium and its alloys, have attracted much attention as they exhibit an excellent combination of high conductivity and deformability. As shown in Figure 2.11G, Li et al. prepared a microfluidic strain sensor by introducing liquid metal eutectic gallium indium (EGaIn) embedded into a wave-shaped microchannel elastomeric matrix. The prepared strain sensor exhibited high GF of 4.91, high resolution with the low detection limitation of 0.09% strain change, quick response time of 116 ms and long-term stability.[80]

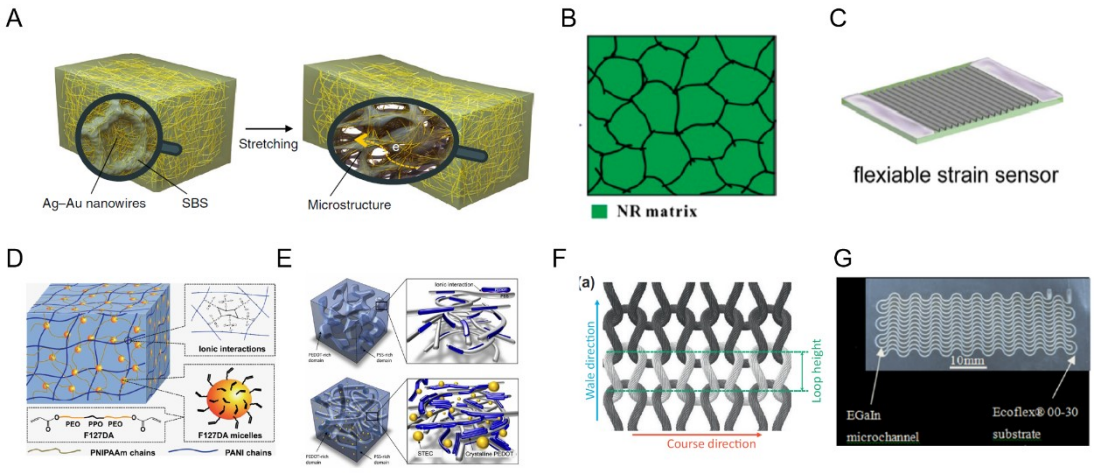

Figure 2.11 (A) Schematic illustration of the microstructured Ag–Au nanocomposite before and after stretching.[74] (B) Schematic illustration of cross-linked S-NRGE composites with segregated networks.[75] (C) Schematic illustration of SACNT strain sensor.[76] (D) Illustration of the network structure of F-PNIPAAm/PANI hydrogels.[77] (E) Schematic diagram representing the morphology of a typical PEDOT: PSS film versus that of a stretchable PEDOT film with STEC enhancers.[78] (F) Illustration of knitted structure of nylon/PU fabric.[79] (G) Images of the enhanced wave-shaped strain sensor.[80]

Structure design and fabrication techniques

To improve the sensing performance of strain sensor, some stretchable microscopical macroscopical structures such as fractal design and serpentine structure, coiled structure, out-of-plane wavy structure, open mesh structure, kirigami structure, and 3D porous structure have been developed. Some in-plane stretchable structures with fractal design include lines, loops, branch, serpentine, etc. As shown in Figure 2.12A, Su et al. reported stretchable strain sensors based on a contact-resistance free

structure, i.e., the off-axis serpentine sandwich structure (OASSS), with the mechanism of the stretch−bending−stretch transformation. The sensor exhibited large applied strain of 50%, with high repeatability (repeatability error = 1.58%) and linearity (goodness-of-fit >0.999).[81] However, the stretchability of inplane structures is limited due to structural failure caused by local stress concentration in the wires.

Some research demonstrates that the 3D coil structure has more uniform strain deformation than the 2D coil, which results in higher stretchability. As shown in Figure 2.12B, Zhao et al. fabricated a carbon nanotube (CNTs) and polyurethane (PU) nanofibers composite helical yarn with electrical conductivity, ultra stretchability, and high stretch sensitivity. The elastic PU molecules and springlike structure enable the helical yarn to have excellent stretchability, and CNTs are locked into the yarn through a simple twisting strategy, enabling good conductivity. The CNTs/PU helical yarn had good recoverability within 900% and maximum tensile elongation up to 1700%.[82]

Making thin films or highly conductive materials into out-of-plane buckles is one of the most direct methods to improve the stretchability. When applied a strain, the waves are straightened to accommodate the deformation. Gao et al. prepared a strain sensor based on a strain-sensing bilayer consisting of a wrinkled reduced graphene oxide layer and a highly susceptible Ag nanoparticles layer. The obtained strain sensor exhibited high stretchability and gauge factor (GF) both in subtle and large strain ranges (0–2%, GF: 420; 110–125%, GF: 1.1 × 109), low detection limit of 0.01%, and fast response time of 0.13 ms (Figure 2.12C).[83]

High stretchability could also be improved by introducing open mesh structures of various shapes. When mesh structures are stretched, the open holes deform with the strips rotating to accommodate the deformation. As shown in Figure 2.12D, Lu et al. constructed highly stretchable, conductive polymer composite open meshes by using a self-compensated two-order structure strategy. The conductive polymer composite was fabricated by 3D printing and coated with graphene layer. The resulting sensor revealed high GFs of 18.5 to 88 443 over a large work range from 0 to 350%.[84]

The stretchability can also be achieved by kirigami structure. The mechanical properties of a kirigami structure can be tuned based on unit cut geometry and hierarchical levers. As shown in Figure 2.12E, Takei et al. reported a kirigami structured graphene–polymer hybrid strain sensor using a laser direct writing technique on a polyimide sheet. By the design of kirigami structures, the fracture in the sensor material can be drastically reduced under high stretching conditions. The prepared strain sensor realized high stretchability of 200% strain and sensitivity (>80% resistance change at 60% strain).[85]

The 3D porous structure has also been proven to improve the stretchability. Similar to mesh structures, the pores deform with the accommodate the stretching deformation. According to Li et al., a highly stretchable and sensitive strain sensor was fabricated based on a porous segregated conductive network in the carbon nanotube/thermoplastic polyurethane composite by the salt-leaching method. The prepared strain sensor exhibited ultrawide sensing range of 800% strain, high sensitivity (GF of 356.4), fast response and recovery time of 180 ms, as well as

excellent durability (Figure 2.12F).[86]

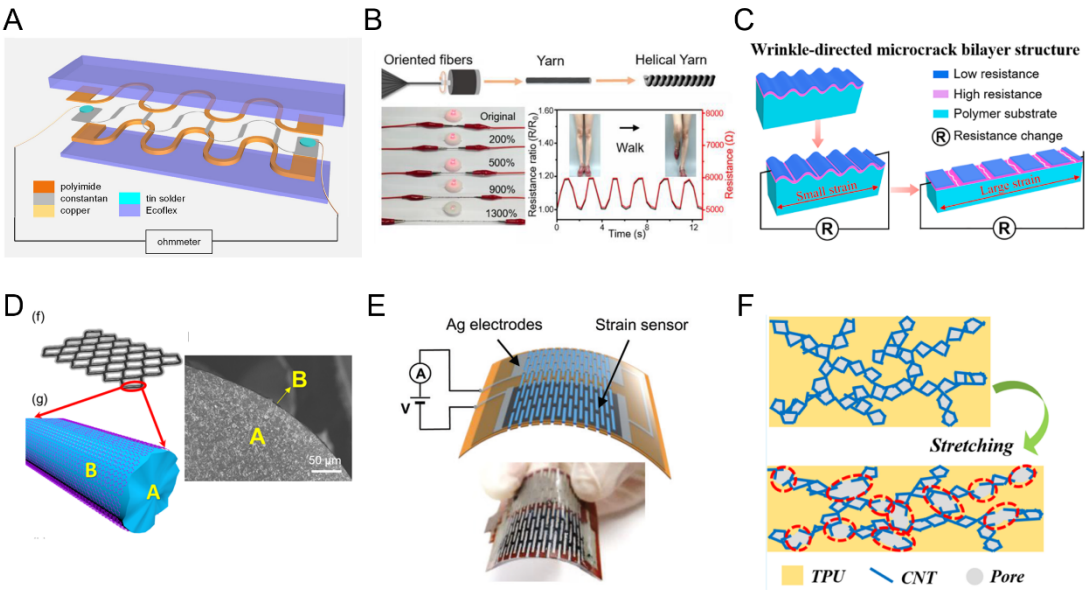

Figure 2.12 (A) Schematic illustrations and images of a contact-resistance-free stretchable strain sensor.[81] (B) Schematic illustrations of the helical CNTs/PU yarn.[82] (C) Schematic illustration of strain sensors based on wrinkle-directed microcracking bilayer configurations.[83] (D) The structure model and SEM image of the cross section of G−PDMS/RGO sensor.[84] (E) Schematic of an integrated device with printed electrodes.[85] (F) Schematic for the structure change in the CNT/TPU composite based strain sensors during stretching.[86]

2.3 Applications

Flexible wearable sensors with the high sensing performance of detecting multiple mechanical stimuli have attracted tremendous attention in the applications of health monitoring, motion detection, artificial skin, human-machine interface, etc. In

this chapter, we mainly review some research in the application of sports, health monitoring and human-machine interface.

2.3.1 Human motion monitoring

Wearable sensors have been widely used in the human body to detect human motion information such as bending of knees, hands, and fingers or monitoring of small-scale movements like subtle vibrations of the throat and chest while speaking and breathing.[87] Song et al. developed a flexible dual sensor with ultra-high sensitivity and a wide detection range for stretch and pressure. The prepared sensor has a high sensitivity of gauge factor (GF) up to 690.76 and pressure sensitivity of up to 169.94 kPa^{-1}, low detection limit of 1.274 Pa pressure and excellent durability. The sensor was able to detect weak and large movements of the human body, such as bending of the finger, wrist, knee, swallowing, speaking, jogging, running and jumping.[88] Cheng et al. developed a high-performance strain sensor by using gold and silver nanowires. The high sensitivity of the sensor was used to monitor emotional expressions by attaching the sensor to the face.[89] Liao et al. fabricated a self-assembly of MWCNTs in polymer composites to obtain a novel flexible strain sensor. The sensor exhibited a broad strain range up to 720%, with high sensitivity (GF = 1768), fast response and recovery time of 92.2 ms and 143.6 ms, and high durability (1050 cycles at 10% strain). The high sensing performance of the sensor can be used to monitor human physiological activities, and a gesture recognition system by detecting the extension

or bending of fingers and wrists.[90]

2.3.2 Health monitoring

The wearable devices integrated with sensors have been widely used in health monitoring. They are able to monitor various physiological signals in the human body, including breathing rate, pulse beat, body blood pressure, blood flow, tremor, etc. Khine et al. developed a capacitive pressure sensor with the wrinkled gold thin films on elastomeric substrates as the parallel plate electrodes, and microridged structures support the counter electrodes to create air cavities within the elastomeric dielectric layer. The prepared sensor was able to take continuous measurements of beat-to-beat blood pressure by translated from the measurement of the radial arterial pulse.[91] Wang et al. fabricated a helical fiber triboelectric nanogenerator by introducing helical structure braided fibers on a stretchable substrate fiber. The high sensitivity of the prepared sensor was able to detect the contraction and relaxation of the thoracic cavity and abdomen caused by the heartbeat and breathing. Then a wearable respiratory monitoring system was developed to diagnose potential respiratory diseases.[92] Wang et al. developed a facile plantar pressure mapping system by using piezoelectric nanogenerators as the sensor array to acquire pressure signals. The pressure mapping system was able to accurately monitor and visualize the real-time pressure distribution during walking, which can be used for sport/exercise biomechanics information acquisition, injury prevention, and ulceration prediction in the feet.[93]

2.3.3 Human-machine interface

Wearable sensors have also been widely used in human-machine interface such as gait analysis, posture correction, sports training, sign language, rehabilitation training, etc. Lu et al. fabricated an imperceptible EOG sensor system based on noninvasive, ultrathin, breathable graphene electronic tattoos (GET). The prepared sensors connect to a wireless transmitter attached to the collar to wirelessly control a quadcopter in real time by eyeball movements.[94] Yang et al. proposed triboelectric vibration sensors (TVS) by mimicking the ampulla of a fish. The tribo-pair of TVS were nanowire arrays and hemispherical pore structures. The sensor achieved a high force sensitivity of 0.97 V/N under the 1N force and a broad frequency range (1–3 kHz). Benefiting from the excellent performance, the TVS-based intelligent virtual digital keyboard was developed, which can sense and locate the position of the keystroke for interactive input and importer authentication.[95] According to Wang, a wearable triboelectric nanogenerator was fabricated with biodegradable and conductive carboxymethyl chitosan-silk fibroin (CSF). A maximum voltage of 165 V and output power density of 72 mW cm^{-2} were produced. A CSF-TENG-based human-machine interface (HMI) is developed to track writing steps and access the accuracy of letters, which builds a straightforward communication media between human and machine.[96] Kim et al. reported 1D/2D heterodimensional hybrids *via* dopant induced hybridization of Ti_3C_2Tx MXene with nitrogen-doped graphene nanoribbon. And the piezoresistive pressure sensor with the 1D/2D heterodimensional hybrids as the active layer presented low hysteresis (degree of hysteresis: 1.33%) and a wide sensing range

to 100 kPa. By utilizing the 8 × 8 sensor array and machine learning algorithm, the various seating postures could be classified with high accuracy (> 95%), facilitating the potential for future healthcare monitoring systems.[97]

2.4 Multifunctional sensor for detecting multiple mechanical stimuli

There have been a series of significant reports on developing wearable sensors with high sensing abilities such as sensitivity, stretchability, robustness, sensing range, etc. However, most reported wearable sensor is optimized for only detecting uniaxial mechanical deformation (such as lateral stretch or pressure). This severely limits its use in practical applications where the detection and differentiation of a variety of complex mechanical stimuli are essential. Thus, it is very important to develop a multifunctional sensor with the sensing capability to detect multiple mechanical stimuli.[98] As shown in Figure 2.13A, Cui et al. fabricated a highly sensitive and stretchable electronic skin based on an elastic graphene oxide (GO)-doped polyurethane (PU) nanofiber membrane with an ultrathin conductive poly(3,4-ethylenedioxythiophene) (PEDOT) coating layer. The nanofiber-based electronic skin sensor demonstrates a high-pressure sensitivity of 20.6 kPa^{-1}, a broad sensing range to 20 kPa, excellent cycling stability and durability (over 10,000 cycles), and a high strain sensitivity over a wide range (up to approximately 550%).[99] As shown in Figure 2.13B, Yuan et al. fabricated a multifunctional strain sensor based on

a network-structured MXene/polyurethane mat (network-M/P mat) through a facile and scalable electrospinning technique. Ye et al. fabricated a conductive hydrogel designed by proportionally mixing silk fibroin, polyacrylamide, graphene oxide, and poly(3,4-ethylenedioxythiophene): poly (styrenesulfonate). Due to the stretchability and compressibility of hydrogel, it can be assembled into a dual mode strain-pressure sensor with a wide sensing range (strain, 2%−600%; pressure, 0.5−119.4 kPa) and good durability.[100] According to Ha, a dual mode sensor was fabricated using polydimethylsiloxane coated microporous polypyrrole/graphene foam composite. The prepared dual-mode sensor exhibited high sensitivity, fast response and recovery time, and good durability during 10000 cycles. Additionally, the resistive-type strain sensor fabricated using the same PDMS/PPy/GF could detect the strain up to 50% (Figure 2.13C).[101]

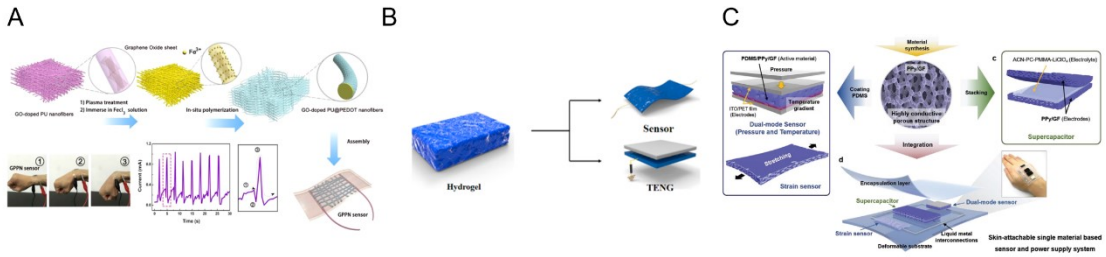

Figure 2.13 (A) Schematic illustration of the fabrication of the GPPN sensor.[99] (B) Schematic structures of the PSGP hydrogel, sensor, and TENG.[100] (C) Schematic illustration of dual-mode and strain sensors, and a flexible supercapacitor as a power supply, using a single highly conductive porous material.[101]

Although much progress has been made in developing multifunctional sensors with

the capability of sensing different mechanical stimuli, including pressure, stretch, bending, etc., most of them can't differentiate between multiple mechanical stimuli. The sensing features of these sensors exhibit the same electrical output tendency under different mechanical stimuli. Thus, it is needed to develop a multifunctional sensor that can not only detect the multiple mechanical deformations but also distinguish the types and directions of the stimuli. In order to develop multifunctional sensors with directional recognition ability, various strategies have been conducted, such as introducing new electrode materials, designing novel network structures, and developing new integration technologies. A direct strategy to develop multidimensional sensor is to integrate different types of sensors into a sensing system where each sensor is responsible for a single axial or a single stimuli sensing. As shown in Figure 2.14A, Sun et al. combined rational structure design and sensing materials to fabricate a stretchable and highly sensitive E-skin sensor. The prepared E-skin took a simple orthogonal configuration to enable pressure sensing by capacitive mode for pressure sensing and strain sensing by resistive mode independently.[102] The designing the sensing element with special microscopic architectures or spatially distributed components can also realize identification of multiple mechanical stimuli. Each sensing element can independently respond to a direction or a single form of stimulus sensing without interfering with each other. As shown in Figure 2.14B, Rogers et al. reported a three-dimensional type of microelectromechanical sensor that incorporates monocrystalline silicon nanomembranes in a configuration that enables independent, simultaneous

measurements of multiple mechanical stimuli, including pressure, shear force, bending, and temperature.[103] Some research also proves that microscale architectures such as nanopillars and micropyramid arrays can also be utilized to achieve multidimensional sensing. According to Jeong et al., high-performance stretchable electronic skin can be produced by incorporating carbon nanotube composite into a hierarchical of micropillar–wrinkle hybrid architectures. The hybrid e-skin structure was fabricated *via* a replica molding and subsequent wrinkle formation process. Benefiting from the hierarchical topography of the hybrid architectures, the prepared electronic skin exhibited versatile multiaxial force sensing, which includes pressure, bending, and tensile stresses (Figure 2.14C).[104] In addition, anisotropic structures can decouple the conductive network to achieve multidimensional sensing. As shown in Figure 2.14D, Kim et al. developed a stretchable multidirectional strain sensor with highly aligned, anisotropic carbon nanofiber (ACNF) films *via* electrospinning approach. By orthogonally stacking two single layer ACNFs to fabricate a cross-plied ACNF strain sensor, the sensor is capable of distinguishing the directions and magnitudes of strains with a remarkable selectivity of 3.84.[105]

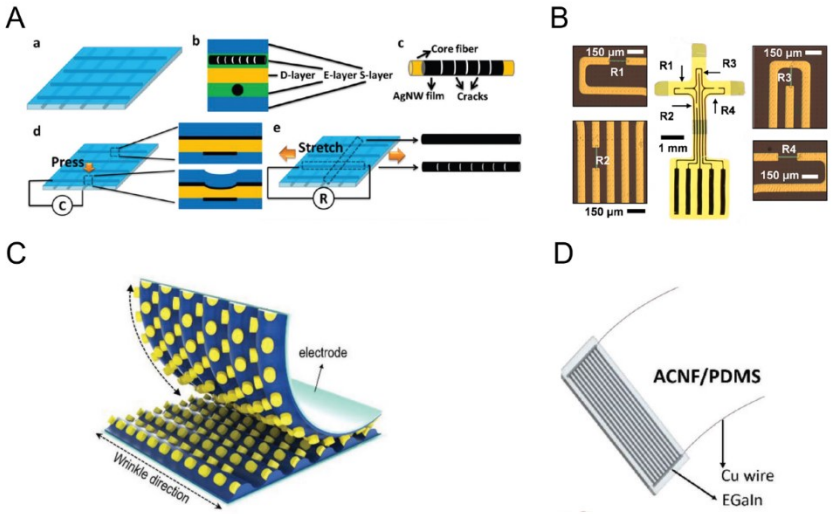

Figure 2.14 (A) Schematic illustrations of pre-cracked fiber electrode and the piezocapacitive E-skin device and pressure, stretch sensing mechanism.[102] (B) Optical microscope images of 2D precursor that have two piezoresistors (R_2 and R_3) in the vertical direction and the other two (R_1 and R_4) in the horizontal direction.[103] (C) Conceptual illustration of microscale wrinkle–pillar hybrid structures using piezoresistive CNT–elastomer composites.[104] (D) Schematic illustrations of ACNF strain sensors.[105]

2.5 Challenges for flexible sensors

For widespread deployment of flexible sensors in more application scenarios, the ideal pressure sensor requires high sensitivity and high linearity over a broad sensing range. However, one of the critical issues of the most developed flexible sensors is the poor sensing performance with a conflict between sensitivity, working range, and linearity. This is mainly caused by the rapid saturation of the change of microstructure contacts sites and generation of conductive pathways.

Another challenge of the most developed flexible sensors is the inability to detect and differentiate multiple mechanical stimuli. They present the same electrical output trend in response to different mechanical stimuli. When measuring one directional mechanical stimuli, the electric signal is interfered by stimuli from other directions, resulting in the inability to differentiate multiple mechanical stimuli. This severely limits their practical applications, which usually involve a variety of complex mechanical stimuli.

Thus, the goals of my projects are to solve these two main problems: 1. Develop a flexible sensor with high sensitivity over a broad linearity range and demonstrate it in the applications under different pressure scenarios. 2. Develop a flexible multifunctional sensor with the ability to detect and differentiate multiple mechanical stimuli, including pressure, stretch, convex and concave bending. Demonstrate it in the accurate detection of human kinesthesia, robotics, and human-machine interface.

Chapter 3. Fabrication of HPPS

3.1 Introduction

Flexible pressure sensors with the capacity of transducing tactile information into electric signals have attracted huge attention because of their promising applications in health monitoring,[106–110] artificial intelligence,[111,112] human-machine interfaces,[113–115] robotics,[116,117] etc. Typically, flexible pressure sensors are categorized into four types based on the sensing mechanism: piezoresistvie[5,6], capacitive[7,8], piezoelectric[9,10] and triboelectric[11,12]. Among these pressure sensors, piezoresistive sensors, which transfer mechanical information into resistance variation, have multiple advantages, including low energy consumption, ease of device assembly, simple signal acquisition, etc. However, most published piezoresistive pressure sensors suffer from low sensitivity or poor linearity over a broad range. For widespread deployment of pressure sensors in more application scenarios, the ideal pressure sensors require high sensitivity and high linearity over a broad sensing range.

Recently, several strategies to enhance the sensitivity and linearity have been reported. Preparation of nanostructure or microstructure geometries (such as wrinkles,[118] micropyramids,[119] microdomes,[120] micropillars,[121] interlock structure,[122] etc.[123,124]) on the flexible substrate can significantly enhance the sensitivity due to the low initial current and large deformability under low stress. For example, Tao et al. reported an interlocking microdome-structured based piezoresistive pressure sensor with a high sensitivity of 53 kPa^{-1} and the pressure range from 58.4 to 960 Pa.[125] Whereas the rapidly saturated microstructure contacts sites during compression, resulting in the high sensitivity and linear response only valid in a low sensing range

(<10 kPa). To extend the linear sensing range, the introduction of porous structure has been proven effective because of the high compressibility and considerable conductive pathways generation during compression. Seunghwan et al. developed a porous sponge sensor with the sensitivity of 0.01–0.02 kPa^{-1} under a broad sensing range from 10 Pa to 1.2 MPa.[126] Nevertheless, the pores increase the distance among the conductive fillers, which hinders the contact of conductive fillers and generation of conductive pathways. Thus, most of the porous pressure sensors exhibit a low sensitivity (< 1 kPa^{-1}) over a broad range. A few studies proposed a multi-layer or multiscale hierarchical structure with enhancements in both sensitivity and linear sensing range. For instance, Youngoh Lee et al. fabricated a tactile sensor with multilayer interlocked microdome geometry that presented high sensitivity of 47.7 kPa^{-1} over the range from 0.0013 kPa to 353 kPa.[127] However, the linear sensing range of the sensors is still not sufficient. Therefore, there is a strong need to fabricate a high performance (e.g., a linear response with high sensitivity over 1 kPa^{-1} over the range up to 1 MPa) pressure sensor in a simple and cost-effective way.

Herein, we propose a hierarchical in-situ filling porous structure as the sensing layer fabricated by DIW printing and curing of CNFs/PDMS emulsion. The hierarchical geometry is composed of lattice structure formed by DIW technique and the internal porous structure formed by the emulsion template method. This hierarchical geometry significantly increases the variation of contact area and distributes the applied stress to the multilayered lattice structure and internal porous structure. Benefiting from the customizability of the DIW technique, a face-centered

tetragonal (FCT) structure is designed with the highest compressibility compared with other types of lattice structures such as parallel stacked lattice structure and simple cubic lattice structure, enabling a broad sensing range. For in-situ filling porous structure fabricated by the soft emulsion template method, the CNFs dispersed in emulsified water remain inside the pores during the high temperature curing process, forming CNFs networks embedded in the pores. This in-situ filling porous structure led to the conductive fillers not only attaching at the edges of the pores but also in-situ filling in the pores, which significantly increase the sensitivity under pressure. Then we optimize the hierarchical in situ filling porous structure by thoroughly investigating the effect of the porosity, CNFs mass ratio, structure types, stacked sensing layer numbers,and printed lattice types.

3.2 Methodology

3.2.1 Materials

Carbon nanofibers (CNFs, model XFM60, purity > 95 wt%) with a diameter of 50–200 nm and a length of 1–15 μm were purchased from XFNANO company. The PDMS matrix (Sylgard 184) and curing agent were bought from Dow Corning Co., Ltd. Paraffin liquid was obtained from Sinopharm Chemical Reagent Co., Ltd. N-hexane (AR, 97%), 1,1,1,3,3,3-Hexafluoro-2-propanol (99.5%), and ethanol (ACS, purity > 99.5%) were purchased from Aladdin Co., Ltd. TPU pellets were purchased from Bayer Material Science.

3.2.2 Preparation of CNFs/PDMS emulsion as DIW printing ink

The PDMS matrix Sylgard 184 (5 g) and curing agent were fully mixed in a ratio of 10:1 in a 50 ml beaker. Then the prepared PDMS solution was diluted with paraffin liquid (5 g) by a high-shear dispersing machine (FS400-S, LICHEN Co., Ltd.) at a stirring speed of 1200 rpm. Then the aqueous solution with the calcium chloride concentration of 3.5 wt% was added dropwise by a microfluid syringe pump machine (SP-1000, Ningbo Annuo Medical Apparatus, and Instruments Technology Co., Ltd.) with a flow rate of 48 ml/h under mechanical stirring. After all the water was added into the PDMS/paraffin liquid mixture, a white and creamy PDMS emulsion was obtained. Then, the CNFs were added into the PDMS emulsion in batches under vigorous mechanical stirring by using a high-shear dispersing machine to form a black and creamy CNFs/PDMS emulsion. Upon the completion of the ink preparation, the CNFs/PDMS emulsion ink was ready for characterization and DIW printing.

3.2.3 Characterization of CNFs/PDMS emulsion ink

The morphology of the PDMS emulsion and CNFs/PDMS emulsion was characterized by upright microscope (ZEISS Axio Imager Vario) with objective lens (40×). The emulsion was dripped on the microscope slide and covered with a coverslip before observation. Rheological behaviors of inks were obtained using a rheometer (Physica MCR-301, Anton Paar GmbH Co., Ltd.) at ambient temperature

(25 ℃). The ink shear viscosity was measured by increasing the shear rate from 10^{-2} to 103 s^{-1}. Shear storage modulus (G') and viscous loss modulus (G'') were obtained in an oscillatory mode with a constant frequency of 1 Hz in the stress range from 10^{-2} to 103 Pa.

3.2.4 Fabrication of CNFs/PDMS emulsion lattice structure

The 3D CNFs/PDMS emulsion lattice structure was fabricated using pneumatic extruding DIW printing (SHOTmini200ΩX, Musashi Engineering, Inc.). All DIW printed lattice structure was fabricated based on the lattice structure models designed by 3D modeling software in DIW printer. The printed lattice structure was extruded and deposited on the PET substrates. Based on primary optimization, the nozzle diameter was 0.84 mm, the print head moving speed was 6 $mm \cdot s^{-1}$, and the extrusion pressure was controlled in the range of 50–100 kPa according to various compositions of CNFs/PDMS emulsion. After DIW printing, the CNFs/PDMS emulsion lattice structure was heated in an oven at 110 ℃ for 2 h to cure while evaporating the emulsified water. The cured CNFs/PDMS lattice structure was washed twice in n-hexane and ethanol, respectively, and subsequently dried at 110 ℃ for 2 h in an oven. The thickness of the CNFs/PDMS lattice structure with four layers is around 1.6 mm.

The porosity of the CNFs/PDMS emulsion lattice structure was controlled by the amount of water added, while the ratio of CNFs to PDMS is fixed. The porosity of

CNFs/PDMS sponge was calculated based on the following equation (11):

$$\text{porosity}=\frac{m_{(\text{CNF/PDMS block})}-m_{(\text{CNF/PDMS sponge})}}{m_{(\text{CNF/PDMS block})}}$$

3.2.5 Preparation of the HPPS

The fabrication of HPPS was as follows: First, the TPU film as the encapsulation layer was prepared by electrospinning of 4 wt% TPU dissolved in 1,1,1,3,3,3-Hexafluoro-2-propanol with a positive voltage of 10 kV and a negative voltage of 2 kV. The TPU film was cut into 2×2 cm^2 for protective layer. The pattern of the electrode was designed using CorelDRAW software. A laser cutting machine (4060, FST) was used to engrave the conductive fabric tape to the predesigned pattern. Then the two pieces of cut conductive fabric tape were transferred to the two pieces of cut TPU film as the top electrode and bottom electrode, respectively. The sensing layer of HPPS was encapsulated between two pieces of square TPU film with the conductive fabric tape.

3.2.6 Structural characterization

The morphology and microstructure of the samples were observed by field emission scanning electron microscopy with the voltage of 5 kV (Sirion200, FEI, USA).

3.3 Fabrication and structural characterization of HPPS.

The fabrication process of the hierarchical in-situ filling porous structure by DIW printing technique is illustrated in Figure 3.1. First, the PDMS emulsion was prepared by adding the aqueous solution with the calcium chloride concentration of 3.5 wt% dropwise into PDMS/paraffin liquid mixture through a syringe pump (Figure 3.1A). After vigorous mechanical stirring, the emulsified water droplets are uniformly distributed in the mixture to form creamy PDMS/water emulsion, which is shown in the optical microscope images in Figure 3.1A. Second, the CNFs were added into the PDMS emulsion in batches under vigorous mechanical stirring by using a high-shear dispersing machine. Benefiting from the batch's addition of CNFs, while under vigorous mechanical stirring of PDMS emulsion, the CNFs could homogeneously disperse in PDMS emulsion. Because of the mobilities and containable properties of the emulsified water, the added CNFs can disperse in the emulsified water, PDMS matrix and PDMS-water interfaces, as presented in Figure 3.1B. The photographs of the PDMS emulsion and CNFs/PDMS-emulsion are presented in Figure 3.2A and 3.2B.

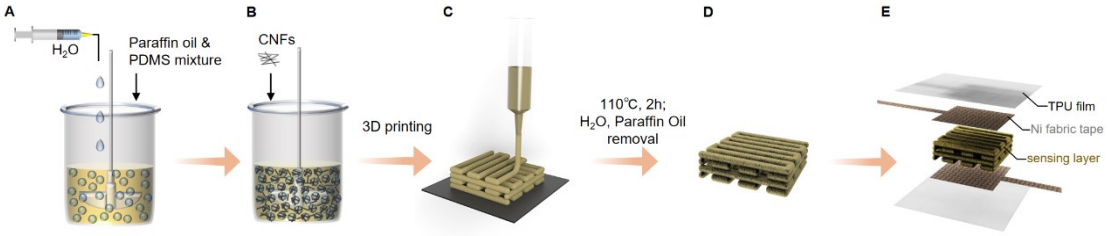

Figure 3.1 Schematic diagram of (A) PDMS emulsion, (B) CNFs/PDMS emulsion, (C) hierarchical in-situ filling porous structure by DIW printing, (D) hierarchical in-situ filling porous structure and (E) HPPS.

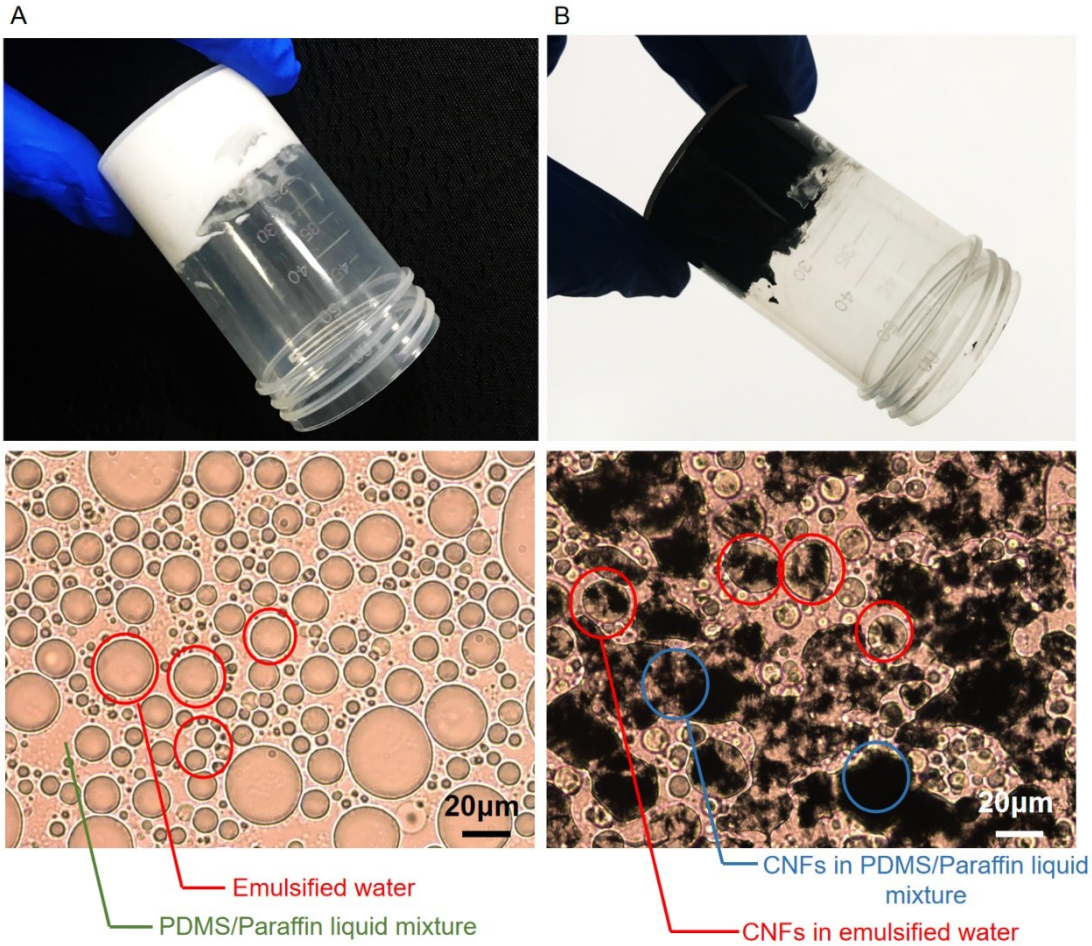

Figure 3.2 Optical and microscope images of emulsion and CNFs/PDMS emulsion with porous structure. (A) Optical image and microscope image of PDMS emulsion in an inverted vial. (B) Optical image and microscope image of CNFs/PDMS emulsion in an inverted vial.

Furthermore, the CNFs/PDMS emulsion with high shear thinning behavior and large storage modulus is beneficial in extruding and preserves self-standing 3D lattice structure, as interpreted in Figure 3.3A and 3.3B, respectively. The rheological measurements clearly suggest that the CNFs/PDMS emulsion inks are non-Newtonian fluids with shear-thinning behavior. Low viscosity at high shear (10^2 s^{-1}) rates suggests that inks can flow smoothly through the nozzle, and high viscosity at low shear (10^2 s^{-1}) rates indicates that inks could stack and preserve 3D shape integrity after leaving the nozzle. The viscosity is proportional to the CNFs concentration. When more CNFs are added, the CNFs/PDMS emulsion will become more viscous, which is beneficial to preserving 3D shape integrity after printing. As shown in Figure 3.3B, for the CNFs/PDMS emulsion inks, the storage modulus (G') is higher than the loss modulus (G'') at low shear stress, where the system resides in the linear viscoelastic region. This suggests that the inks are stiff with solid-like properties. When the shear stress increases to the yield point, the storage modulus is lower than the loss modulus, which indicates that the inks display liquid-like properties. The increased range of storage modulus at higher concentration of CNFs contributes to the retention of the 3D-printed shape. Thus, the CNFs/PDMS emulsion can be extruded uniformly and continuously from the nozzle and stacked layer-by-layer to construct a 3D lattice structure (schematic diagram in Figure 3.1C and optical image in Figure 3.3C).

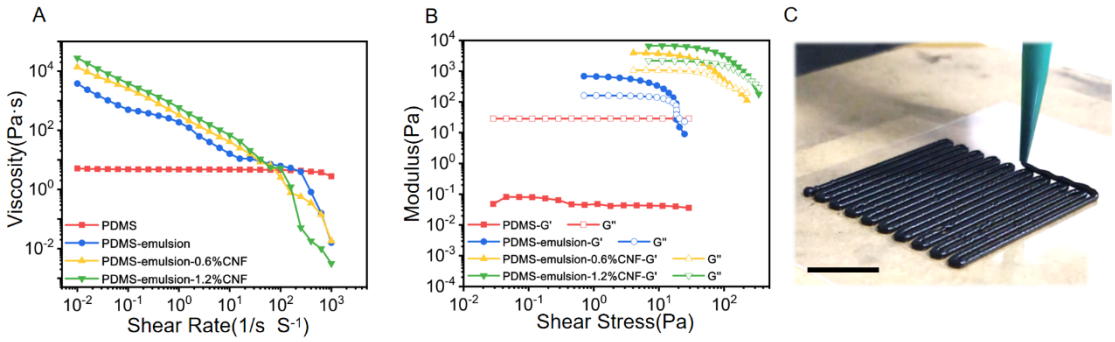

Figure 3.3 (A) The apparent viscosity as a function of shear rate (B) Storage modulus (G') and loss modulus (G'') as a function of shear stress. (C) Optical image of hierarchical in-situ filling porous structure by DIW printing.

Then, the printed CNFs/PDMS emulsion lattice structure is heated at 110 ℃ to make the PDMS fully cure, and emulsified water evaporate, which results in the formation of hierarchical in-situ filling porous structure with the CNFs networks embedded in the internal porous, as shown in Figure 3.1D. The cured CNFs/PDMS lattice structure needs to be washed twice in n-hexane and ethanol, respectively, and subsequently dried at 110 °C for 2 h to remove the paraffin oil to prevent the degradation of sensing performance. (Figure 3.4). As shown in Figure 3.4, the sensing layer without paraffin liquid removal will result in lower sensitivity, poor response time, and unstable signal performance where the current change keeps increasing at a fixed pressure. This is because the paraffin liquid hinders conductive material contact and reduces the elasticity of the sensing layer. Thus, the removal of paraffin liquid is a necessary step during the preparation of the sensing layer. After the paraffin is removed, the hierarchical in-situ filling porous layer is well prepared.

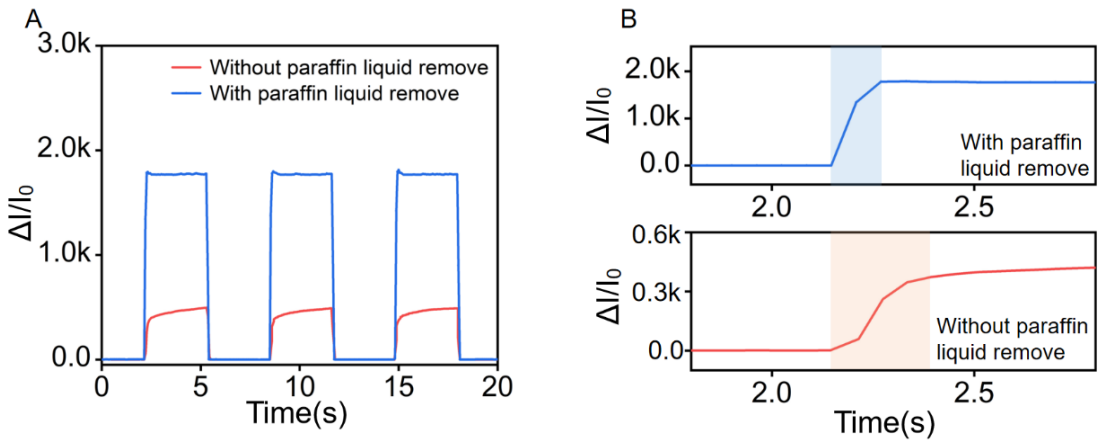

Figure 3.4 (A) Sensing performance and (B) response time comparison of sensors with and without liquid paraffin removal.

The morphology of the hierarchical in-situ filling porous layer is studied by scanning electronic microscopy (SEM), as shown in Figure 3.5. As the emulsified water embedded with the CNFs evaporates, the CNFs networks are left in the internal pores, which can be seen in the cross-sectional SEM images of the rod (Figure 3.5A and 3.5B). Figure 3.5A shows the cross-sectional view of the hierarchical in-situ filling porous sensing layer consisting of multilayers of lattice rods with a distance of approximately 500 μm between each rod. On the cross-sectional surface of a single lattice rod (Figure 3.5B), the internal porous structures with the diameter of 5–10 μm are evenly distributed in the lattice rod. The small gap of around 1 μm among the embedded CNFs networks is observed in a single pore structure (inset images of Figure 3.5B). It can be clearly seen from the cross-sectional SEM images that the CNFs are homogenously dispersed on the PDMS porous structure. In addition, a top view of the printed hierarchical in-situ filling porous structure is shown in Figure 3.5C.

The SEM image in Figure 3.5D, shows that some CNFs networks also exist in the PDMS matrix.

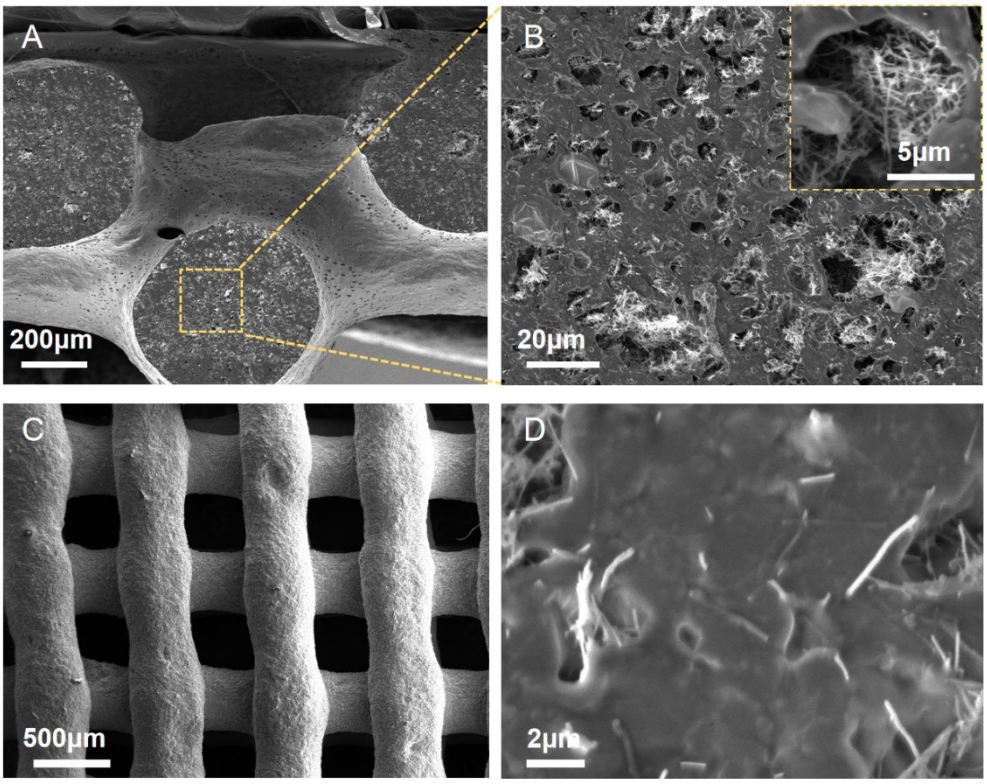

Figure 3.5 (A) Cross-sectional SEM image of the multilayered lattice structure. (B) Cross-sectional SEM image of inner porous structure in a single lattice rod. Inset high magnification SEM image of CNFs networks embedding in a single pore structure. (C) Top view of the printed hierarchical in situ filling porous structure. (D) CNFs networks embedding in PDMS matrix.

With the advantages of DIW technique, the custom fabricated lattice structures with different sizes (1×1 cm^2 and 2.5×2.5 cm^2) and different layer numbers are shown in Figure 3.6A and Figure 3.6B, respectively. This demonstrates that the DIW technique is capable of mass and customized production of the pressure sensor. Meanwhile, the

prepared porous layer shows good bending capacity, as shown in Figure 3.6C.

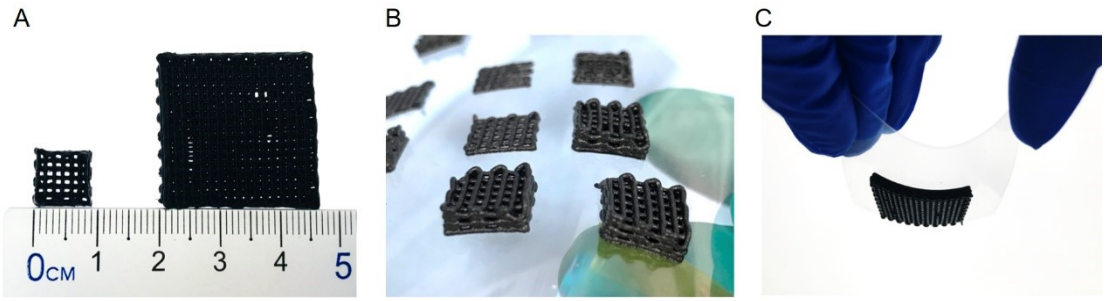

Figure 3.6 (A) Optical image of hierarchical in-situ filling porous structure with different sizes. (B) Optical image of hierarchical in situ filling porous structure with different lattice structures. (C) Optical image of hierarchical in situ filling porous sensing layer showing bending capacity.

The schematic diagram and the optical image of the whole assembled HPPS is shown in Figure 3.7A and 3.7B, in which the hierarchical in-situ filling porous structure serves as the sensing layer and the Ni fabric tape and thermoplastic polyurethane (TPU) electrospinning film (Figure 3.8) act as the electrodes and protective layers, respectively.

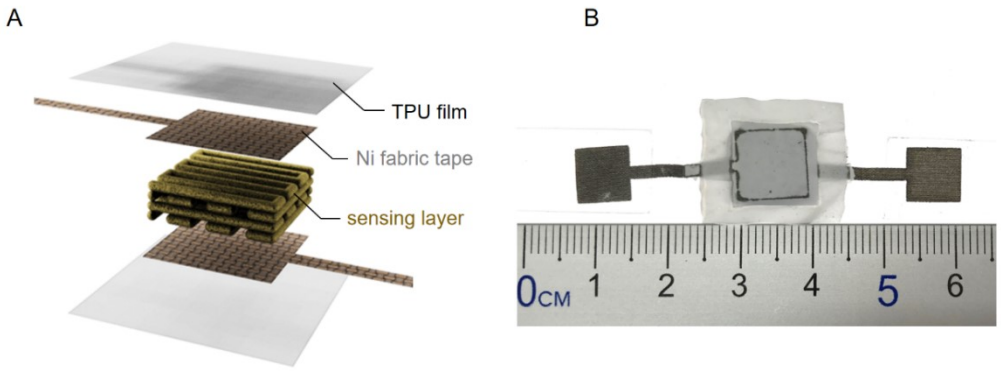

Figure 3.7 (A) Schematic structure and (B) Optical images of the HPPS.

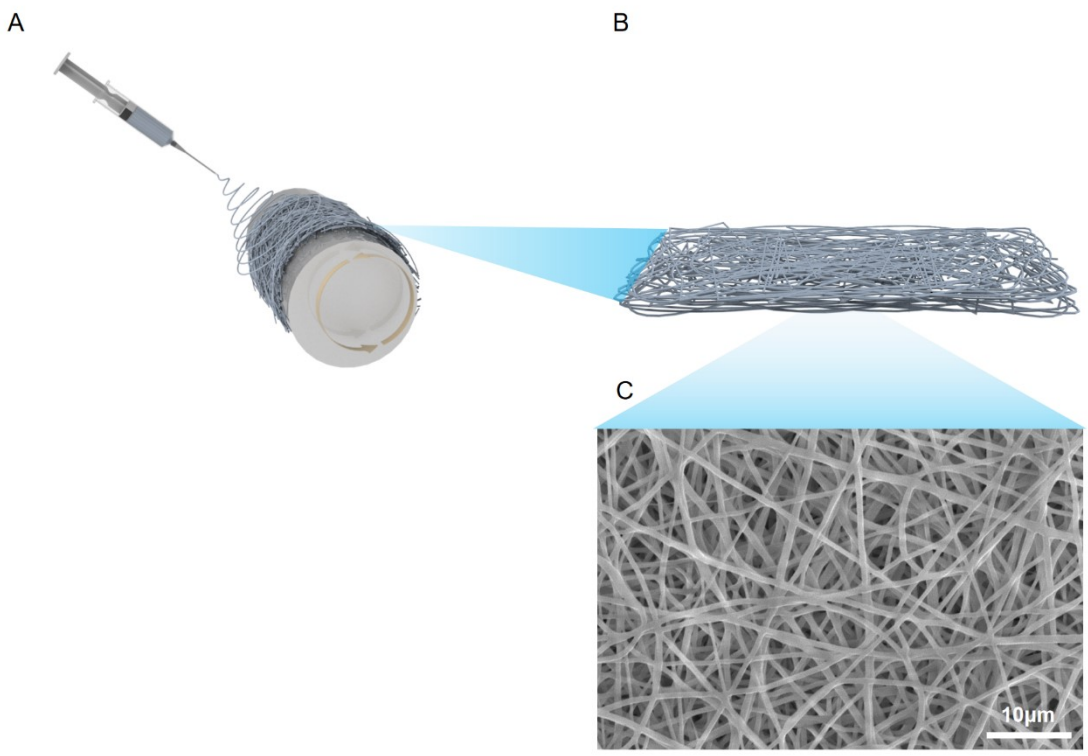

Figure 3.8 Schematic of the fabrication process of TPU film.

3.4 Parameter optimization of the sensing layer in HPPS.

To develop the optimal preparation parameters for the sensing layer, the influence of the porosity, CNFs mass ratio, structure types and stacked sensing layer numbers are thoroughly investigated, respectively. Here, when one of the variables is studied, the other ones remain unchanged. And the pressure sensitivity (S) is defined as $S = (\Delta I/I_0)/\Delta P$, where ΔI represents the current change of the sensor, I_0 represents the current without pressure and ΔP represents the applied pressure. The experiment setup for detecting the current change of the sensor is schematically shown in Figure 3.9. The force is provided and measured by a linear motor and a computer-controlled

linear motor, respectively. The current is recorded in real-time using a LabVIEW-controlled digital source meter (Keithley 2611B), and the source-drain voltage was 0.1V.

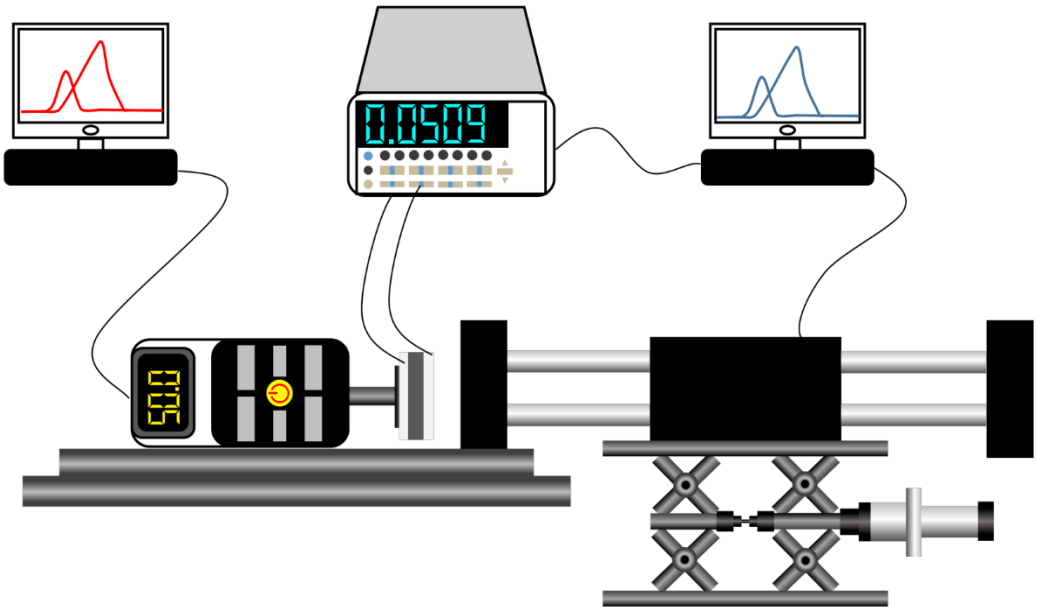

Figure 3.9 Schematic of the pressure sensing measurement setup.

First, four types of sensing layers (solid, porous, lattice and lattice with porous) with the same extended contour volume were prepared, as shown in Figure 3.10A. Figure 3.10B shows the detailed sensitivity of each type of sensing layer. The solid structure has the lowest sensitivity of 0.19 kPa^{-1}, while the porous structure and the lattice structure have higher sensitivity of 0.47 kPa^{-1} and 1.65 kPa^{-1}, respectively. As we all know, a higher compression generates more conductive pathways within the sensing layers. So, the porous structure formed by emulsion template method has higher compressibility under the same pressure. For lattice structure, the macroscale

gap between the lattice rods produced by DIW also provides higher compressibility.

Here, the synergetic effect of the internal porous and lattice structure endows the structure with the highest compressibility among them, which results in the highest sensitivity of 2.4 kPa^{-1} with high linearity (R^2 = 0.993). Then multiple samples of pressure sensing layer with different geometrical structures, including solid, porous, lattice, and lattice with porous, were repeatedly measured to further demonstrate the highest sensitivity of the lattice with porous pressure sensing layer, as shown in Figure 3.10C. In addition, the linearity of pressure sensing layers with different geometrical structures was measured in Table 3.1. The lattice with porous structure exhibits the best linearity compared with other kinds of structure. In addition, the lattice with porous structure has the highest linearity (R^2=0.993) compared with lattice form (R^2=0.991), porous (R^2=0.93), and solid form (R^2=0.91).

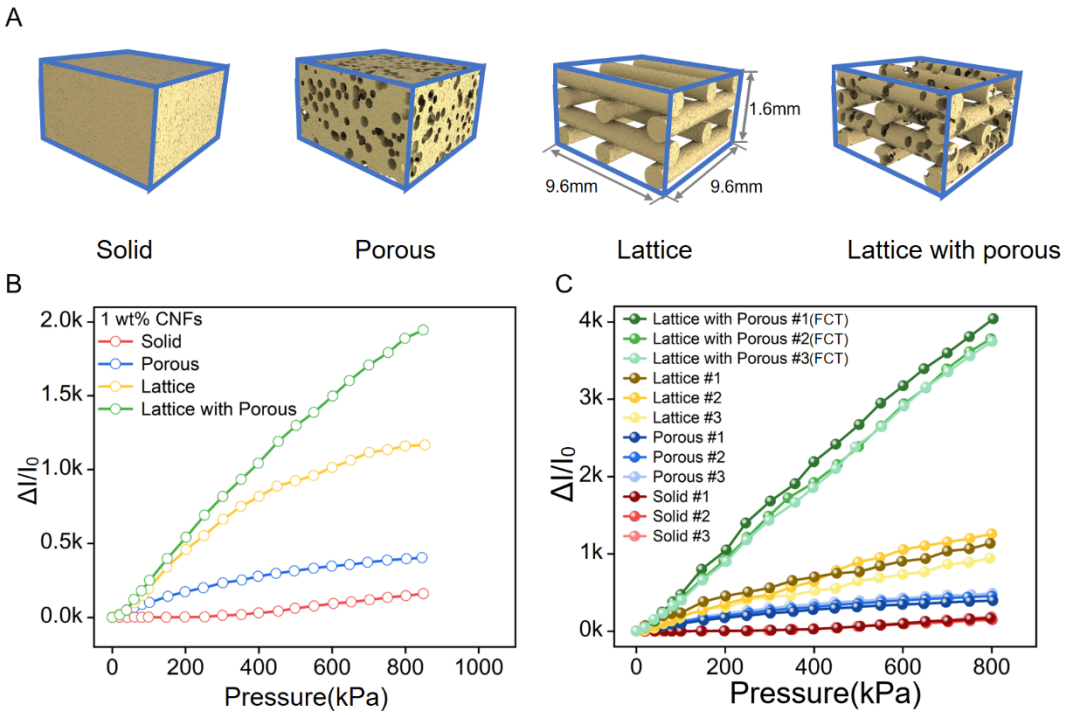

Figure 3.10 (A) Sample preparation with the same extended contour volume for studies of the effect of geometric structure. (B) Current response and sensitivity of 1 wt% CNFs, 60% porosity pressure sensors with different geometrical structures (solid, porous, lattice, lattice with porous). (C) The current response of pressure sensor with multiple samples of different geometrical structures.

Table 3.1 The linearity of pressure sensors with different geometrical structures.

	Lattice with porous(FCT)	**Lattice**	**Porous**	**Solid**
Sample 1	0.999	0.985	0.94	0.873
Sample 2	0.998	0.991	0.954	0.908
Sample 3	0.997	0.979	0.955	0.889

Note that for the effect of composition of water and CNFs and structure types, the layer numbers are fixed at four because the structures with four layers possess the best

sensing performance compared with the structures with other layers. The reason of four-layer structure has the best sensing performance is explained in detail in Figure 3.11 and Table 3.2. Based on the definition of sensitivity $S = (\Delta I/I_0)/\Delta P$, the sensitivity is determined by the current change ΔI and the initial current I_0. The I_0 of the four-layer structure is lower than that of the structure with more than four layers.

As shown in Figure 3.11A and Table S2, compared with the one-, two-, and three-layer structures, the four-layer structure has more empty space between the lattice rods, resulting in higher deformability and more conductive pathway generation. The $\Delta I/I_0$ of four-layer structure is larger than $\Delta I/I_0$ of a structure with fewer than four layers. When compared with five-layer structure, the initial current of the four-layer structure is around 1.1 μA which is much smaller than the initial current of five-layer structure, which is about 3 μA. When the pressure reaches 800 kPa, the final current of the four-layer structure and the structure with more than four layers are comparable. In that case, the I_0 is the dominant factor to determine the sensitivity, where the $\Delta I/I_0$ of four-layer structure is larger than $\Delta I/I_0$ of the structure with the layer number of more than four layers. In addition, multiple samples of HPPS with 3, 4 and 5 layers of sensing layer are fabricated and measured in Figure 3.11B.

The main reason for the larger I_0 of the structure with more than four layers is that the TPU packaging layer has a larger initial pressure on the sensing layer. As shown in schematic Figure 3.11C, the sensor layer was encapsulated with double-side adhesive tape by two pieces of TPU film adhered with Ni conductive fabric tape. Each layer of the printed structure is about 0.4 mm thick, so one more layer of printing will result in

a larger increase in thickness. The thicker the sensing layer, the larger initial pressure of the upper and lower TPU film applied on the sandwiched sensing layer. This leads to tighter contact between the electrodes and sensing layer, and even slight compression of the sensing layer, resulting in a larger initial current.

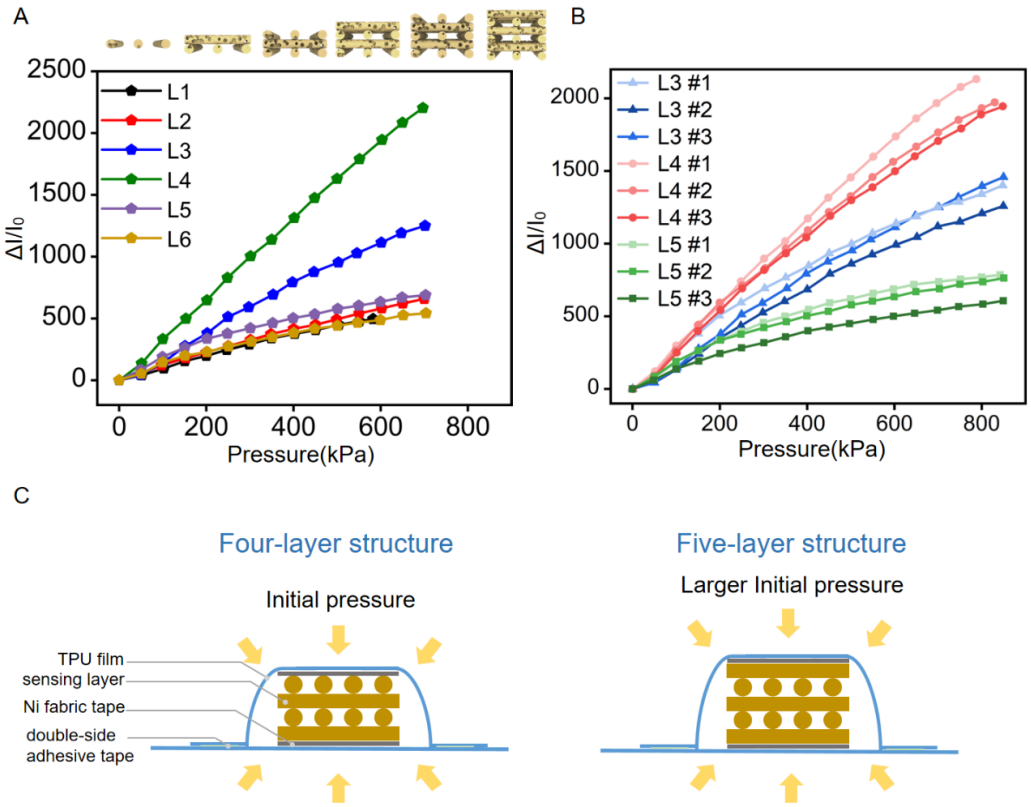

Figure 3.11 (A) Current response and sensitivity of HPPS with different numbers of sensing layers. (B) The comparison of the sensitivity of HPPS with 3, 4 and 5 layers by testing many samples. (C) Schematic cross-sectional view of the structure of the HPPS.

Table 3.2 The comparison of the I_0, ΔI, and $\Delta I/I_0$ of HPPS with 3, 4 and 5 layers by testing many samples.

Layer number	Sample	I_0 (μA)	ΔI (mA)	$\Delta I/I_0$
3 layer	1	0.984	1.38	1401
	2	0.923	1.34	1457
	3	0.977	1.23	1260
4 layer	1	1.12	2.38	2132
	2	1.01	1.99	1971
	3	1.10	2.14	1944
5 layer	1	2.88	2.26	785
	2	2.82	2.13	763
	3	3.62	2.19	606

Next, the effect of composition of water on sensing performance is well studied in Figure 3.12. Based on the previous studies and comparative experiments (Table 3.3) about the effect of amounts of emulsified water on porosity, the porosity could be simply adjusted by varying the mass ratio of water in the emulsion system.[128,129] The porosity increases with the increasing content of the emulsified water. The porosity is characterized through the mass difference method (see the Experimental Section for details). As shown in Figure 3.12, the higher porosity structure exhibits higher sensitivity. Compared with the sensors with porosity of 33% and 47%, the pressure sensor with 60% porosity exhibits improved sensitivity (3.2 kPa^{-1}) and linearity (R^2 = 0.998) in the range of 0–750 kPa. This is because the higher porosity structure with the lower young modulus is more compressible under the same pressure. Thus, a subtle pressure would largely deform the structure and create more conductive pathways in the high porosity structure.

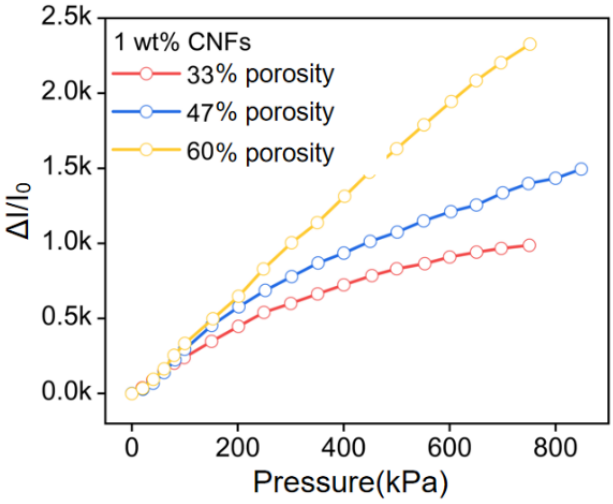

Figure 3.12 Current response and sensitivity of four layers SC pressure sensor with different mass ratios of water.

Table 3.3 The porosity of PDMS sponge under preparation conditions with different amounts of water.

Samples	PDMS:water	$m_{(PDMS\ sponge)}$ (g)	Porosity (%)
1	5:4	0.3169	34.86
2		0.3369	30.75
3		0.3269	32.80
4		0.3369	30.75
5		0.3169	34.86
6	5:7	0.2477	49.08
7		0.2558	47.42
8		0.2640	45.73
9		0.2730	43.88
10		0.2647	45.59
11	5:14	0.1968	59.54
12		0.2021	58.45
13		0.1987	59.15
14		0.1980	59.30
15		0.1933	60.26

Third, the content of CNFs also has an observable effect on the sensors. So, the sensors with the CNFs mass ratio ranging from 0.6 wt% to 1.2 wt% are prepared, and their influence on the sensitivity is studied in Figure 3.13. For the sensors prepared with the CNFs amount from 0.6 wt% to 1 wt%, the sensitivity gradually improved. The increased mass ratio of the conductive fillers can construct more conductive pathways when applied with the same pressure, which results in a higher sensitivity. However, excessive CNFs greatly reduce the resistance in the original state (I_0), which leads to a decrease in the relative current changes. As a result, the sensitivity of the sensor with 1.2 wt% CNFs is lower than the sensor with 1 wt% CNFs.

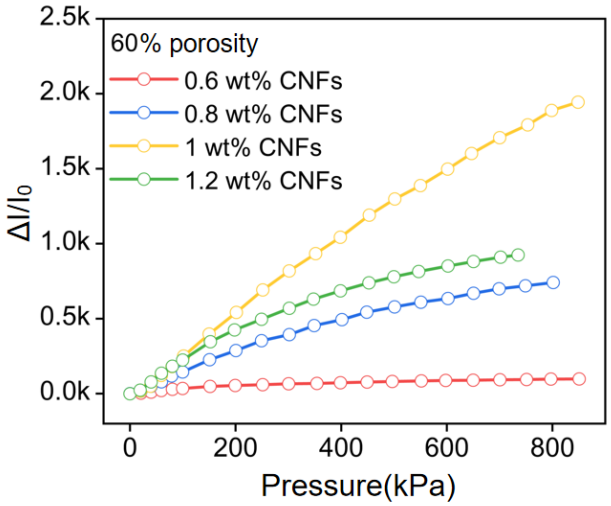

Figure 3.13 Current response and sensitivity of four layers SC pressure sensor with different mass ratios of CNFs.

Finally, three different lattice structures: simple cubic (SC), parallel stacked (PS), and face-centered tetragonal (FCT) are simply fabricated through DIW based on the designed structural model.[130] All the lattice structures are fabricated with the same amount of emulsion. The design diagrams of the SC, PS and FCT structures are

shown in Figure 3.14, respectively.

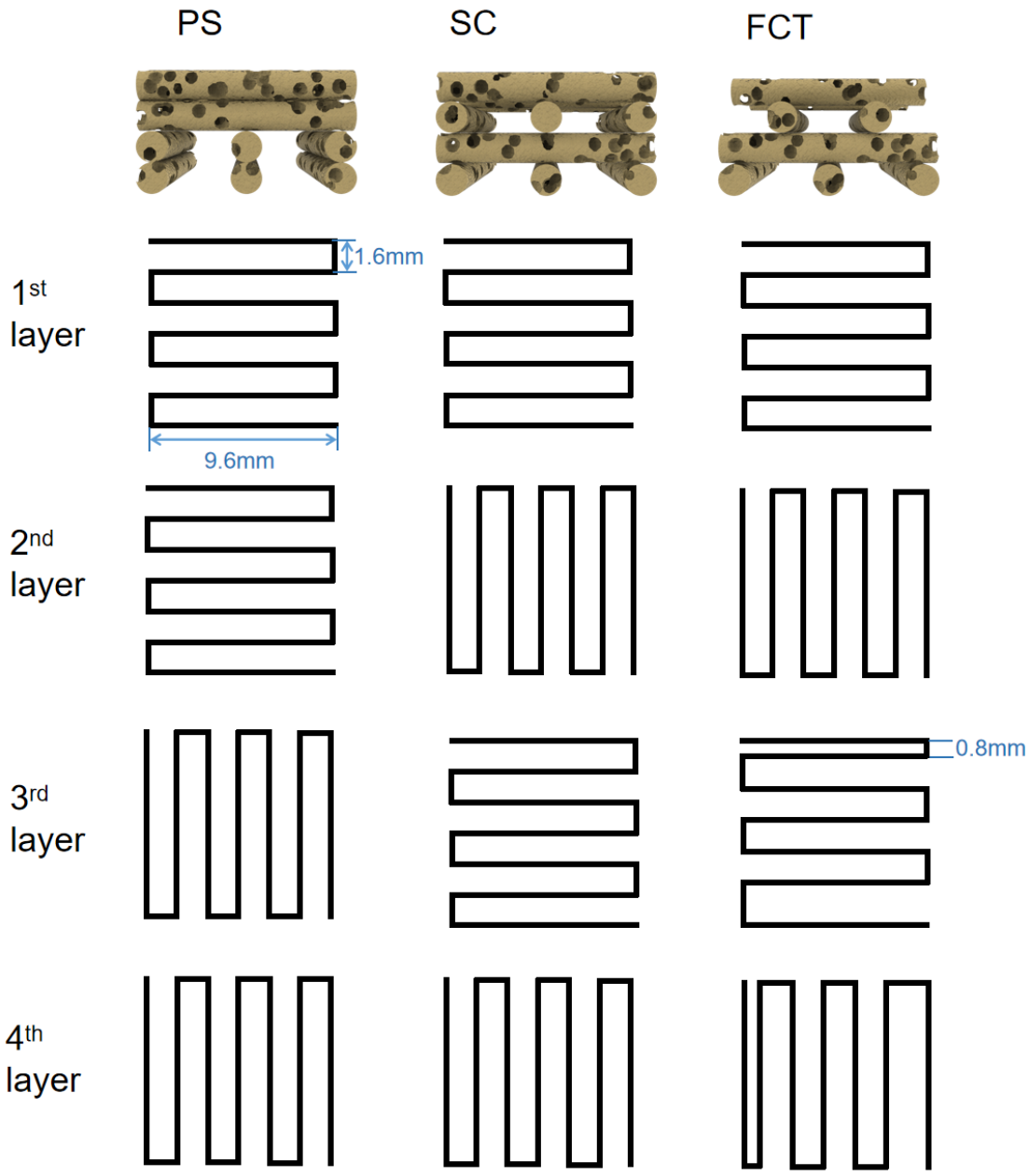

Figure 3.14 Design diagram of lattice structure with different parameters.

The sensitivities and compression simulation by finite element analysis (FEA) are shown in Figure 3.15. With the optimal content of water and CNFs, the FCT structure exhibits the highest sensitivities among them. Different sensitivity of three lattice structures results from the degree of deformability of the lattice structure.

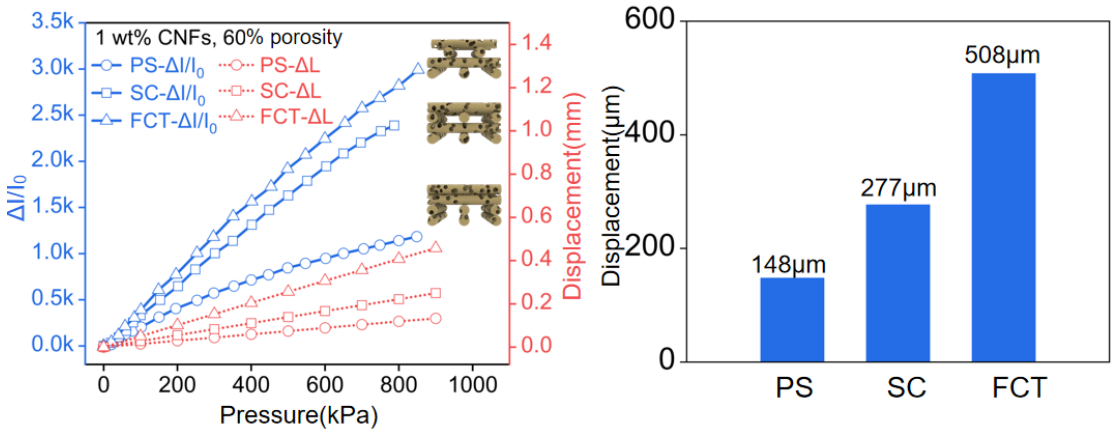

Figure 3.15 Current response and FEA simulation of four layers SC pressure sensor with different lattice structures (PS, SC and FCT).

Then, the finite element analysis (FEA) is performed to analyze the deformation and the stress distribution of three lattice structures, as shown in Figure 3.16. The stress and displacement distribution of PS, SC, and FCT lattice structures under external pressure were simulated using COMSOL software. In simulation, the single lattice rod was set to be 1 mm long and 0.5 mm in diameter, and the distance between two lattice rods was set to be 1 mm. Two plates were given the steel properties to sandwich the lattice structure, and the lower plate remained fixed. A linear compressive force of 1 MPa was applied to compress the lattice structures. In the simulation results, the PS structure has the smallest displacement (ΔL=148 μm), and the FCT structure has the largest displacement (ΔL=508 μm). The simulation result is consistent with the experiment result. Compared with the PS and SC structures, the FCT structure experiences a dominant deformation provided by compressing the staggered rods rather than the vertically aligned rods in the PS and SC structure. So, the stress is homogeneously distributed at the contact sites of each perpendicular stack

layer. In short, based on the above optimization of the HPPS, it is determined that 60 wt% water, 1 wt% CNFs, four layers and the FCT lattice structure are the optimal preparation conditions.

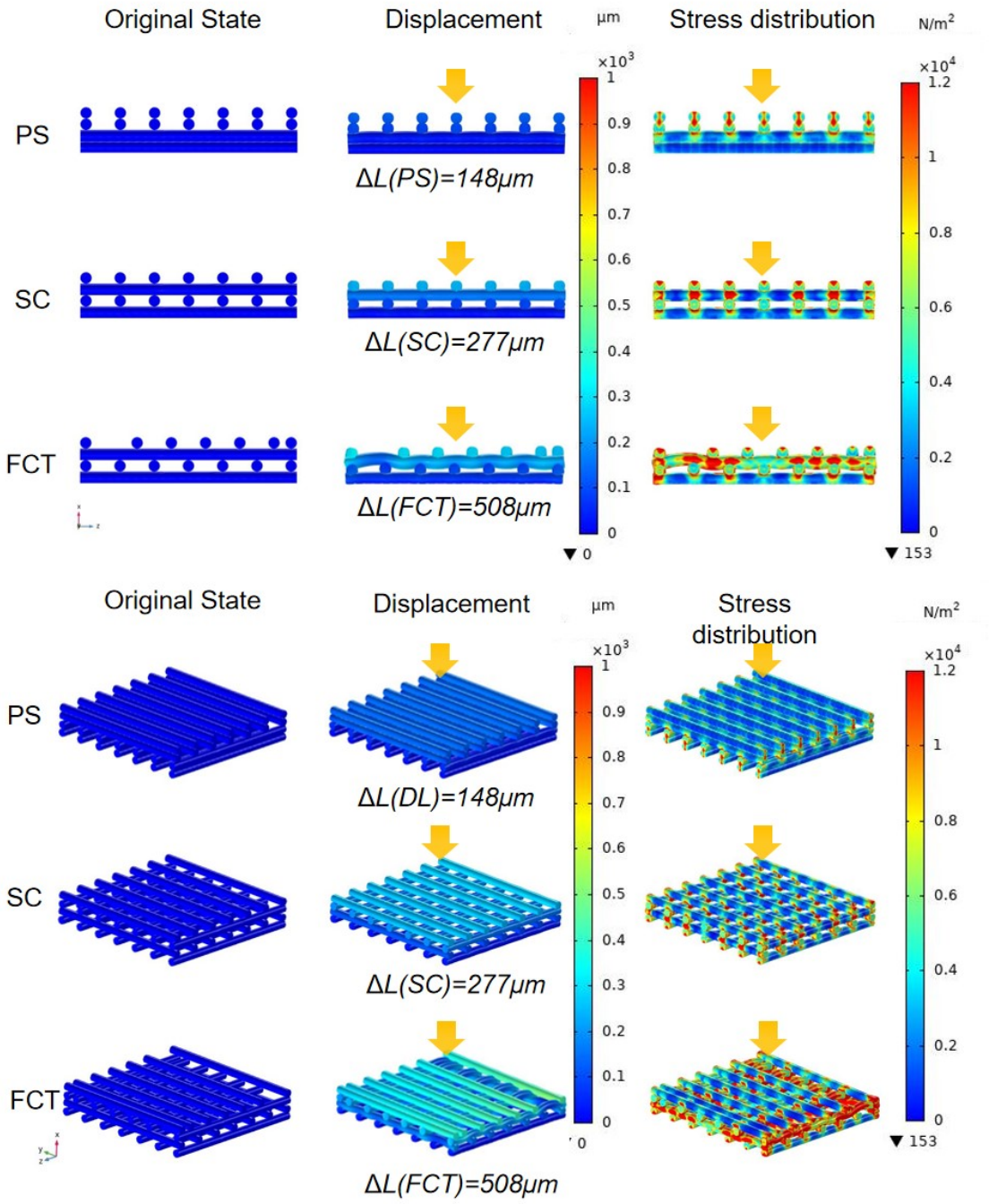

Figure 3.16 Finite element analysis of PS. SC, FCT.

3.5 Conclusion

In summary, we designed a hierarchical in-situ filling porous pressure sensor with high sensitivity and high linearity over a broad sensing range. The DIW printed hierarchical geometry achieves a broad sensing range because the multilayer lattice and internal porous structure increase contact area and distribute applied stress. The strategy of in-situ formation of CNFs networks embedded in inner porous structure provides a significantly and continuously increasing in contact area in each single pore, which results in high sensitivity and high linearity. After optimizing the hierarchical in situ filling porous structure by thoroughly investigating the effect of the porosity, CNFs mass ratio, structure types, stacked sensing layer numbers, and printed lattice types, the hierarchical in situ filling sensor layer with the 4-layer FCT structure composed with 60% porosity and 1 wt.% CNFs has been proven to have the highest sensitivity (4.7 kPa^{-1}) under the broad linear sensing range up to 1 MPa (R^2=0.99).

Chapter 4. Electromechanical performance of HPPS and its applications

4.1 Introduction

In this chapter, the electromechanical performance of the optimized HPPS is comprehensively studied, including detailed sensitivity, detection limit, response time, stability, and durability. Then the sensing mechanism of the hierarchical in-situ filling porous structure is studied by SEM during compression process. The high sensitivity over the broad sensing range can contribute to the CNFs in-situ filling porous structure has a very different morphology and working principles from the conventional porous structure, which led to the better sensing performance of the in-situ filling porous structure. For conventional porous structures fabricated by hard templates or gas foaming method,[29] the conductive fillers are separated and excluded by the hard templates or foaming process, resulting in the conductive filler being dispersed only at the edge of the pores. The large space of the pores hinders the contact of the conductive fillers dispersed at the edges of the pores, resulting in fewer conductive paths being generated. The in-situ filling porous structure is formed by the solidification of CNFs/PDMS and evaporation of emulsified water, while the CNFs dispersed in emulsified water remain inside the pores, forming CNFs networks embedded in the pores. The CNFs networks in-situ filling in porous structure dramatically increases the conductive material contact sites and conductive pathways generation during compression, which achieves high sensitivity and high linearity.

Based on such a hierarchical geometry and secondary CNFs in-situ filling porous structure, the HPPS achieves a high sensitivity (4.7 kPa^{-1}) and high linearity (R^2 =

0.998) over a broad range (0.03–1000 kPa) simultaneously. The high sensitivity and linearity enable the pressure sensor to have a high-pressure resolution. Therefore, the sensor is capable of detecting a low-pressure change (10 kPa) under a high pre-compression of 643 kPa.

Benefiting from the high sensing performance of the HPPS, the sensor is used in detecting various stimuli from low pressure, such as tiny object recognition, pulse detection, and voice recognition, to medium pressure, such as finger bending and human motion detection, to large pressure, such as tire pressure detection. The demonstration of slight pressure changes upon large pre-compression indicated our pressure sensors have a high-pressure resolution. In addition, a smart insole sensor array comprising of 5 sensors located in different positions is employed for plantar pressure sensing to diagnose foot diseases and detect sports biomechanics. With the remarkable sensing performance, we envisage that the hierarchical in-situ filling porous structure can provide a promising design strategy to fabricate high-performance wearable devices for applications in health monitoring, artificial intelligence, human-machine interfaces, robotics, etc.[11,12]

4.2 Methodology

4.2.1 Electromechanical performance characterization of the HPPS

For pressure-sensing performance, the linear motor was set to apply pressure

according to appropriate testing conditions. Two pieces of PMMA square plate with a length of 1cm and a thickness of 1 mm were stuck on the head of the digital force gauge and the head of the linear motor, respectively. The sensor was stuck on the PMMA plate on the head of the digital force gauge. The pressure was recorded by the digital force gauge. Meanwhile, the current was recorded in real-time using a LabVIEW controlled digital source meter (Keithley 2611B). The source-drain voltage was 0.1 V, except for the high-pressure resolution demonstration, which was 0.07 V. The *I-V* curves were measured by an electrochemical analyzer (CHI660E) in the pressure range of 0 kPa to 600 kPa. For the high-pressure resolution test, tiny object pressure sensing test, voice recognition, pulse detection, and high-pressure resolution demonstration, the current was recorded using an electrometer (Keithley 6514).

The 3×3 cm^2 sensor was used for the high-pressure resolution demonstration, and the 1×1 cm^2 sensor was used for all other tests and demonstrations. The sensitivity (S) was calculated according to the following equation (12):

$$S=\frac{\Delta I/I_0}{\Delta P} \text{ or } \frac{\Delta R/R_0}{\Delta P}$$

Where I_0 is the initial current of the sensor without pressure loading, and ΔI is the current changes of the sensor under a fixed pressure change (ΔP).

4.2.2 Finite element analysis simulation

The stress and displacement distribution of PS, SC, and FCT lattice structures under external pressure were simulated using COMSOL software. The single lattice

rod was set as 1 mm long and 0.5 mm in diameter, and the distance between two lattice rods was set as 1 mm. Two plates were given the steel properties to sandwich the lattice structure, and the lower plate remained fixed. A linear compressive force of 1 MPa was applied to compress the lattice structures. The material model of lattice structure was set as linear elastic material. The sequence type of meshing was set as physics-controlled mesh, and the element size of meshing was set as normal.

4.2.3 Fabrication of smart flexible insole

The foot-shaped PET film was used as the substrate of the smart flexible insole, and it was fabricated by a laser cutting machine (4060, FST) based on the designed pattern in CorelDRAW software. The five HPPS were fixed on the five positions of the PET film with double-side tape, including 1st phalanx (#5), 5th metatarsal (#4), 1st metatarsal (#3), Medial cuneiform (#2), and Posterior calcaneus (#1).

4.3 Electromechanical performance of HPPS

The sensing performance of the HPPS under different pressing conditions is studied. The synergetic effect of in-situ filling internal porous structure and lattice structure enables the sensor to exhibit high sensitivity and high linearity over a broad pressure-sensing range. As shown in Figure 4.1A, the HPPS prepared with the optimized condition (1 wt% CNFs, 60 wt% water with FCT structure) achieves a high

sensitivity of 4.7 kPa^{-1} and high linearity with the correlation coefficient of 0.998 in the broad pressure range from 0.032 kPa to 1000 kPa. In comparison with the previously reported piezoresistive pressure sensors in Figure 4.1B, our HPPS exhibits an incomparable high sensitivity and a broad linearity range of pressure.[7,125,127,131–149] To the best of our knowledge, the simultaneous achievement of such a high sensitivity of 4.7 kPa^{-1} over such a broad linear range from 0.03 kPa to 1000 kPa has never been reported before. The dynamic response speed of the sensor is measured by suddenly pressing with a 17 kPa force, followed by a quick release. The response and relaxation time are 24 ms and 15 ms (Figure 4.1C), respectively, which are comparable to the response time of human skin (30–50 ms). The HPPS exhibits a low detection

limitation of 32 Pa, as shown in Figure 4.1D, which indicates the HPPS is able to detect very small mechanical stimuli.

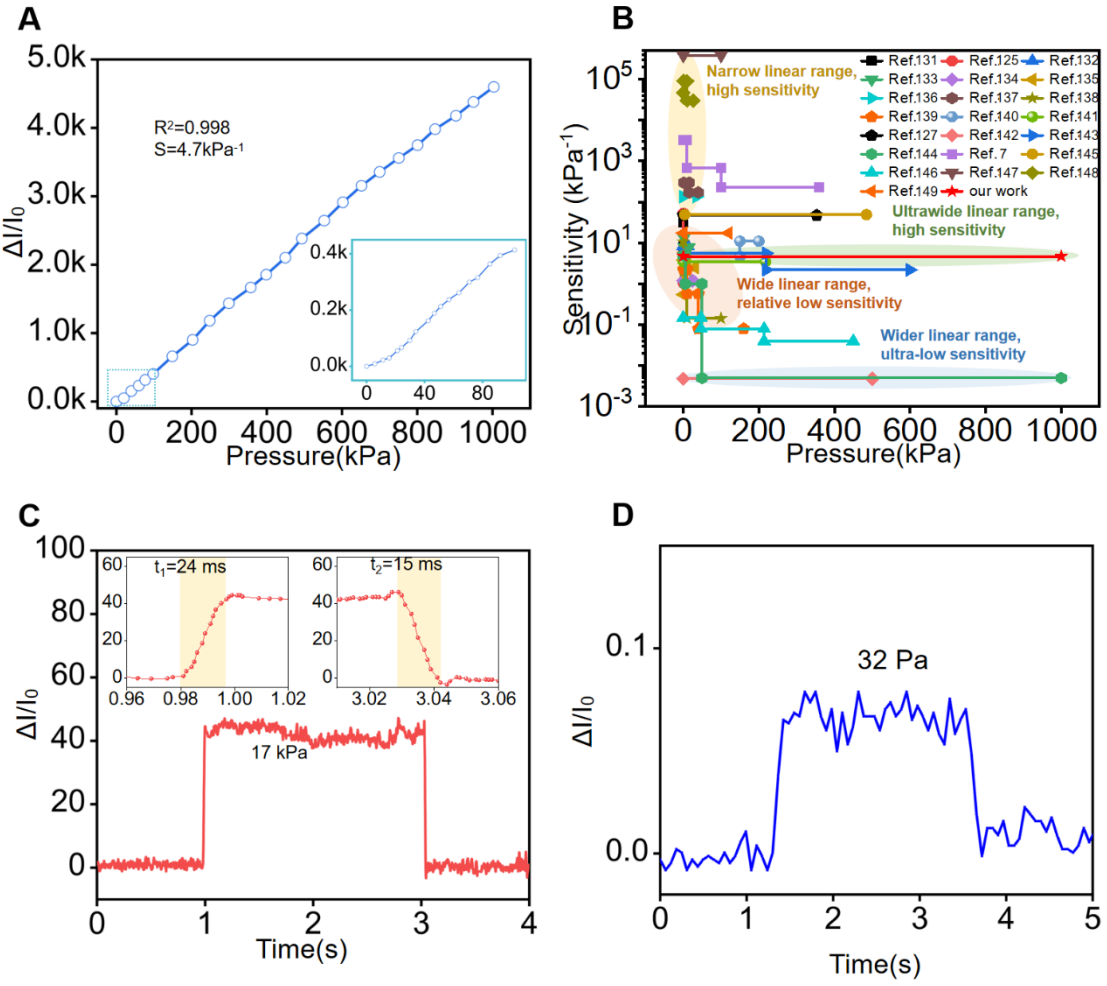

Figure 4.1 (A) Relative current change based on the optimized sensing layer under different pressures (0.032 kPa–1000 kPa). (B) Comparison of the sensitivity of our pressure sensor with other reported literatures. (C) Response and recovery times of the HPPS under the pressure of 17 kPa. (D) The relative current change under the subtle pressure of a half peanut.

The current-voltage (*I-V*) curves of the pressure sensor from −3 V to 3 V under different pressures display a linear relationship, indicating that the HPPS possesses

ohmic contact characteristics (Figure 4.2A), and has a stable sensing performance under various static pressures. As the pressure increases from 0 to 600 kPa, the resistance decreases dramatically. The relative current change of the sensor under six incremental pressure loading/unloading cycles is measured to investigate the dynamic pressure sensing performance (Figure 4.2B). The pressure sensor exhibits a steady signal and a transient response to the cyclic loading/unloading process, indicating that the pressure sensor is capable of working stably in a wide range of dynamic cyclic pressure. The effect of loading frequency should also be considered for evaluating the stability of dynamic pressure sensing performance. As depicted in Figure 4.2C, the relative current change exhibits no frequency dependence or delay under a constant pressure of 100 kPa with different frequencies from 0.2 to 5 Hz. The high sensitivity and high linearity under a broad pressure range enable the pressure sensor to exhibit high-pressure resolution. The pressure sensor could detect the slight pressure change under high pre-compression. Figure 4.2D depicts the synchronous change of current and pressure. At first, the sensor is compressed to 643 kPa as the reference P_0, and then the incremental slight pressures (10 kPa, 21 kPa, and 32 kPa) were added in sequence. The results show that the sensor has the ability to differentiate the incremental slight press under a large pre-compression.

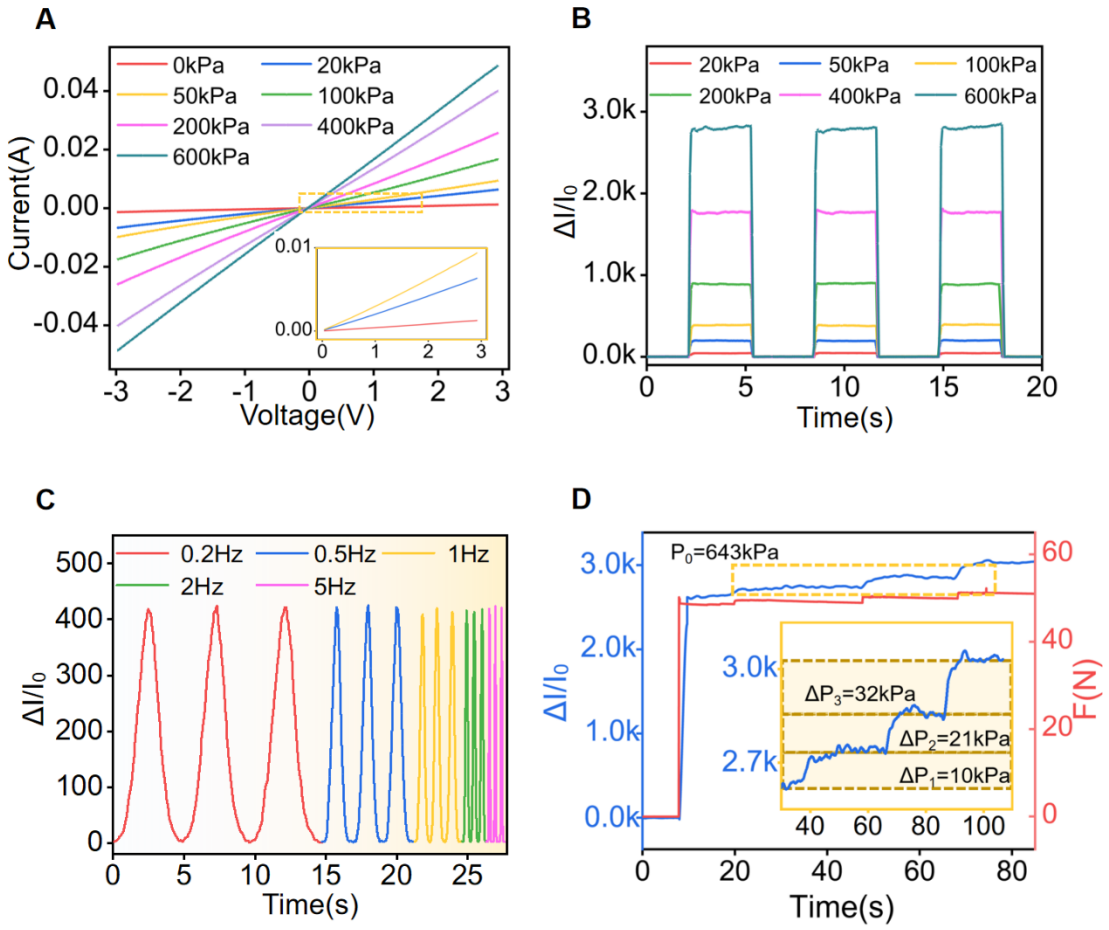

Figure 4.2 (A) Current-voltage curves of the HPPS under different pressures. (B) Dynamic response of the HPPS under loading/unloading cycles from low pressure to high pressure. (C) Dynamic response of the HPPS under 100 kPa at different frequencies. (D) Detection of tiny pressure under pre-compression of 643 kPa.

As illustrated in Figure 4.3, the pressure sensor exhibits high reproducibility and durability under the pressure of 28 kPa, 50 kPa and 200 kPa during 35,000 cycles, respectively. In the inset figure, the signal shows that there is no obvious amplitude change in the cycle test.

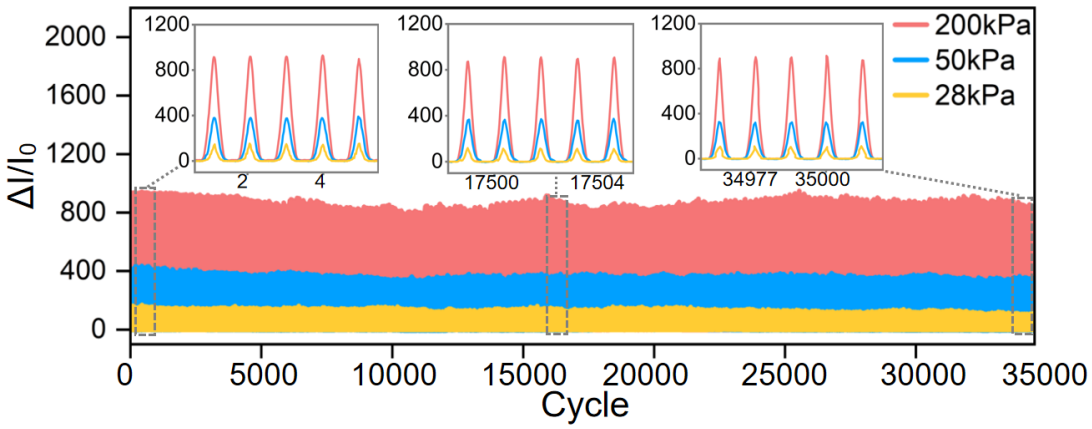

Figure 4.3 Repeatability performance of HPPS over 35000 loading/unloading cycles under the pressures of 28 kPa, 50 kPa, and 200 kPa respectively.

To study the reproducibility of the pressure sensor, the error bar studies in terms of pressure range and sensitivity were conducted by measuring 8 sensors in Figure 4.4 and Table 4.4. All eight sensors have very close sensitivity values over a wide sensing range of 1 MPa. Furthermore, all eight sensors exhibit very high linearity. There is no significant deviation in sensitivity and linearity, which implies the good reproducibility of the pressure sensor.

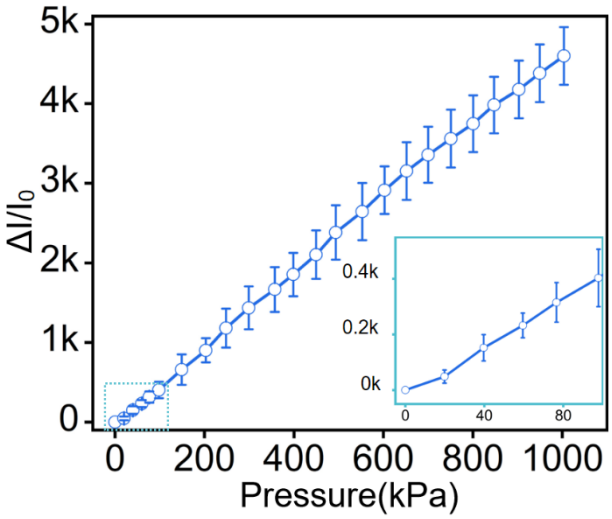

Figure 4.4 Relative current change with error bars based on the optimized sensing layer under different pressures.

Table 4.4 The sensitivity and linearity of eight different samples.

	Sensitivity(kPa^{-1})	**Linearity R^2**
Sample-1	5.01	0.994
Sample-2	4.96	0.995
Sample-3	4.75	0.998
Sample-4	4.74	0.998
Sample-5	5.03	0.997
Sample-6	5.08	0.998
Sample-7	4.86	0.998
Sample-8	5.04	0.993

4.4 The Sensing Mechanism of HPPS

The synergic effect of multilayer structure and hierarchical in-situ filling porous structure enables the pressure sensor to exhibit high sensitivity and high linearity over

a broad pressure range. In order to understand the high-performance sensing mechanisms of HPPS, micromechanics compression test and in-situ SEM imaging are performed. For all the following SEM images, the compression direction is vertical (up to down). Figure 4.5A–I visualizes the cross-sectional views of structure evolution at 0%, 26%, and 63% compression at different scales. The schematic illustration of the detailed sensing mechanism is depicted in Figure 4.5J–M and Figure 4.6.

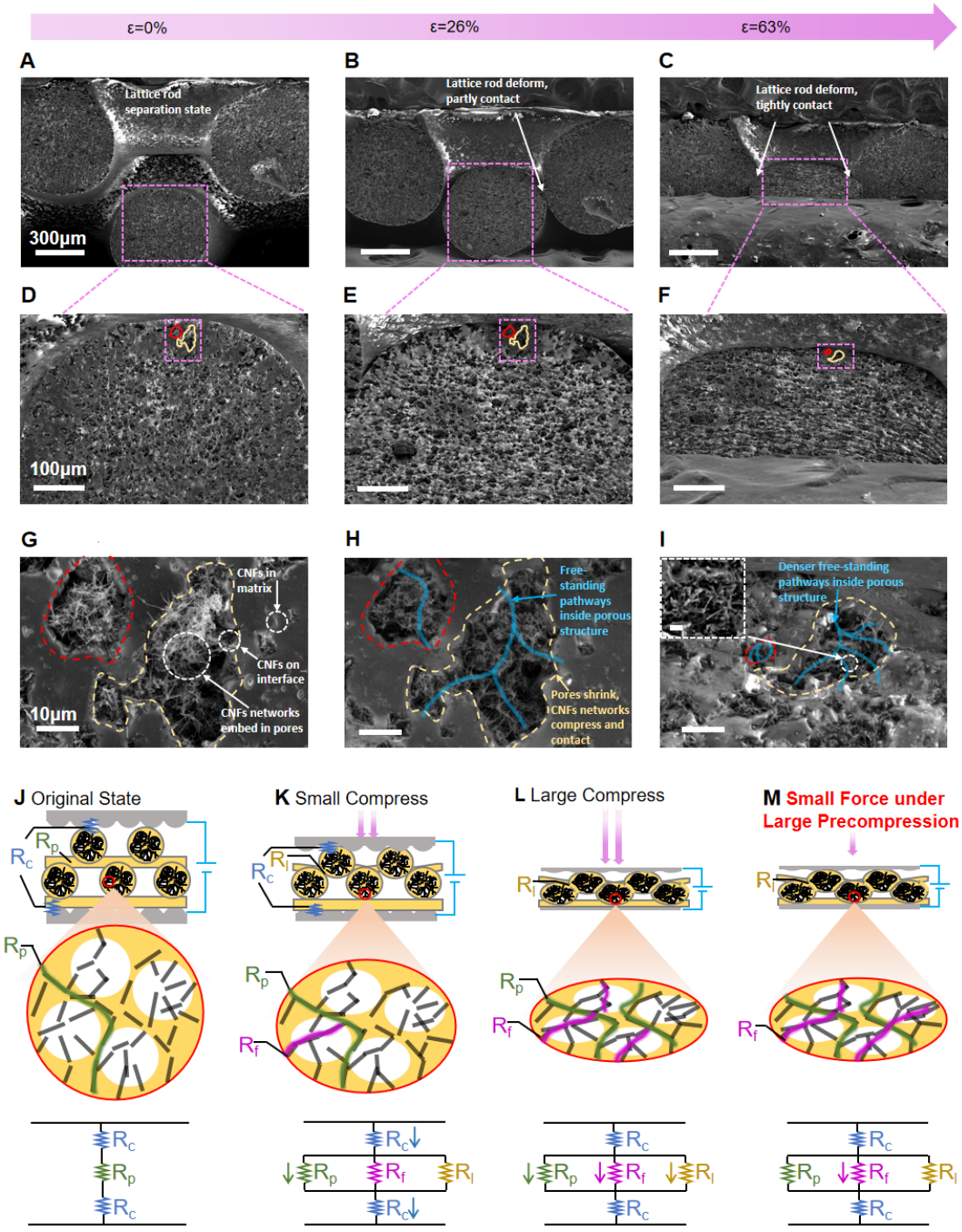

Figure 4.5 Cross-sectional SEM images of lattice structure at (A) original state, (B) compression of 26%, (C) compression of 63%. Cross-sectional SEM images of the porous structure at (D) original state, (E) compression of 26%, (F) compression of 63%. Cross-sectional SEM images of the CNFs networks embedding in a single pore at (G) original state, (H) compression of 26%, (I) compression of 63%. Schematic

illustration and circuit diagram of sensing mechanism of HPPS under (J) small compression, (K) medium compression, (L) large compression. m A tiny pressure change under a large preload is used to illustrate the high pressure resolution performance.

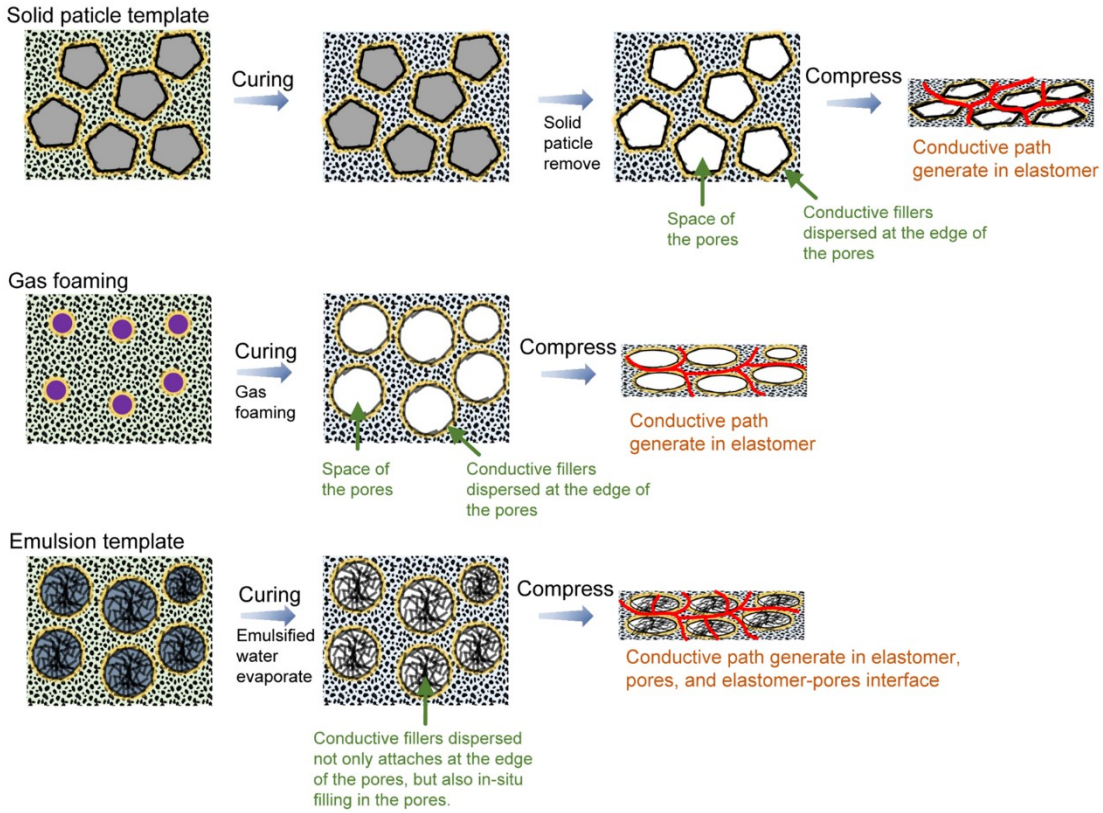

Figure 4.6 Schematic illustration and comparison of porous structures formation by emulsion template method, sold particle template method, and gas foaming method. The schematic illustration of pressure sensing mechanisms of porous structures prepared by three different methods.

Figure 4.7 visualizes the interface between the sensing layer and the Ni electrodes. The wavy textile microstructure of Ni electrodes forms fewer initial contact points

with the sensing layer, which results in high contact resistance in the unloaded state. Figure 4.5A, 4.5D, 4.5G and 4.5J illustrate the morphology of multilayer lattice and hierarchical in-situ filling porous structure before compression. The space between stacked layers makes the lattice structure highly compressible (Figure 4.5A). The in-situ filling porous structure formed by emulsion template method results in CNFs networks that exist in the PDMS matrix, on the interface, and embedded in pores (Figure 4.5D and 4.5G). This could create more contact sites among CNFs networks during compression, resulting in high sensitivity over the sensing range.

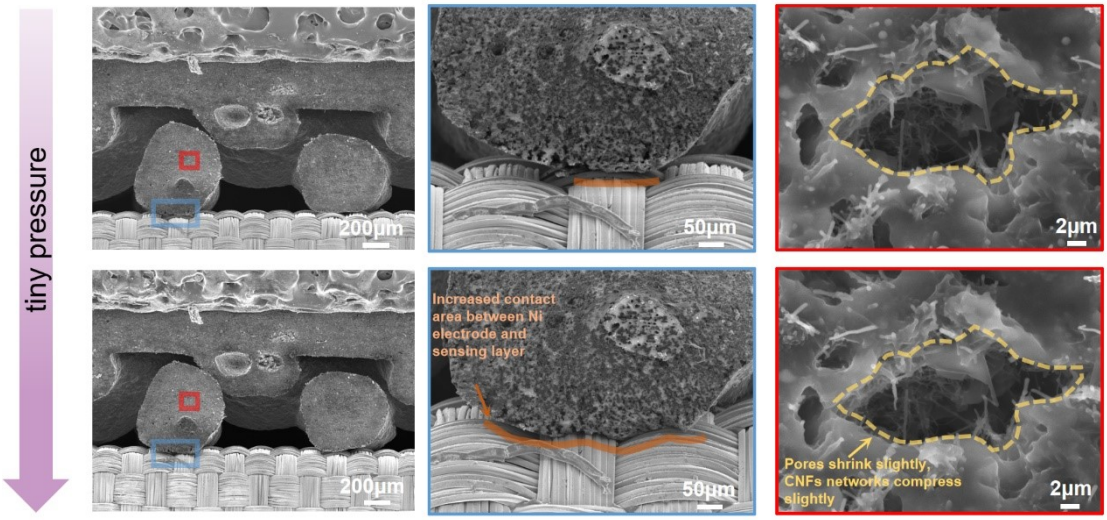

Figure 4.7 In situ SEM images of structural deformation of hierarchical in situ filling porous structure under a tiny pressure.

At very low compression, shown in Figure 4.7, the contact area (orange line) between the Ni electrodes and sensing layer increases significantly, resulting in a decrease in contact resistance under low pressure. In addition, the internal pores compress slightly, and CNFs networks embedded in porous structure slightly contact

each other, generating some conductive pathways that increase the current. As shown in Figure 4.8, a comparison experiment of the effects of a wavy textile microstructure electrode and a flat Cu electrode on the sensing performance under low pressure is conducted to prove that the Ni electrodes can improve the sensing performance in low pressure range. Furthermore, there is no significant deviation in sensitivity between the low pressure (4.64 kPa^{-1}, < 500 Pa) and high pressure range (4.7 kPa^{-1}, < 1 MPa), which further confirms the high sensitivity and linearity over the entire sensing range.

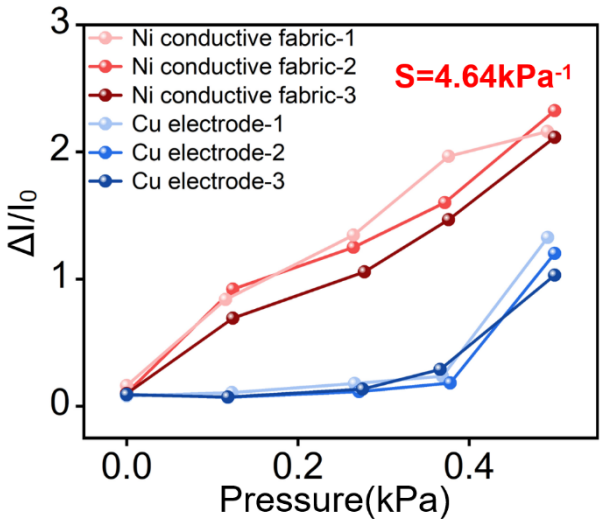

Figure 4.8 The sensing performance of sensors fabricated using Ni conductive fabric and Cu electrodes at low pressure range.

At 26% compression (Figure 4.5B, 4.5E, 4.5H and 4.5K), the lattice rods deform and partly contact each other to create more conductive pathways. Comparing with the single-layer structure, the multilayer structure has a larger contact area change and effective stress distribution, thereby generating more conductive pathways during compression.[150] This is also verified in the pressure sensitivity comparison test of the

HPPS with different numbers of layers (Figure 3.11). In the high magnification SEM images of Figure 4.5E and 4.5H, inner pores (red dash line, yellow dash line) begin to shrink, and CNFs networks embedded in porous structure contact each other to build up more conductive pathways. The introduction of in-situ filling porous structure further improves sensitivity and linearity. This can be proved by the results in Figure 3.10, where the sensitivity of lattice structure with internal porous structure is higher than the lattice structure without it.

Herein, a schematic illustration of Figure 4.6 is used to interpret the high-performance mechanism of in-situ filling porous structure compared with other kinds of conventional hollow porous structure. The superiority of our in-situ filling porous structure to conventional porous structures is caused by different morphologies and different working principles. For conventional porous structures, which are usually fabricated by hard templates (like sugar, salt, and other solid particle templates) or gas foaming method, the conductive fillers are separated and excluded by the hard templates or foaming process. This results in the conductive filler only being dispersed at the edge of the pores. When applied with a slight pressure change, the large space of the pores hinders the contact of conductive fillers dispersed at the edge of the pores, which results in most conductive paths generating only in the elastomer. Therefore, for conventional porous sensors, the resistance change is relatively small over the entire sensing range. For our in-situ filling porous structure fabricated by soft emulsion template method, the CNFs can disperse inside the soft template when mixed with PDMS emulsion. Then, during the high temperature curing

process, the emulsified water evaporates, while the CNFs dispersed in emulsified water remain inside the pores, forming CNFs networks embedded in the pores. This led to the conductive fillers not only attaching at the edge of the pores but also in-situ filling in the pores. When a slight pressure change is applied, the CNFs networks embedded in internal porous structure can easily contact each other to generate free-standing conductive pathways in the internal pores. In addition, the CNFs networks could also serve as a 'bridge' to connect the separated conductive filler dispersed at the edges of the pores to form more conductive pathways. This result in the conductive path could generate in elastomer, pores, and elastomer-pores interface. Therefore, a more significant resistance change can be induced over the entire sensing range. A comparison of sensing performance of the in-situ filling porous sensor with conventional porous sensor with the same porosity and same ratio of CNFs is conducted to further prove the superiority of in-situ filling porous structure to conventional porous structure (Figure 4.9).

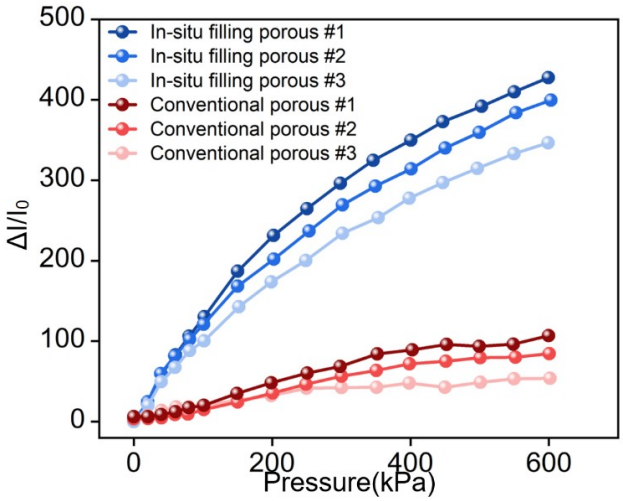

Figure 4.9 The comparison of the sensitivity of in situ filling porous sensor and conventional porous sensor.

At 63% compression (Figure 4.5C, 4.5F, 4.5I and 4.5L), the further deformation and tight contact of lattice rods will generate more conductive pathways and reduce resistance. In the high magnification SEM images of Figure 4.5F and 4.5I, the pores further shrink, and the CNFs networks embedded in porous structure are compressed to form more conductive pathways. During the entire process of compression, conductive pathways are continuously generated due to the gradual contact of in-situ filling CNFs networks in microscale and deformation and contact of lattice rods in macroscale.

As can be observed from Figure 4.5I and 4.5M, even at a highly compressed of 63%, there are still some nano-scale gaps between each carbon nanofiber due to the mesh characteristics of the CNFs networks. Thus, upon huge pre-compression, a slight pressure change could still induce some conductive pathways to be generated in nanoscale CNFs networks. This can be demonstrated by the result in Figure 4.2D.

The total resistance of HPPS is expressed in terms of the sum of the resistance of the sensing material (R_p, R_f) and contact resistance (R_c, R_l). In theory, the total resistance is expressed as follows equation (13):

$$R_{total} = 2R_c + \frac{R_p * R_f * R_l}{R_p * R_f + R_p * R_l + R_f * R_l}$$

where R_c denotes the contact resistance between the sensing layer and the electrode, R_l denotes the contact resistance between the neighboring interlocked lattice rod, R_p denotes the resistance of the conductive pathways generated in the PDMS matrix, and R_f denotes the resistance of the free-standing pathways generated inside the porous structure.

4.5 Applications

4.5.1 Wearable device and high-pressure resolution demonstration

Due to the high sensitivity and high linearity over a broad range, the pressure sensor can be used in various applications. As presented in 4.10A, different slight pressures are detected and distinguished to verify the high sensitivity and high-pressure resolution of the HPPS. In order to detect the slight pressure, adhesive tape is used to fix the sensor tightly on the table. The light objects' weights, from a grain of rice (0.022 g) to a tiny screw (0.7 g), are detected and distinguished based on the difference of the current change. Next, the pressure sensor is used to recognize different voices (Figure 4.10B). As shown in the inset, the sensor is attached on the throat to detect the subtle vibration when the volunteer speaks. The words 'good' and 'morning' correspond to characteristics of the current change pattern, indicating that the sensor is capable of distinguishing different voices. The word 'good' is repeated five times to demonstrate its repeatability.

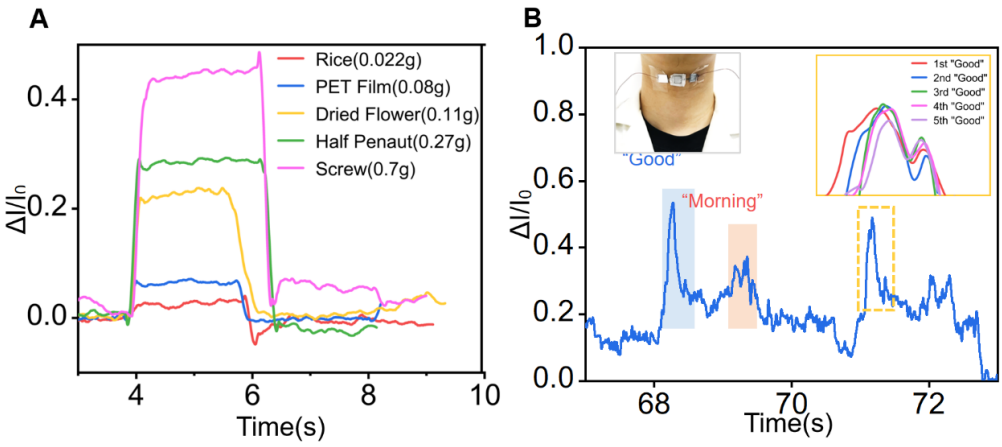

Figure 4.10 (A) Transient response to the loading/unloading light objects. (B) Monitoring of throat vibration when pronounced "Good morning". The repeatability of recognizing the same word "Good" five times, as shown in the inset image.

Due to its high sensitivity, the sensor can be used to detect the wrist pulse period and waveform in real-time when it is attached to the wrist skin by the medical tape (Figure 4.11A). As illustrated in Figure 4.11B, the arterial pulse could be read accurately under both normal conditions (66 beats per minute) and after exercise (108 beats per minute). Meanwhile, each periodic pulse with three distinguishable characteristic peaks can be accurately recognized in both states: percussion wave (P), tidal wave (T), and diastolic wave (D) (Figure 4.11C).

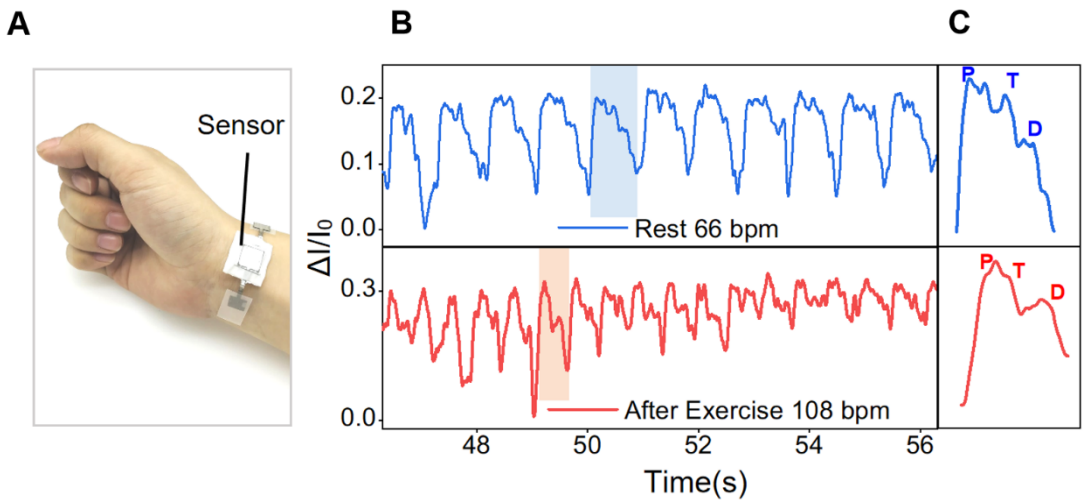

Figure 4.11 (A) HPPS is attached to the wrist to monitor the (B) wrist pulse of a healthy person before and after exercise, and (C) the enlarged single pulse signal contains characteristic peaks: P-wave, T-wave, and D-wave.

This suggests that the HPPS could potentially apply in healthcare monitoring and disease diagnosis. In addition, the angle of finger bending could also be accurately measured by fixing the HPPS to the finger joint, as depicted in Figure 4.12A. When the bending angle of the finger gradually changes, the current change exhibits a stepwise increase. The current change remains constant when the finger maintains a certain angle, and it returns to the original value when the finger restores to the original position (Figure 4.12B).

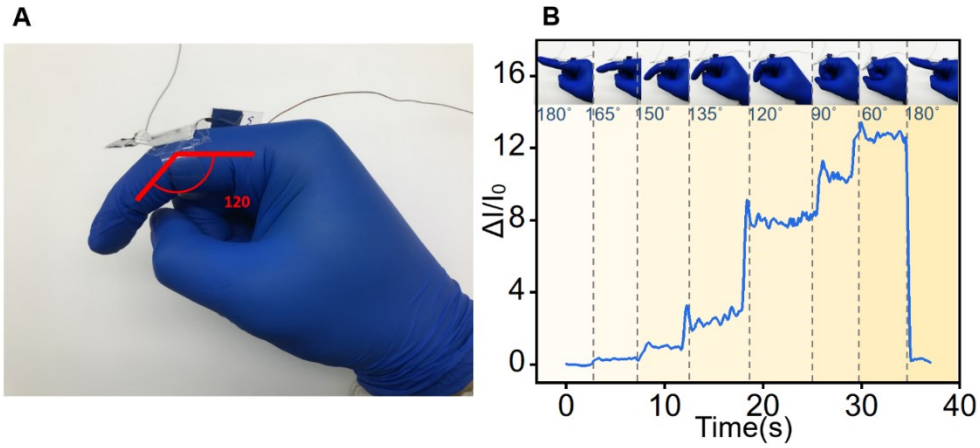

Figure 4.12 (A) HPPS is fixed on the index finger joint for monitoring finger bending angle. The angle of finger bending is defined as shown in the figure. (B) Monitoring finger bending with different angles.

Beside the sensing capability in the low-pressure range, such as arterial pulse monitoring, voice recognition, and finger joint bending detection, the HPPS could also be applied in some high-pressure scenarios. As shown in Figure 4.13A, the pressure sensor is fixed on the sole to detect the different motion states. Different motions, including walking, brisk walking, running, and jumping, could be distinguished according to the sharpness, frequency, and intensity of the signal. The sensor can be utilized to measure tire pressure while riding a bicycle, as shown in Figure 4.13B. When riding a bicycle with inflated tires, the tires generate large pressure on the sensor, which results in a large current signal. When the tire is out of air, the contact area of the tire with the ground becomes larger, resulting in a decrease in the pressure of the tire on the sensor. Sensors with a wide range can potentially be applied to the tactile perception of human-machine interfaces to detect small pressures such as blowing and touching, and then larger pressures such as stabbing and

smashing (Figure 4.13C).

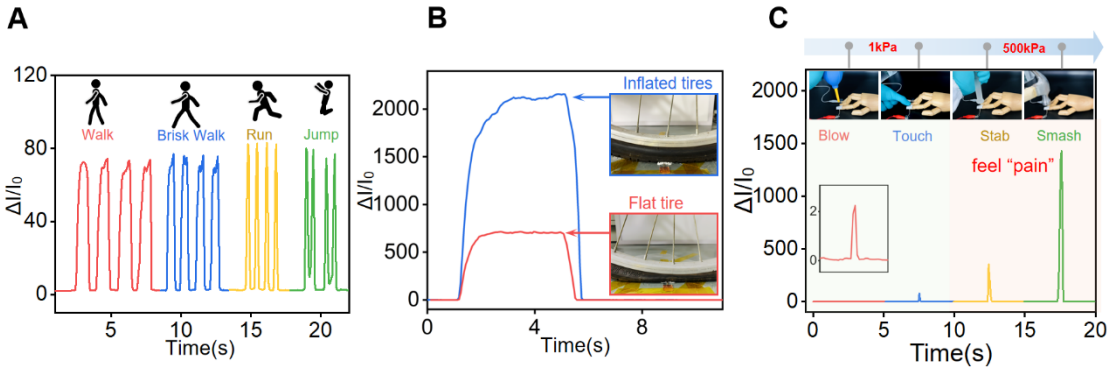

Figure 4.13 (A) Real-time recording of human motions, including walking, brisk walking, running and jumping. (B) Measuring the tire pressure while riding a bicycle. (C) Tactile recognition of different magnitudes of force, including blowing, touching, stabbing, and smashing.

Benefiting from the high sensitivity and a broad linear range of sensing capability, the HPPS exhibits high pressure resolution. Then, the pressure sensor is used as an electronic balance to verify the linear sensitivity at high pressure, as depicted in Figure 4.14A. The square PET plate is placed on top of the sensor to bear the weight, and four small columns are located at four corners to stabilize the PET. When three incremental weights (20 g, 40 g, and 60 g) were sequentially loaded under 0 kg and 3 kg pre-loading weights, the current changes for each 20 g mass increase in both cases exhibit the same value, indicating the good linearity of the pressure sensor under high pressure. Above all, the HPPS has great potential in detecting the incremental small press under a large pre-compression.

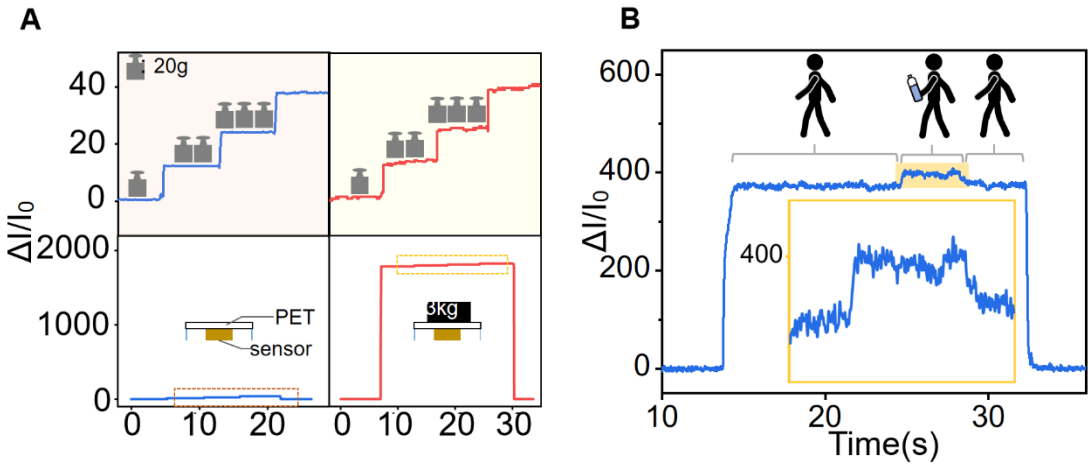

Figure 4.14 (A) Measuring the three 20 g weight changes in sequence under the pre-loading weights of 0 and 3 kg. (B) Measuring the tiny pressure change of a bottle of water under the preload of a human weight.

In Figure 4.14B and 4.15, a 2.5×2.5 cm^2 pressure sensor is used to demonstrate the high-pressure resolution characteristics under a broad pressure range. As shown in Figure 4.14B, an 80 kg male stands with one foot on the pressure sensor, and then a bottle of water (550 g) is placed on his hand. The whole process, including the slight pressure change due to the addition of a bottle of water, can be detected by the current change. Moreover, the HPPS demonstrates its high-pressure resolution in some high pressure scenarios (Figure 4.15). As shown in Figure 4.15A, the front wheel of a car (1700 kg) is first pressed on the sensor as pre-compression. When a male (80 kg) is getting on the car, the increased pressure leads to a stepped increase of the current change. When the car leaves the pressure sensor, the signal instantly returns to its original state. As shown in Figure 4.15B, a lighter object (a box of bottled water, 6 kg) is placed on the car. The entire process, including the weight change of a box of

bottled water, could be accurately recorded through the obvious signal change. The signal oscillations (marked in red circle) in the inset of Figure 4.15A and 4.15B indicate the slight vibration and movement while a man and a box of water were loaded on the car.

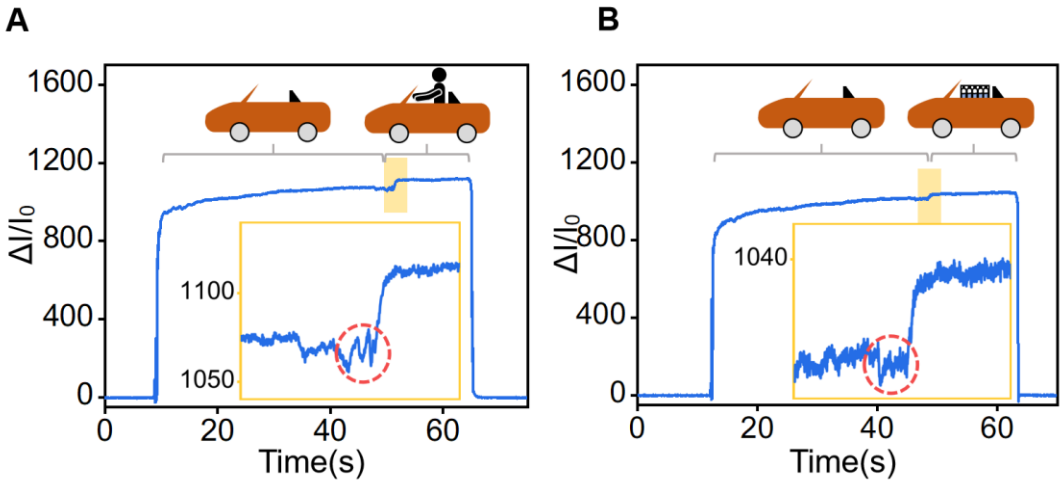

Figure 4.15 Measuring the pressure change of (A) a human and (B) a box of water under the preload of a car weight.

4.5.2 Plantar pressure distribution monitoring

Plantar pressure distribution monitoring is of great significance in podiatric disease prevention and diagnosis, injury prevention, gait analysis, sports biomechanics, etc. For instance, abnormal gait and walking posture may cause excessive local pressure in certain areas of the foot, which can lead to various diseases such as plantar fasciitis, diabetic foot ulcers, etc.[151,152] The typical abnormal gaits, including supination and pronation, are shown in inset images in Figure 4.17B and 4.17C. Except for

congenital supination and pronation, some acquired cases result from wearing unfit shoes, being overweight, having calcium deficiency, or having poor walking habits. For the acquired supination and pronation, it is difficult to prevent and diagnose the disease at an early stage.[153]

Herein, our highly sensitive over broad range pressure sensor is capable of accurately detecting plantar pressure distribution, which can be used to diagnose abnormal gait at an early stage. The high linearity of pressure sensor is able to clearly distinguish the pressure intensity of different local areas. As shown in Figure 4.16A, five pressure sensors are integrated into the smart insole. Each sensor is placed at corresponding areas of posterior calcaneus (#1), medial cuneiform (#2), 1st metatarsal (#3), 5th metatarsal (#4) and 1st phalanx (#5). The evolution of pressure distribution map during dynamic waking process (heel strike, mid stance and toe-off) is reconstructed from the acquired signals, as shown in Figure 4.16B.

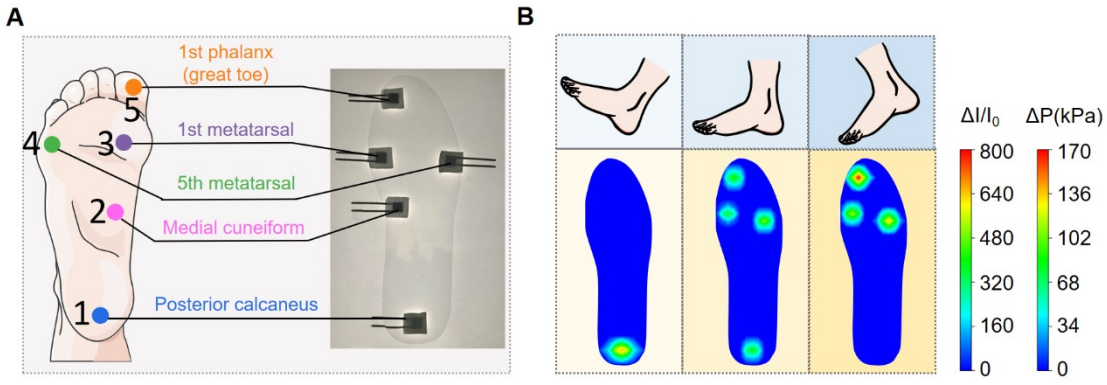

Figure 4.16 (A) Optical image of HPPS array on smart insole and corresponded anatomy in the schematic illustration of the human foot. (B) Evolution of the pressure distribution mapping during dynamic waking process.

Figure 4.17A–C demonstrate and compare the current variation and corresponding calculated pressure as a function of time for three different walking gaits: neutral, supination and pronation. For neutral gait (Figure 4.17A), the #1 sensor signal increases first due to the heel touching the ground. Then the #3,4 sensor signal rise indicates the mid stance, and finally, the #5 sensor signal growth suggests that the heel lift in the final stage. For supination gait (Figure 4.17B), the signal of sensor #4 is much higher than sensor #3 which indicates a shift of barycenter to the outside of the foot (5th metatarsal). In the case of pronation (Figure 4.17C), the shifting of barycenter to the inside of the foot leads to a higher signal in sensor #3 (1st metatarsal). In addition, the early stage of pronation gait results in a slightly flat foot, which causes the arch slightly to deform to touch the #2 sensor (medial cuneiform), as shown in the inset image in Figure 4.17C. Therefore, the high sensitivity of the pressure sensor enables to identification of minor gait abnormalities, thereby realize diagnose of pronation and supination in the early stage. The high linearity of the pressure sensor could easily distinguish three different walking gaits by comparing the plantar pressure distribution.

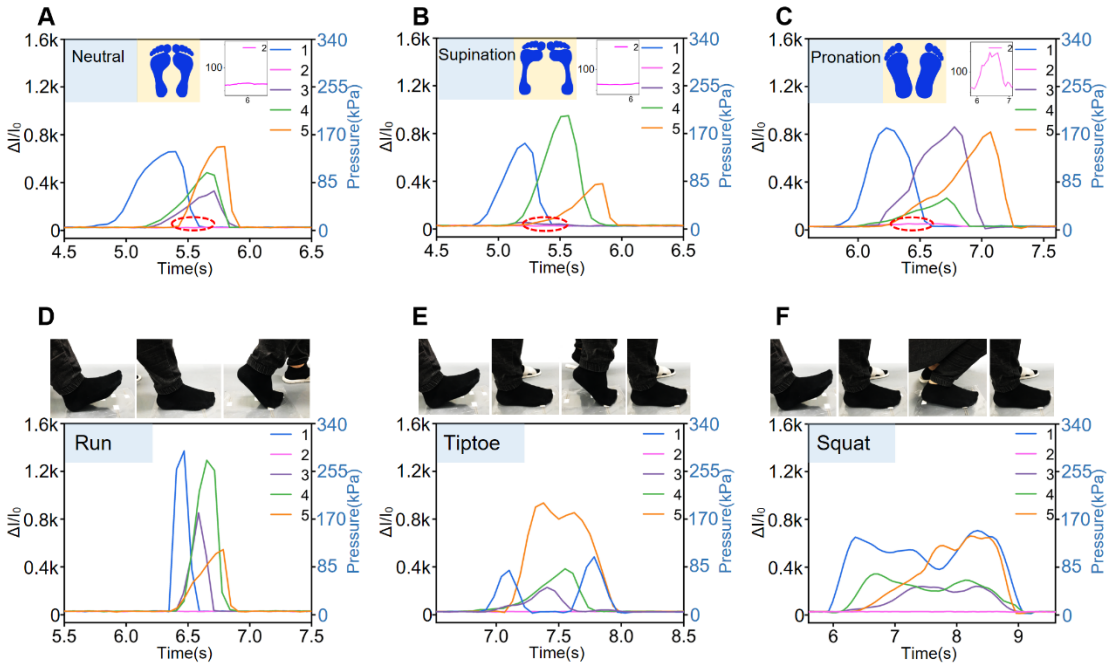

Figure 4.17 Real-time recorded current variations and corresponding calculated pressure of the five sensors to detect the walking posture of three different people with (A) neutral gait, (B) supination gait, and (C) pronation gait, respectively. Real-time recorded current variations and corresponding calculated pressure of the five sensors to recognize the sports biomechanics of (D) running, (E) standing on tiptoe, and (F) squatting, respectively.

In addition to prevention and diagnosis of foot diseases, our sensor can also be applied to sports biomechanics detection (Figure 4.17D–F). Compared with normal walking (Figure 4.17A, step speed: 48 steps per minute), a larger current signal and higher frequency are observed during running (Figure 4.17D, step speed: 100 steps per minute). During the process of standing on tiptoe (Figure 4.17E), more pressure is concentrated on 1st phalanx, which causes an intense signal in sensor #1. During the squatting process (Figure 4.17F), the signal experience constantly changes because of

the altering barycenter. The above results indicate that the high sensitivity and high linearity over the broad range pressure sensor have outstanding potential in wearable medical devices and sports equipment for real-time monitoring purposes.

4.6 Conclusion

In conclusion, the optimized HPPS achieves high sensitivity (4.7 kPa^{-1}) and high linearity (R^2 = 0.998) over a broad range (0.03–1000 kPa). These sensing capabilities enable the pressure sensor to detect diverse stimuli from low pressure such as tiny object recognition, pulse detection, and voice recognition, finger binding detection, and human foot motion in medium pressure regimes, tire pressure monitoring in high pressure regions. Moreover, the sensor is able to detect a low pressure change under high compression because of its high-pressure resolution. With the outstanding performance of the pressure sensor, it can be applied to personal electronics and biomedical devices in the near future. In addition, this cost-effective fabrication method of hierarchical in-situ filling porous structure provides a general design strategy for other types of sensors.

Chapter 5. Fabrication of WMS

5.1 Introduction

The wearable and stretchable sensing electronics with the mechanical stimuli sensing capabilities attract tremendous attention due to their promising application in personal health monitoring,[154–156] electronic-skin,[157–159] human-machine interface[160–162] and robotics.[163,164] For steadily and accurately perceiving physical signals, a series of significant progress has been made in developing high-performance wearable sensors with excellent sensitivity,[150,165] stretchability,[13,14] robustness,[15,16] broad sensing range,[17,18] etc.[19] However, most of the developed wearable sensors are optimized for detecting only uniaxial mechanical deformation (such as lateral stretch or pressure) and cannot monitor and differentiate multiple mechanical stimuli. The sensing features of these sensors exhibit the same electrical output tendency under different mechanical stimuli such as pressure, stretching, bending and twisting. As a result, the measurement of one directional mechanical stimulus will be interfered with by stimuli coming from other directions, indicating the inability to sense and differentiate between multiple mechanical stimuli. This severely limits its use in practical applications where the detection and differentiation of a variety of complex mechanical stimuli are essential.

To address the interference caused by the mechanical stimuli coming from different directions, a typical strategy is to fabricate a wearable sensor that is sensitive to mechanical stimuli from only one direction while being insensitive to others. Oh et al. developed a porous pressure insensitive strain sensor.[166] The working mechanism is that pressure is working primarily to close the pores while having no effect on

CNTs network, and the lateral stretching causes microcracks occur within the carbon nanotube network, leading to a change in resistance. On the other hand, some research on strain insensitive pressure sensors has also been reported. A hierarchical micropyramid array structure with a stiffening microelectrode was developed that produces contact area changes and capacitance change only under pressure but not under tension.[167] Although these devices reduced interference from mechanical stimuli coming from other directions, they were unable to detect mechanical signals coming from other directions. Therefore, there is a strong need to develop sensors that can not only differentiate multiple mechanical signals but also monitor them simultaneously. So far, some wearable sensors with the multiple mechanical stimuli sensing and differentiating ability have been developed. Bao et al. designed a stretchable, porous e-skin to detect and harvest a variety of mechanical stimuli based on three independent electric signals.[168] According to Zhu et al., a dual-interdigital-electrode sponge sensor was fabricated with the capability of identifying multiple mechanical stimuli by measuring the resistance signal of the top and bottom interdigital electrodes.[169] However, these sensors with multiple mechanical stimulus sensing capabilities still suffer from many drawbacks, such as low sensitivity in different sensing directions, a narrow sensing range, and a complex fabrication process.

Herein, a wing-like structured, high sensing performance WMS is designed to precisely detect and differentiate multiple mechanical stimuli, including pressure, stretch, convex and concave bending. The wing-liked structure is composed of

pressure sensing module in the middle and stretch sensing module in both wings. The pressure sensor module is assembled from a hierarchical in situ filling porous sensing layer and the PDMS substrate pasted with interdigital electrode. The structural feature of the hierarchical in situ filling porous pressure sensing layer is the in-situ filling porous structure formed by emulsion template method, and hierarchical porous structure prepared by DIW printing technique. This high density of CNFs in-situ filling in porous structure and the huge deformability of hierarchical porous structure result in outstanding pressure sensitivity. Then we optimize the pressure sensing module by investigating the sensing layer, which is composed of different concentrations of CNFs. For stretch sensing module in both wings, the high stretch sensing performance is achieved by the pre-stretch treatment and preparation of 1D CNTs and 2D Ag nanoflakes conductive network in the sensing layer. The wrinkled CNT-Ag nanoflakes hybrid film results in high sensitivity over a broad stretching sensing range. The effect of different concentrations of CNTs and Ag nanoflakes, and the effect of pre-stretch treatment are investigated to optimize the stretch sensing module.

5.2 Methodology

5.2.1 Materials

Carbon nanofibers (CNFs, model XFM60, purity > 95 wt%, diameter of 50–200 nm, length of 1–15 μm), carbon nanotubes (diameter of 8–15 nm, length of 50 μm),

and Ag nanoflakes (~5 μm) are obtained from XFNANO Materials Tech Co., Ltd. The PDMS (Sylgard 184) with curing agent and Ecoflex 00-30 were bought from Dow Corning Co., Ltd. Paraffin liquid was obtained from Sinopharm Chemical Reagent Co., Ltd. Ethanol (ACS, purity > 99.5%), 1,1,1,3,3,3-HexafluoroHexafluoro-22-propanol (99.5%), propanol (99.5%), and N-hexane (AR, 97%) were purchased from Aladdin Co., Ltd. Conductive silver resin from Aladdin Co., Ltd. Conductive silver paint (SPI# 05001Paint (SPI# 05001-AB) was purchased from SPI Supplies. Conductive resin adhesive was purchased from Beijing Jianlong Electronic Chemical Co., Ltd. Polyurethane was purchased from Beijing Jianlong Electronic Chemical Co., Ltd. Polyurethane masterbatches (TPU) were purchased from BASF Comasterbatches (TPU) were purchased from BASF Co., Ltd.

5.2.2 Fabrication of wrinkled CNTs/Ag hybrid film for the stretch sensing module

-Fabrication of substrate and electrodes

The overall substrate is composed of PDMS in the middle and Ecoflex in both wings. For the fabrication of middle PDMS part, firstly, a 1.2 x 1.6 cm^2 PMMA mold is fabricated by laser cutting machine (4060, FST) based on the designed pattern in CorelDRAW software. Then, the PDMS was thoroughly mixed with curing agent in a ratio of 5:1, pouring and coating in the PMMA mold. The coated PDMS solution is

cured in an oven at 80℃ for 2 h. For the fabrication of Ecoflex in both wings, the cured PDMS middle part was first placed in the middle part of a 1.2 x 4 cm^2 PMMA mold. The Ecoflex part A and part B were mixed thoroughly with a ratio of 1:1, pouring and coating in both sides of the placed PDMS part. The coated Ecoflex solution is cured in an oven at 60℃ for 2 h.

The interdigital conductive fabric electrode was engraved by laser cutting machine according to the designed pattern. Then the interdigital electrode was pasted on the PDMS.

-Preparation of the CNTs/Ag nanoflakes dispersion

The CNTs, Ag nanoflakes dispersion was prepared by dispersing CNTs and Ag nanoflakes in ethanol with ultrasonic and magnetic stirring for 0.5 h, respectively. Three different concentrations of CNTs/Ag nanoflakes dispersion (CNTs: Ag nanoflakes = 1:0.5, 1:1, and 1:2) were prepared by mixing CNTs and Ag nanoflakes dispersion, followed by ultrasonic dispersing and magnetic stirring for 0.5 h.

-Fabrication of wrinkled CNTs/Ag stretch sensing layer

The substrate was pre-stretch with 50% and fixed on a PMMA mold fabricated by laser cutting machine. Both ends of the pre-stretched substrate were fixed on both ends of the PMMA mold by the clamp. The prepared CNTs/Ag dispersion was transferred into the PMMA mold by pipette. The dispersion was dried at 80℃ for 10 minutes to form a CNTs/Ag nanoflakes hybrid film. The PMMA mold was removed, and the pre-stretched strain was released to form a wrinkled CNTs/Ag nanoflakes hybrid film. The inner end of wrinkle hybrid film is coated on the interdigital

electrode. Paste the conductive fabric with conductive silver paint on the outer ends of the wrinkled CNTs/Ag nanoflakes hybrid film in both wings. The wrinkled CNTs/Ag nanoflakes hybrid film was encapsulated with Ecoflex and cured at 60℃ for 2 hours.

5.2.3 Fabrication of hierarchical in situ filling porous structure

-Preparation of CNFs/PDMS emulsion

The PDMS emulsion is prepared by stirring the 5 g of PDMS, 0.5 g of curing agent, and 5 g of paraffin liquid with a high-shear dispersing machine (FS400-S, LICHEN Co., Ltd.) under high-speed stirring at 1200 rpm. Meanwhile, 14 g of ultrapure water was added dropwise at a rate of 48 ml/h into the PDMS/paraffin liquid mixture using a microfluidic syringe pump (SP-1000, Ningbo Annuo Medical Apparatus, and Instruments Technology Co., Ltd.). A white and creamy PDMS emulsion was obtained after all the water was added to the PDMS/paraffin liquid mixture. Second, the CNFs were added into the PDMS emulsion in batches under vigorous mechanical stirring by using a high-shear dispersing machine to form a black and creamy CNFs/PDMS emulsion as the DIW printing inks.

-Fabrication of CNFs/PDMS sensing layer

The CNFs/PDMS hierarchical in situ filling porous sensing layer was printed using pneumatic extruding DIW printing (SHOTmini200ΩX, Musashi Engineering, Inc.). The lattice structure was printed based on the 3D model designed in the DIW printer.

The optimized setting parameters were as follows: the diameter of the nozzle was 0.6 mm, the moving speed of the printing head was 6 mm s^{-1}, and the extrusion pressure was controlled within the range of 50–80 kPa. After printing, the CNFs/PDMS sensing layer was cured at 80℃ for 2 h, and then the cured sensing layer was washed twice with n-hexane and ethanol, respectively. The washed sensing layer was dried for 2 h at 100℃. Finally, the dried CNFs/PDMS sensing layer was assembled on the interdigital electrode and encapsulated by TPU film. The TPU film is prepared by electrospinning 4 wt% TPU dissolved in 1,1,1,3,3,3-Hexafluoro-2-propanol.

5.2.4 Characterization

The morphologies and elemental mapping of CNFs/PDMS hierarchical in situ filling porous sensing layer and wrinkled CNTs/Ag nanoflakes hybrid film were characterized using scanning electron microscopy (SEM, JCM-7000 NeoScope) with a voltage of 5 kV. A computer-controlled linear (LinMot) motor was used to perform pressure and stretch sensing tests.

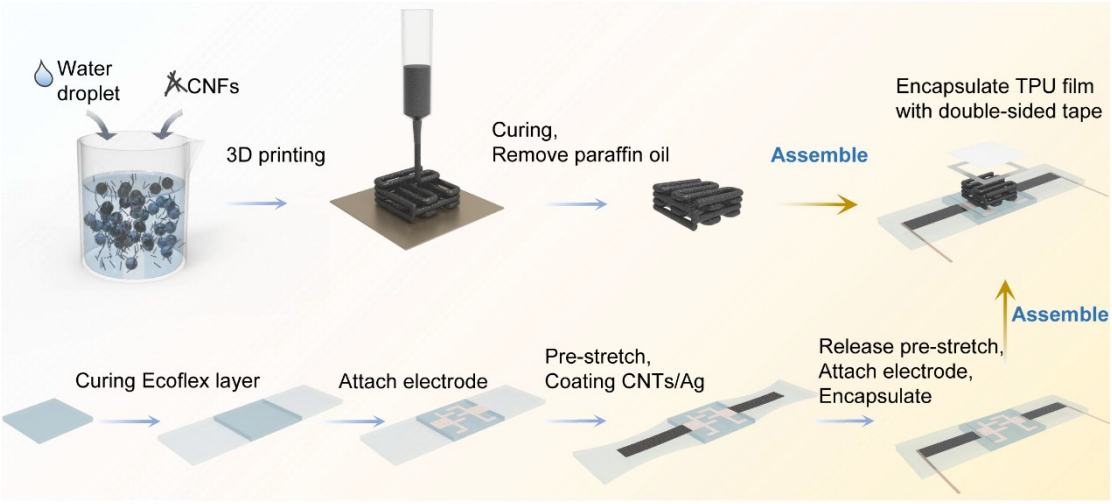

Figure 5.1 Schematic illustration of multifunctional sensor fabrication.

5.3 Structural design and morphology studies of WMS

The fabrication process of WMS is illustrated in Figure 5.1, Figure 5.2 and methodology, which consist of pressure sensing module and stretch sensing module. According to our previous report,[33] the hierarchical in situ filling porous sensing layer in the pressure sensing module was prepared by emulsion template method and direct ink writing (DIW) printing technique. Firstly, the PDMS emulsion is prepared by adding ultrapure water dropwise to PDMS/curing agent/paraffin liquid mixture under vigorous mechanical stirring. Then, the CNFs were added into the PDMS emulsion in batches under vigorous mechanical stirring by using high-shear dispersing machine. The CNFs/PDMS emulsion serves as the ink for DIW printing. The CNFs/PDMS lattice structure is 3D printed based on the designed 3D model in DIW printer. After the printed sensing layer was cured at 100 °C for 2 h and washed with n-hexane and

ethanol to remove the residual paraffin liquid.

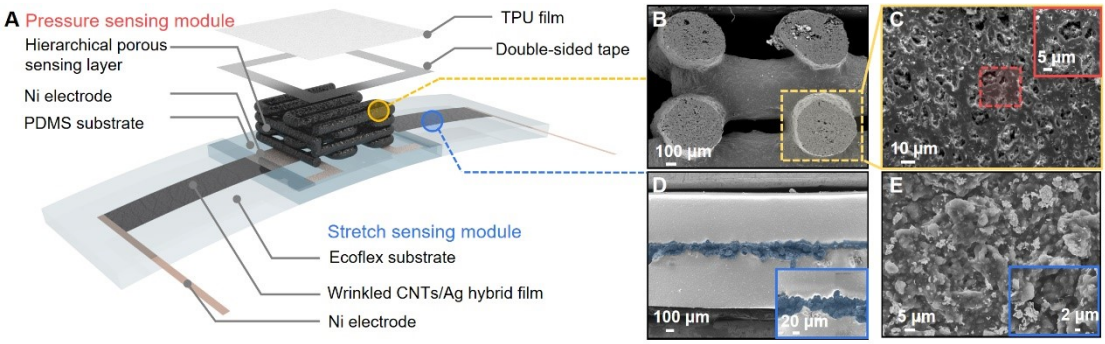

Figure 5.2 (A) Structural schematic of WMS. (B, C) Cross-sectional SEM images of the pressure sensing layer at different magnifications. (D, E) The cross-sectional (D) and top viewed (E) SEM images of the stretch sensing layer at different magnifications.

The morphology of hierarchical in situ filling porous pressure sensing layer was studied by SEM in Figure 5.2B and 5.2C. Figure 5.2B presents the cross-sectional SEM image of the lattice structure, consisting of stacked lattice rods with a distance of approximately 200 μm. In the magnified SEM images of Figure 5.2C and inset, the CNFs networks in-situ filled in the internal porous structure of a single lattice rod formed by emulsion template method. This in-situ filled structure is formed by the curing of CNFs/PDMS lattice structure. During the curing process, CNFs dispersed in emulsified water remain in the pores as the emulsified water evaporates, forming CNF networks embedded in the pores. The lattice structure and internal porosity make the sensing layer highly compressible, while the CNFs in-situ filling porous structure increases the generation of conductive pathways during compression.

For stretch sensing module, the whole substrate is composed of PDMS in the

middle and Ecoflex in both wings. The interdigital electrode, fabricated by laser cutting machine, was pasted on the PDMS. The stretch sensing layer is made with wrinkled CNTs/Ag nanoflakes hybrid film. Firstly, the CNTs/Ag nanoflakes dispersion was prepared by mixing CNTs and Ag nanoflakes in ethanol under ultrasonic and magnetic stirring for 30 min. Then, the CNTs/Ag nanoflakes dispersion was transferred onto the 50% pre-stretched substrate and dried at 80 °C for 10 minutes to prepare a CNTs/Ag nanoflakes hybrid film. The wrinkled CNTs/Ag nanoflakes hybrid film is formed after releasing the pre-stretched substrate. The morphology of the wrinkle structure is studied by a cross sectional SEM image in Figure 5.2D, and the thickness of the sensing layer was approximately 50 μm. The top viewed SEM image (Figure 5.2E and elemental mapping in Figure 5.3) confirmed the 1D CNTs and 2D Ag nanoflakes were uniformly distributed on the substrate. The conductive fabric electrode was connected to the ends of the wrinkled CNTs/Ag nanoflakes hybrid film on both wings by conductive silver paint. After that, the hybrid film and electrode were encapsulated with Ecoflex. Finally, the prepared CNFs/PDMS hierarchical in situ filling porous sensing layer was assembled on the interdigital electrode by encapsulating it with TPU membrane.

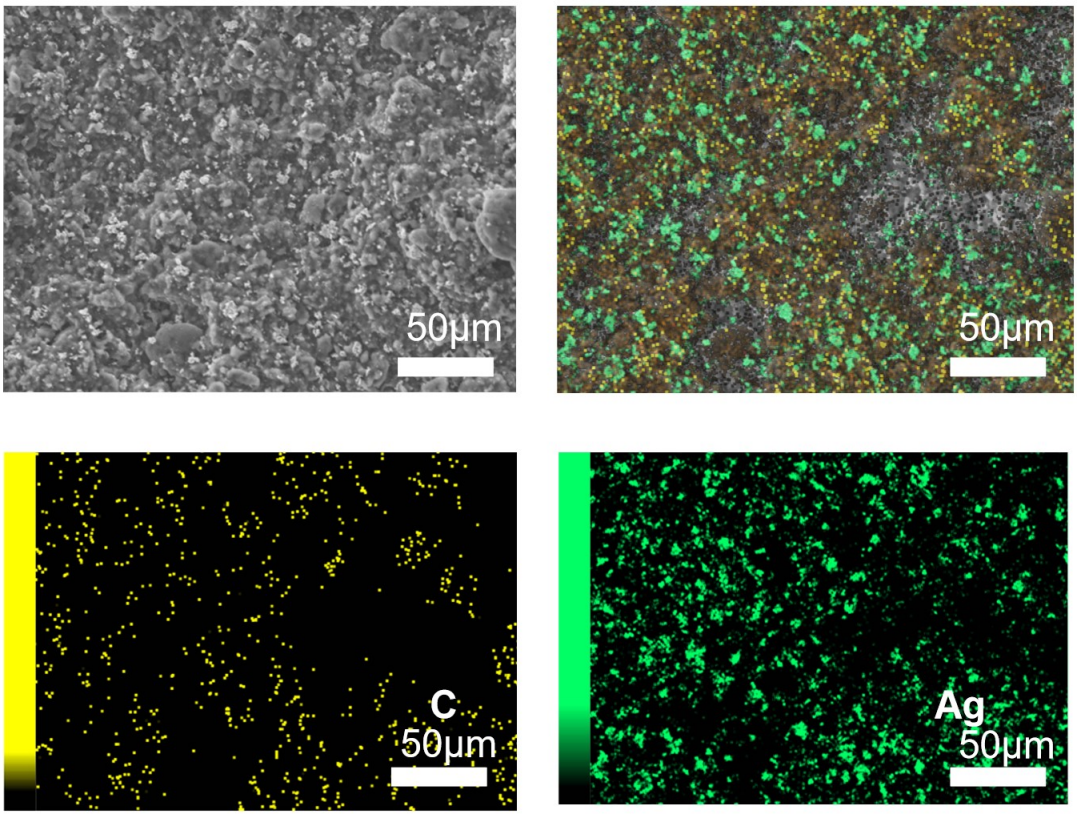

Figure 5.3 Top viewed SEM image and elemental mapping of stretch sensing layer, C element in yellow, Ag element in green.

The photographs of hierarchical in-situ filling porous sensing layer, stretch sensing module and assembled WMS are shown in Figure 5.4A, 5.4B and 5.4C. These fabrication strategies based on hierarchical in situ filling porous pressure sensing layer and wrinkled CNTs/Ag nanoflakes stretch sensing layer enable the WMS to exhibit highly sensitive and broad sensing ranges in both pressure and stretch sensing, compared with other multifunctional sensors (Figure 5.5).[33,102,168–172]

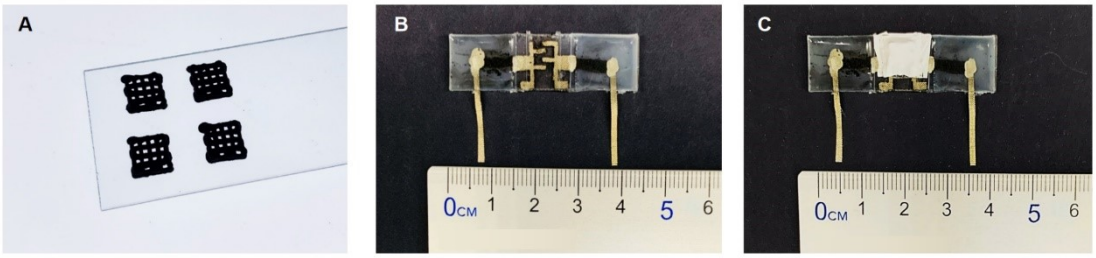

Figure 5.4 Photograph of (A) hierarchical porous sensing layer. (B) stretch sensing module. (C) WMS.

The high degree of stretchability and bendability (Figure 5.6A) enables the WMS to conform well to the human body, such as attached to the finger (Figure 5.6B). Furthermore, during the stretching process shown in Figure 5.6C, the WMS exhibits outstanding stretchability while keeping the pressure sensor module from deforming. Meanwhile, the pressure applied to the pressure sensing module does not cause deformation of the stretching sensing module. (Figure 5.6D) This ensures that the stretch and pressure sensing module will not be affected by each other when they work independently. As depicted in Figure 5.6E, the WMS can detect and differentiate the multiple mechanical stimuli, including pressure, stretch, convex and concave bending, through different resistance and current variation trends.

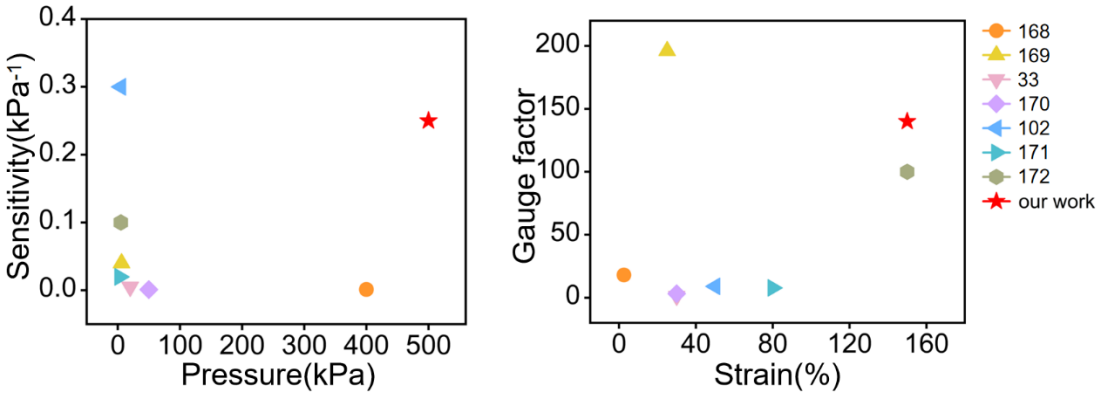

Figure 5.5 Comparison of the pressure sensing sensitivity and stretching sensing gauge factor of our multifunctional sensor with other reported multifunctional sensors.

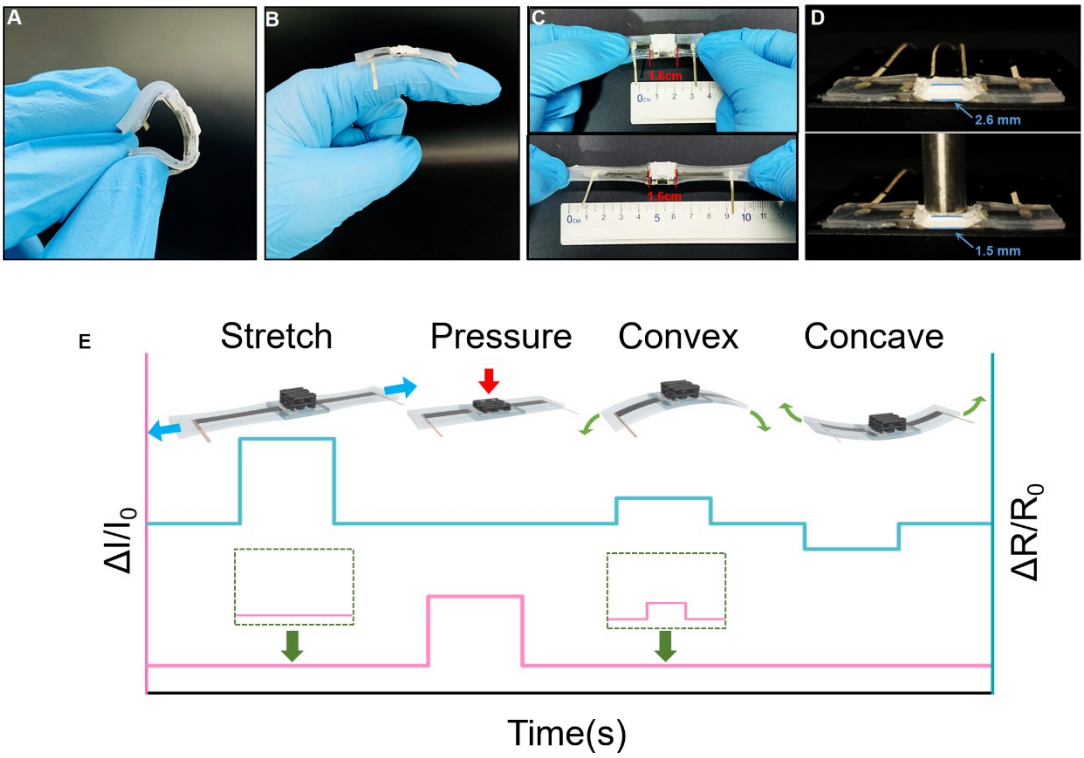

Figure 5.6 (A) Photography of the WMS shows the bendability. (B) Photographs of the sensor attached to a finger. (C) Photograph of the WMS under 0% and 150% stretch. (D) Photograph of the WMS with and without pressure. (E) Schematic diagram of the sensing signal of the WMS to different mechanical stimuli.

5.4 Optimization of the sensing performance of stretch and pressure sensing module

The layout of the wing-like multifunctional sensors is shown in Figure 5.7. The sensing performance of the stretch sensing module was evaluated by measuring the relative resistance change ($(R - R_0)/R_0$) under a specific applied strain. Its sensitivity can be evaluated by the gauge factor ($GF = (R - R_0/R_0)/\varepsilon$)). The sensor is mounted on a linear motor to perform with different strains, while the digital multimeter is connected to the sensor to record the resistance (as shown in Figure 5.8). The sensing performance of the pressure sensing module is studied by the relative current variation ($(I-I_0)/I_0$) under different applied pressures. The sensor is attached to a digital dynamometer, which records the pressure applied by the linear motor, while the sensor is connected to a digital multimeter, which records the current under pressure (Figure 5.8).

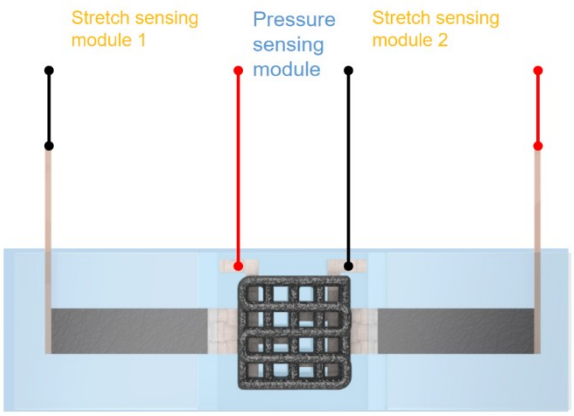

Figure 5.7 Schematic diagram of wing-like multifunctional sensor layout.

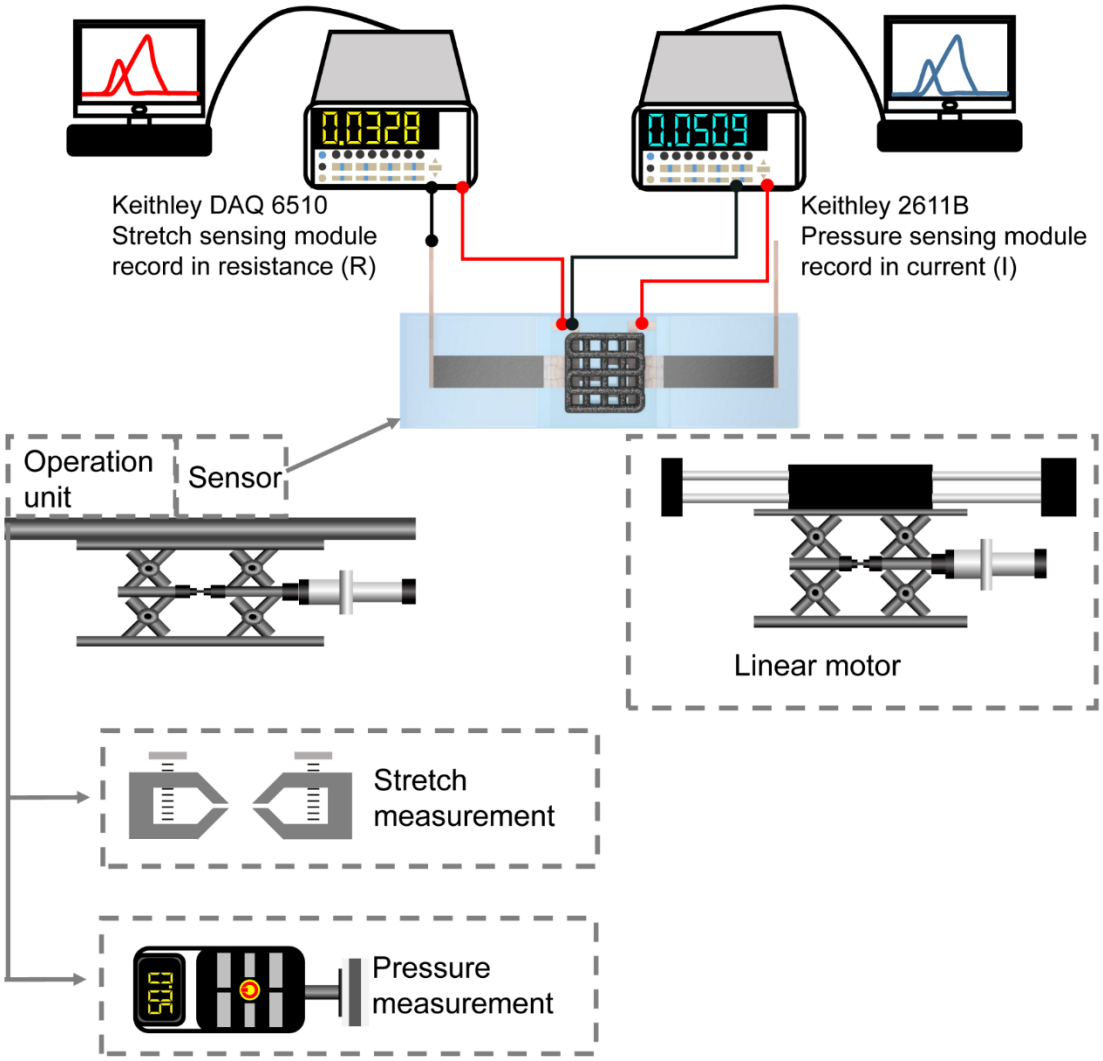

Figure 5.8 Schematic of the stretch/pressure sensing measurement setup. For pressure measurement, the pressure force is provided and measured by a computer-controlled linear motor and a digital force gauge, respectively. The current is recorded using a LabVIEW-controlled digital source meter (Keithley 2611B). For stretch measurement, the strain is provided by the linear motor. The resistance is recorded using a source meter (Keithley DAQ 6510).

5.4.1 Optimization of the sensing performance of stretch sensing module

We first optimized the preparation conditions of stretch sensing module, including the effect of different concentrations of CNTs and Ag nanoflakes (Figures 5.9A, 5.9B, and 5.9C), and the effect of pre-stretch treatment (Figure 5.9D).

For the stretch sensing module prepared with only CNTs, the sensing range and GF are increased with increased CNTs concentration; however, an excess of CNTs concentration (> 1 wt%) didn't show an obvious improvement in sensing performance. And the relative resistive change of the stretch sensing module prepared with only CNTs is still very low (Figure 5.9A). The stretch sensing module prepared only with highly conductive 2D Ag nanoflakes displayed a high GF, but a very small sensing range of 10%, which was caused by the easily fractured brittle Ag nanoflakes film under stretching. According to some studies,[173–175] The synergistic use of 2D and 1D conductive materials can form 1D-2D hybrid conductive networks with both high sensitivity and broad sensing range. In this case, the brittle and highly conductive 2D Ag nanoflakes film cracked under stretching, resulting in a high resistance variation, while the high aspect ratio of 1D CNTs conductive networks maintained the conductive pathway even under large stretching. (Figure 5.9B). Furthermore, Figure 5.9C investigated the sensing performance of the sensors prepared with different weight ratios of CNTs-Ag, where the sensors prepared with CNTs $_{(1)}$-Ag $_{(2)}$ exhibited higher GF. Besides the preparation of 1D-2D conductive network, the formation of anisotropic wrinkle/crumple structure through pre-stretch treatment has also been

proven to improve the sensing performance.[176–178] As shown in Figure 5.9D, compared to the sensor without pre-stretch treatment, the sensor with pre-stretch treatment exhibits higher sensitivity and a broader sensing range.

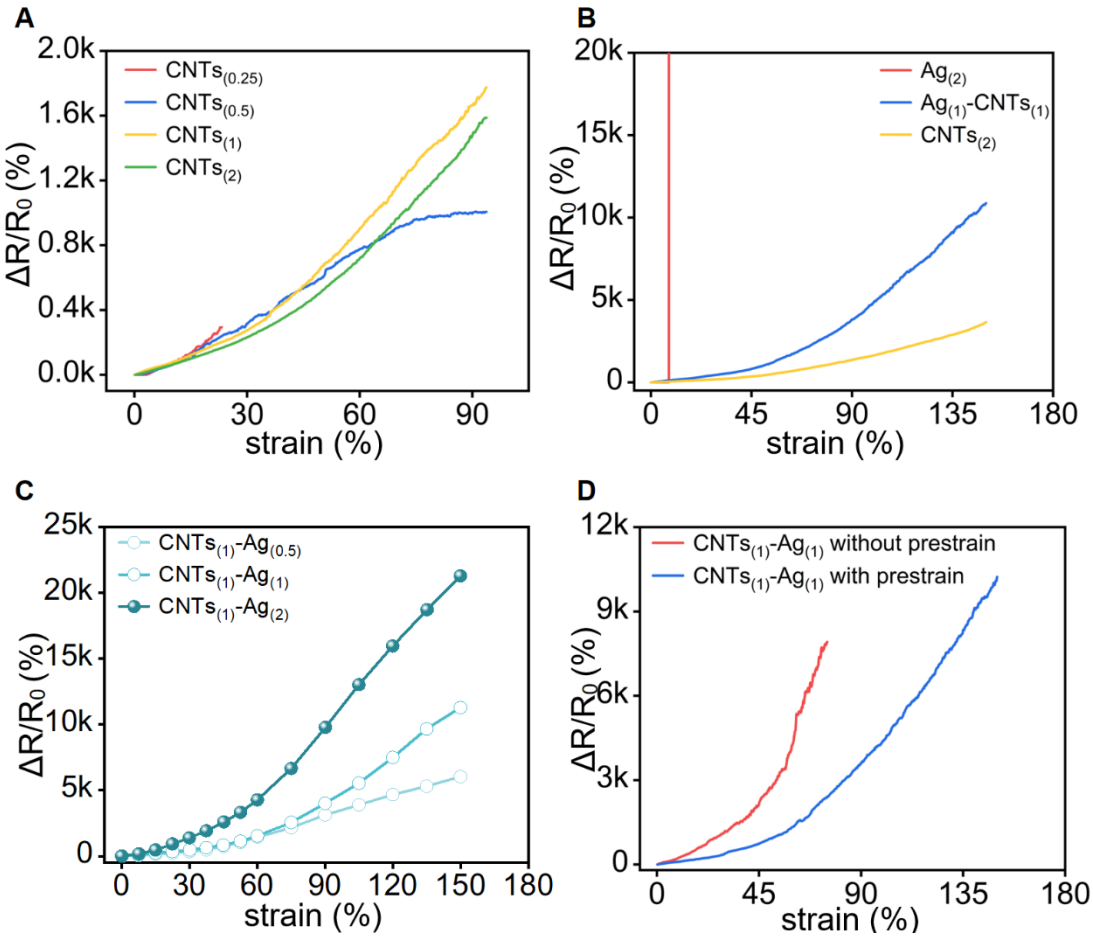

Figure 5.9 (A) Relative resistance change as a function of applied strain curves for stretch sensing module (A) consists of only CNTs with different concentrations: CNTs $_{(0.25)}$, CNTs $_{(0.5)}$, CNTs $_{(1)}$, and CNTs $_{(2)}$. (B) consists of different CNTs/Ag ratios: Ag $_{(2)}$, CNTs $_{(1)}$-Ag $_{(1)}$, and CNTs $_{(2)}$. (C) consists of different CNTs/Ag ratios: CNTs $_{(1)}$-Ag $_{(0.5)}$, CNTs $_{(1)}$-Ag $_{(1)}$ and CNTs $_{(1)}$-Ag $_{(2)}$. (D) consists of (CNTs $_{(1)}$-Ag $_{(1)}$) fabricated with and without prestrain treatment.

5.4.2 Optimization of the sensing performance of pressure sensing module

Another important sensing module of the WMS is the pressure sensing module. To optimize the pressure sensing module, the effect of different concentrations of CNF on sensing performance was investigated, as shown in Figure 5.10. The pressure sensing module composed of 1 wt% CNFs has the highest sensitivity compared with 0.75 wt% and 1.25 wt%. This is because higher concentration of CNFs can create more conductive pathways under the same pressure. However, excessive CNFs result in lower resistance (higher I_0) in the original state, and a lower value of current variation under pressure.

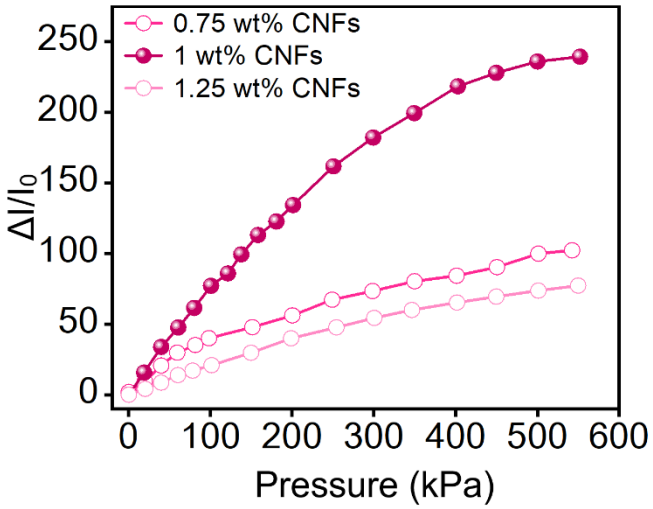

Figure 5.10 The relative current variation as a function of applied stress for pressure sensing module consists of different CNFs ratios and the detailed sensitivity of the optimized pressure sensing module.

5.5 Conclusion

In summary, we designed a wing-like structured WMS to precisely detect and differentiate multiple mechanical stimuli, including pressure, stretch, convex and concave bending. The wing-liked structure consists of a hierarchical in situ filling porous and wrinkled CNT-Ag nanoflakes hybrid film as the active layer of the pressure sensing module and stretch sensing module, respectively. The hierarchical in situ filling porous is fabricated by emulsion template methods and DIW printing techniques, and the wrinkled CNT-Ag nanoflakes hybrid film is prepared by pre-stretch treatment and coating of 1D CNTs 2DAg nanoflakes conductive network. The pressure sensing module is optimized by investigating the effect of different concentrations of CNF, and the stretch sensing module is optimized by studying the effect of different concentrations of CNTs and Ag nanoflakes, and the effect of pre-stretch treatment.

Chapter 6. Electromechanical performance of WMS and its applications

6.1 Introduction

In this chapter, the electromechanical sensing performance and various applications of WMS are comprehensively studied. After the optimization of the pressure and stretching sensing module, the pressure sensing module exhibits a high sensitivity of 0.61 kPa^{-1} and 0.25 kPa^{-1} in the range of 0 kPa to 300 kPa and 300 kPa to 500 kPa, and the stretching sensing modules achieves a high gauge factor (GF) of 40 and 140 in the strain ranges of 0–40% and 40–150%, respectively. Then the electromechanical sensing performance of pressure and stretching sensing module, including detection limit, response time, stability, and durability, were characterized. Furthermore, when tested for stretch, the change in resistance of the stretch sensing module will not be interfered by the external pressure from a perpendicular direction due to the high thickness and compressibility of the hierarchical porous sensing layer that withstands the entire pressure. Besides that, the sensor can detect and differentiate the convex and concave bending based on the positive and negative change of resistance in stretching sensing module, which is caused by conductive material breakage in convex bending and overlap in concave bending. Benefiting from the multiple mechanical stimulus detection and differentiation sensing capability, the WMS has demonstrated in accurate detection and differentiation of body kinesthesia, recognition of different types and sizes of objects by a WMS-integrated robotic gripper, locomotion monitoring and environment perception by a WMS-integrated crawling robot and human-machine interaction.

6.2 Methodology

6.2.1 Pressure and stretch sensing measurement

For pressure sensing test, the sensor is fixed to a digital force gauge using double-sided adhesive tape, and the head of the linear motor applies continuous or cyclic pressure to the sensor. The applied pressure is recorded by the digital force gauge, while the current was recorded using a LabVIEW-controlled digital source meter (Keithley 2611B). For stretch sensing test, one end of the sensor was clamped to the head of linear motor, which applied continuous or cyclic stretch to the sensor. The resistance was monitored by a source meter (Keithley DAQ 6510). The electrochemical analyzer (CHI660E) was used to measure the *I-V* curve under different pressures and stretches.

Calculation：

(1) Sensitivity

$S=\frac{\Delta I/I_0}{\Delta P}$

Where I_0 is the initial current when the sensor is without pressure loading, and ΔI is the current change of the sensor under a fixed pressure change (ΔP).

(2) Gauge factor (GF)

$GF=\frac{\Delta R/R_0}{\varepsilon}=\frac{\Delta R/R_0}{\Delta L/L_0}$

Where R_0 is the initial resistance of the sensor without stretching, and ΔR is the resistance change of the sensor under applied strain ε.

6.2.2 Reference sensor fabrication in body kinesthetic recognition

To demonstrate the sensing and differentiation capabilities of our WMS in body kinesthetic recognition, a common pressure sensor and a strain insensitive pressure sensor were fabricated and tested. The common pressure sensor was fabricated as follows: first, two pieces of conductive fabric electrode were transferred onto the two pieces of cut TPU film that serve as the top and bottom electrodes. The hierarchical in situ filling porous pressure sensing layer was then encapsulated between the top and bottom electrodes by double-sided adhesive tape. The sensor with the same wing-like structure, but without the wrinkled CNTs/Ag stretch sensing layer, was fabricated and tested as a reference sensor for stretch insensitive pressure sensor.

6.2.3 Fabrication of crawling robot

The structural components of a crawling robot are shown in Figure 6.13. The PET plat is cut by laser cutting machine and serves as the crawling robot’s elastic body, connecting its head and tail. The robot’s head is made of a PMMA box with a motor fixed inside that serves as the crawling robot’s driving motor. Teflon paper is pasted on the bottom of the robot's head to reduce friction when crawling forward. The robot’s tail is made of a bulk of PMMA with a fork structure pasted on the bottom to ensure that the robot has a strong forward thrust when crawling. The string connecting the motor to the tail tightened and loosened as the motor was rotated forward and

backward, allowing the crawling robot to be arched and recovered, driving the robot forward. The sensor is fixed to the body of the crawling robot to monitor crawling locomotion and perceive the environment during the crawling process.

6.3 Electromechanical characterization of stretch and pressure sensing module

After optimizing the preparation conditions of the stretch sensing module, the sensing performance, including detection limit, stability, and durability, was characterized. As shown in Figure 6.1A, the optimized stretch sensing module featured two regions: the GF value was 40 in the strain range of 0–40%, and the GF value was 140 in the strain range of 40–150%. The sensor has a low detection limitation of 0.1% along with fast response and recovery times of 36 ms and 74 ms, respectively (Figure 6.1B). Then the stability sensing performance of the sensor under different stretching conditions was tested (Figure 6.1C–E). As depicted in Figure 6.1C, the sensor displayed good linear current-voltage (*I-V*) characteristics in the interval from -3V to 3V, indicating a stable response under different static strains. The slope of the *I-V* curve gradually decreases with increased applied strain due to the increase in resistance caused by the breakdown of the conductive network. The relative resistance of sensor is measured under different cyclic strains (from 5% to 120%) at a stretch rate of 2 mm/s (Figure 6.1D). The signal response of the sensor under the same strain is consistent, which indicates stable output performance under cyclic strain at

different degrees of strain. Then cyclic tests at various frequencies (from 0.1 Hz to 1.5 Hz) under 20% strain were conducted, and no frequency dependence of the signal response was observed (Figure 6.1E). The relative resistive change was almost constant at different frequencies, which confirmed that the sensor can accurately recognize motion at different speeds. Afterwards, the hysteresis effect of the sensor is investigated in Figure 6.1F. At different strain rates of 1–4 mm/s, the stretching and releasing curves are nearly overlapped at 100% strain, indicating negligible hysteresis and good capabilities of elastic recovery. Long-term durability is an essential requirement for reliable use in practical applications. As shown in Figure 6.1G, the strain sensor exhibits excellent stability and reproducibility over 25000 cycles at a cyclic strain of 25% and a strain rate of 2 mm/s.

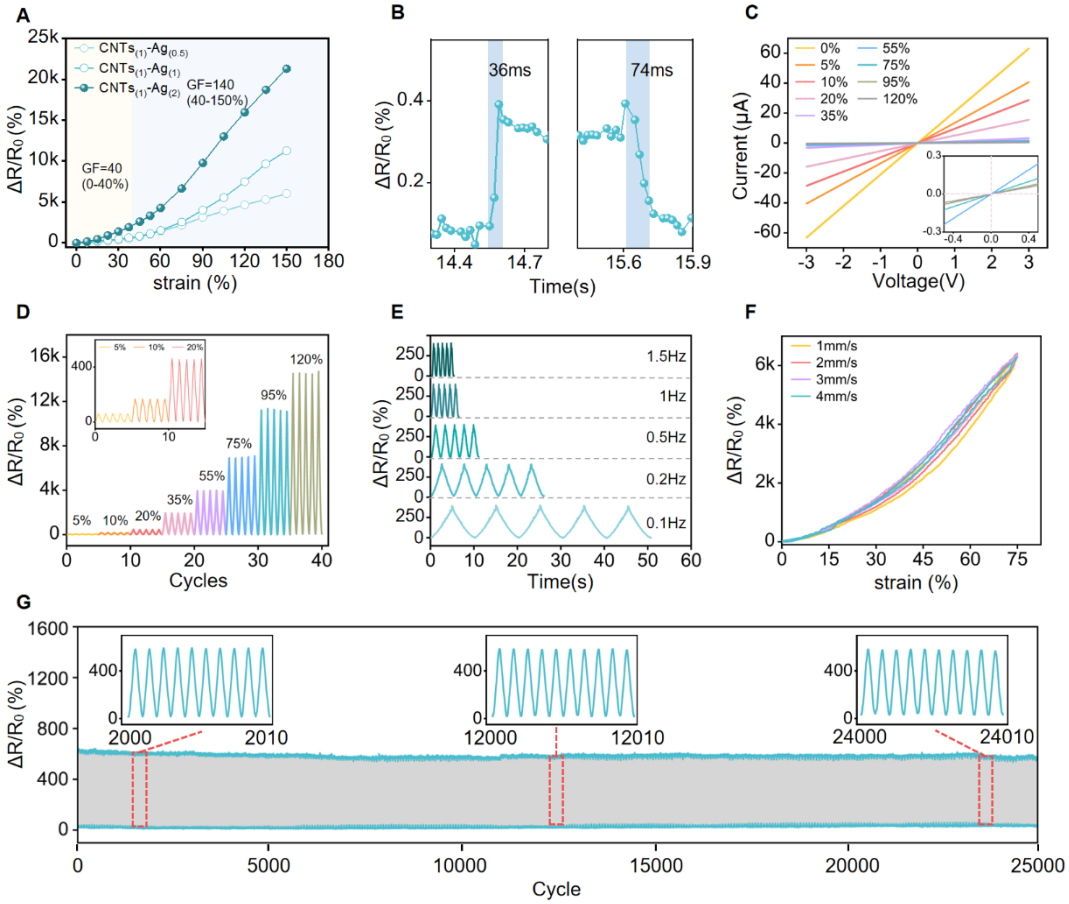

Figure 6.1 (A) Relative resistance change as a function of applied strain curves for stretch sensing module consists of different CNTs/Ag ratios: CNTs $_{(1)}$-Ag $_{(0.5)}$, CNTs $_{(1)}$-Ag $_{(1)}$ and CNTs $_{(1)}$-Ag $_{(2)}$, and the detailed gauge factor of the CNTs $_{(1)}$-Ag $_{(1)}$. (B) Response and recovery time of stretch sensing module under a strain of 0.1%. (C) Current-voltage curves of the stretch sensing module under different static strains (from 0% to 120%). (D) Multiple cycles test of relative resistance changes under different strains (from 5% to 120%). (E) Relative resistance changes at different frequencies (from 0.1 Hz to 1.5 Hz) under 20% strain. (F) Relative resistance change under one stretch/release cycle of 75% strain at different strain rates of 1, 2, 3 and 4 mm/s. (G) Relative resistance change during 25000 cycles under 25% strain (strain rate of 2 mm/s). The detailed relative resistance change is depicted in the inset figure.

Next, we characterized the sensing performance of the pressure sensing module, such as response time, stability, and durability. The optimized pressure sensor exhibits high sensitivity over a broad sensing range (Figure 6.2A). The pressure sensing module displays two sensing regions: sensitivity of 0.61 kPa^{-1} for pressure range of 0–300kPa, and the sensitivity of 0.25 kPa^{-1} for pressure range of 300–500 kPa. The pressure sensor exhibits a fast response and recovery time of 42 ms and 44 ms, respectively (Figure 6.2B), which is critical for accurate real-time monitoring. Meanwhile, the sensor also has a low detect limitation of 4.6 Pa (Figure 6.2C), allowing it to identify the subtle mechanical stimuli. The stability of sensing performance is an essential characteristic to be considered. Therefore, the stability of sensing performance under various pressing conditions is investigated in Figure 6.2D–F.

The *I-V* curves display good linear ohmic characteristics under different static pressures (0 kPa–400 kPa), demonstrating that the sensor has a stable response to the static pressure (Figure 6.2D). The slope of the *I-V* curve increases with increased pressure, indicating a decrease in resistance caused by creation of conductive pathways under pressure. Then, the sensing performance under dynamical loading/unloading cycles with different pressures (10 kPa–400 kPa) was investigated (Figure 6.2E). The sensor exhibits a higher current variation under a higher applied pressure, and the sensor maintains a constant current variation under the same pressure. In addition, the sensor also showed no frequency dependence at different frequency (0.1 Hz–1.5 Hz) cyclic tests under a pressure of 100 kPa (Figure 6.2F).

Furthermore, as shown in Figure 6.2G, the relative current variation response has the same pattern as the input pressure (triangular, sine, and rectangular), suggesting the high fidelity of the sensor to recognize pressure information accurately. The pressure sensing module presents good durability during 50000 loading/unloading cycles under 50 kPa pressure (Figure 6.2H). The current variation remains almost constant throughout the cycle, implying the high robustness of the sensor.

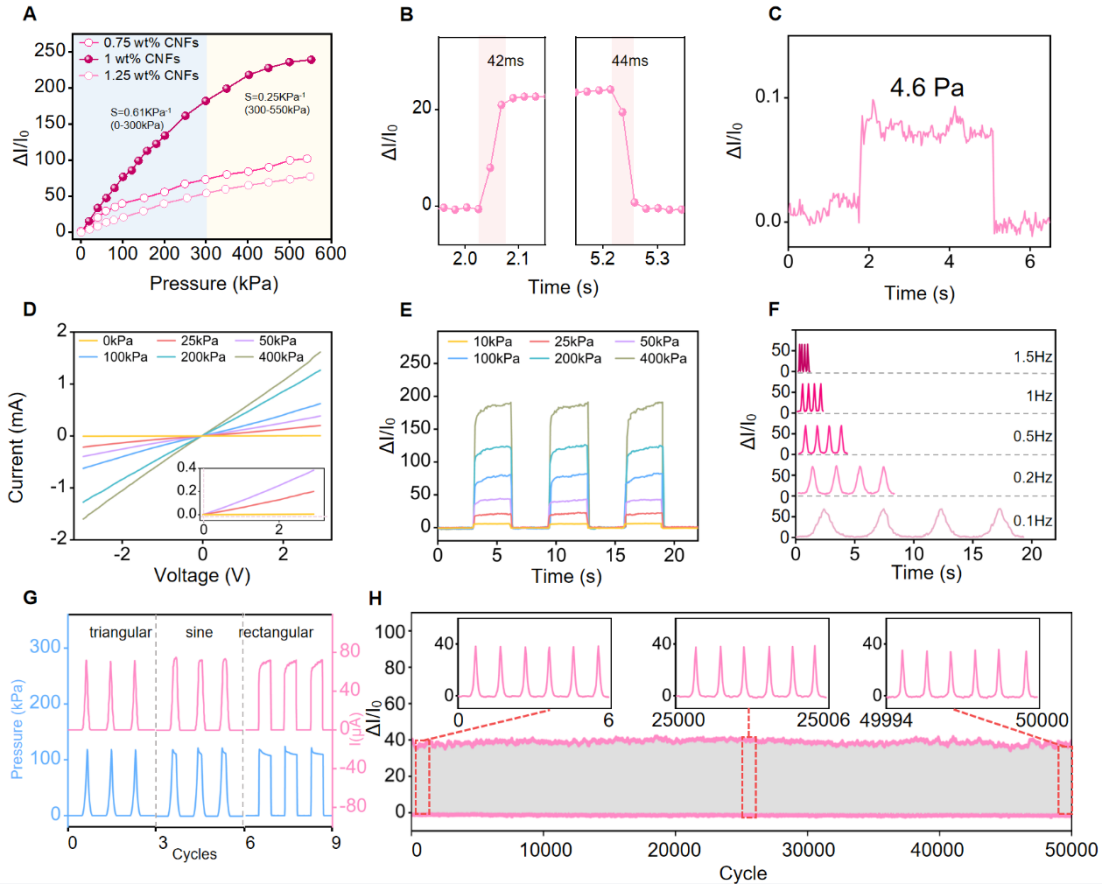

Figure 6.2 (A) The relative current variation as a function of applied stress for pressure sensing module consists of different CNFs ratios and the detailed sensitivity of the optimized pressure sensing module. (B) Response and recovery time of pressure sensing module under a pressure of 25 kPa. (C) Detection limit of the pressure sensing module. (D) *I-V* curves of the pressure sensing module under different pressures (from 0 kPa to 400 kPa). (E) Multiple loading/unloading cycles of relative current variation under different pressures (from 10 kPa to 400 kPa). (F) Relative current variation under 100 kPa at different frequencies (from 0.1 Hz to 1.5 Hz). (G) Relative current variation of sensor under different types of cyclic pressure. (H) Relative current variation over 50000 loading/unloading cycles under the pressure of 50 kPa. Figure inset depicting the detailed relative current variation.

6.4 Validation of the ability to detect and differentiate multiple mechanical stimuli

Despite some high-performance sensors having been developed, the majority of them are incapable of detecting and differentiating multiple mechanical stimuli, limiting their application in complex mechanical stimuli situations. Our designed wing-like structure enables the WMS to detect and differentiate multiple mechanical stimuli, including press, stretch, and convex and concave bending. To investigate this sensing capability, the resistance change of stretch sensing module and current variation of pressure sensing module were recoded simultaneously by two digital meters during different mechanical stimuli given by linear motor. Under only pressure and 0% lateral stretch, the current variation of pressure sensing module increases with increasing pressure, while the resistance changes of stretching module remain unchanged, as shown in Figure 6.3A, indicating the pressure only causes the response in the pressure sensing module and no interference with the stretch-sensing module. In addition, as shown in Figure 6.3B, the pressure sensing module also presents almost the same current variation under the same pressure at strains of 50% and 0%, while the response of the stretching sensing module maintains stability without being disturbed by the pressure. This pressure insensitive stretch sensing behavior in stretch sensing module is due to thickness of pressure module is higher than the stretched module, and high compressibility of hierarchical porous sensing layer bears the full pressure, preventing pressure on stretch sensing module. The finite-element simulations of strain distribution in Figure 6.3C and stress distribution in Figure 6.3D

further confirm that the deformation occurs only in the hierarchical in situ filling porous sensing layer, while the stretching module is not affected by the pressure.

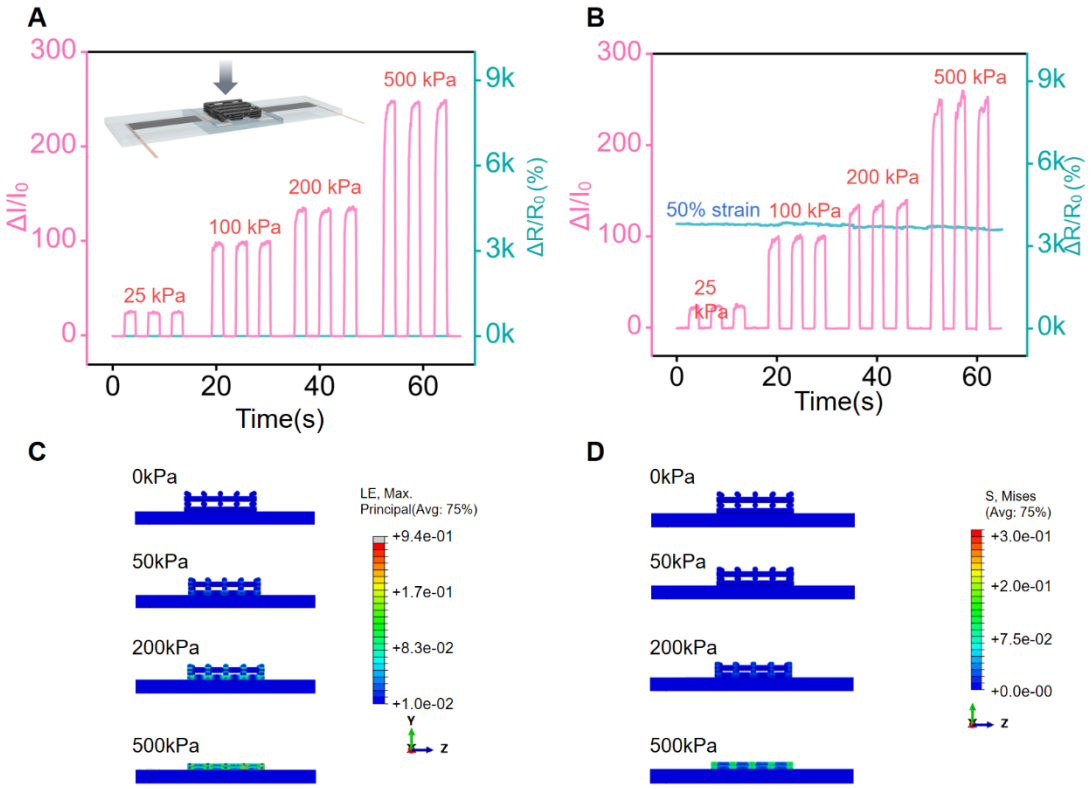

Figure 6.3 (A) Relative resistance changes of stretch sensing module and current variation of pressure sensing module under repeat pressure from 25 kPa to 500 kPa under (A) 0% strain and (B) 50% strain. Finite-element simulation of stress distribution of the sensor from the side view. Side view of finite-element simulation of (C) stress and (D) strain distribution of the sensor under pressure from 0 kPa to 500 kPa.

When the sensor is laterally stretched at 0 kPa pressure (Figure 6.4A), the resistance change of stretching module increases significantly, and the current

variation of pressure sensing module remains almost constant. Furthermore, the stretch sensing module also presents almost the same resistance change at pressures of 0 kPa and 40 kPa, while the current variation keeps constant under the static pressure of 0 kPa and 40 kPa (Figure 6.4B). The reason for stretch insensitive pressure sensing feature in pressure module is that the entire strain effect is carried by Ecoflex substrate with a lower Young's modulus of 125 kPa in both wings,[179,180] without affecting the pressure module with a larger Young's modulus of 2 MPa.[181,182] From the finite-element simulations of strain distribution in Figure 6.4C and stress distribution in Figure 6.4D, the 0%–150% stretching deformation was observed only in both wings structure, while negligible strain occurred in pressure sensing module. The simulation results (Figure 6.3, 6.4, 6.5 and 6.6) are consistent with experiment results, indicating that the pressure sensing module will not be disturbed during stretching.

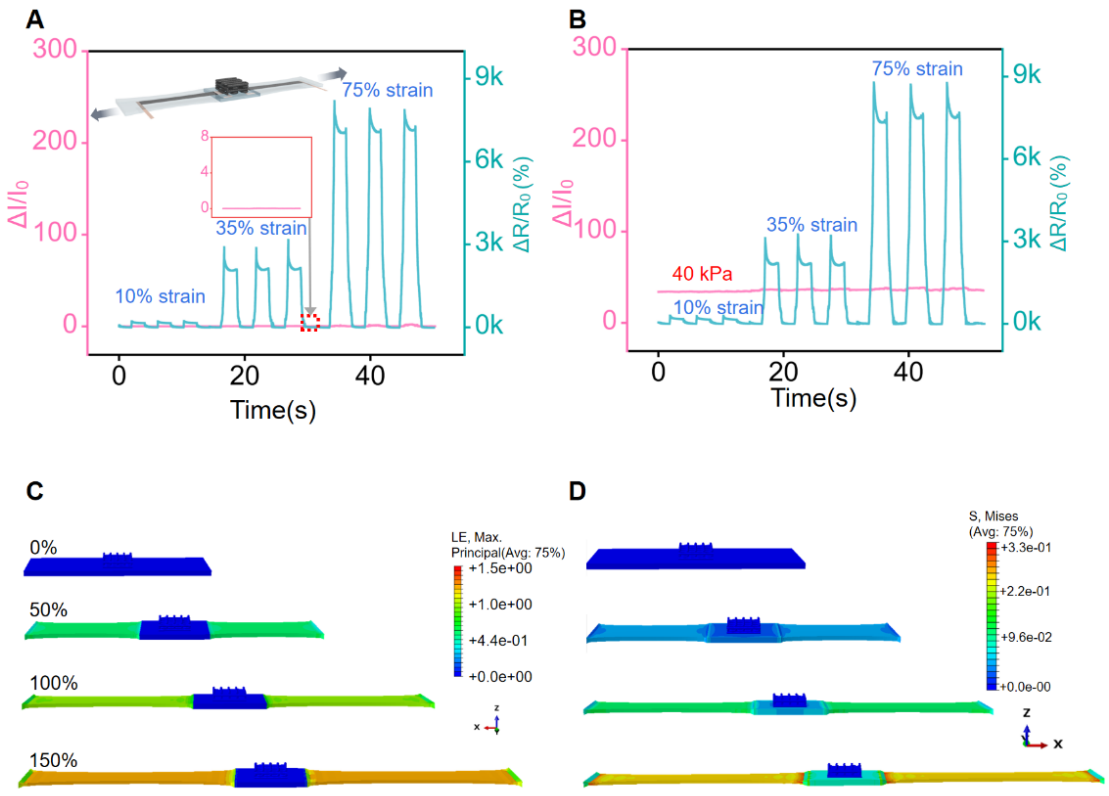

Figure 6.4 (A) Relative resistance changes of stretch sensing module and current variation of pressure sensing module under repeat pressure from 25 kPa to 500 kPa under (A) 0 kPa and (B) 40 kPa pressure. Finite-element simulation of stress distribution of the sensor from the side view. Side view of the finite-element simulation of (C) stress and (D) strain distribution of the sensor under stretch from 0% to 150%.

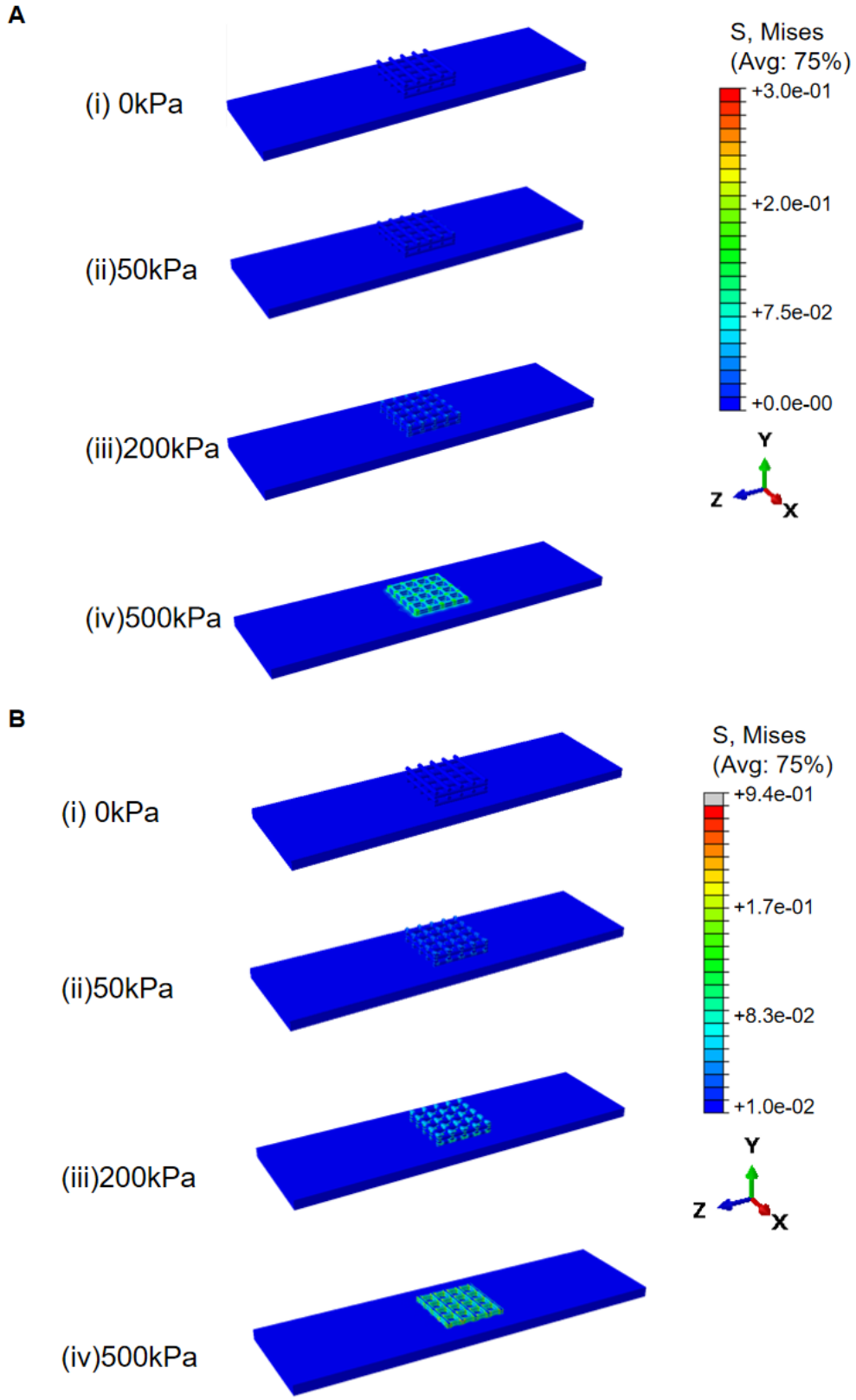

Figure 6.5 Finite-element simulation of stress distribution of the sensor from the oblique view. Oblique view of finite-element simulation of (A) stress and (B) strain distribution of the sensor under pressure from 0 kPa to 500 kPa.

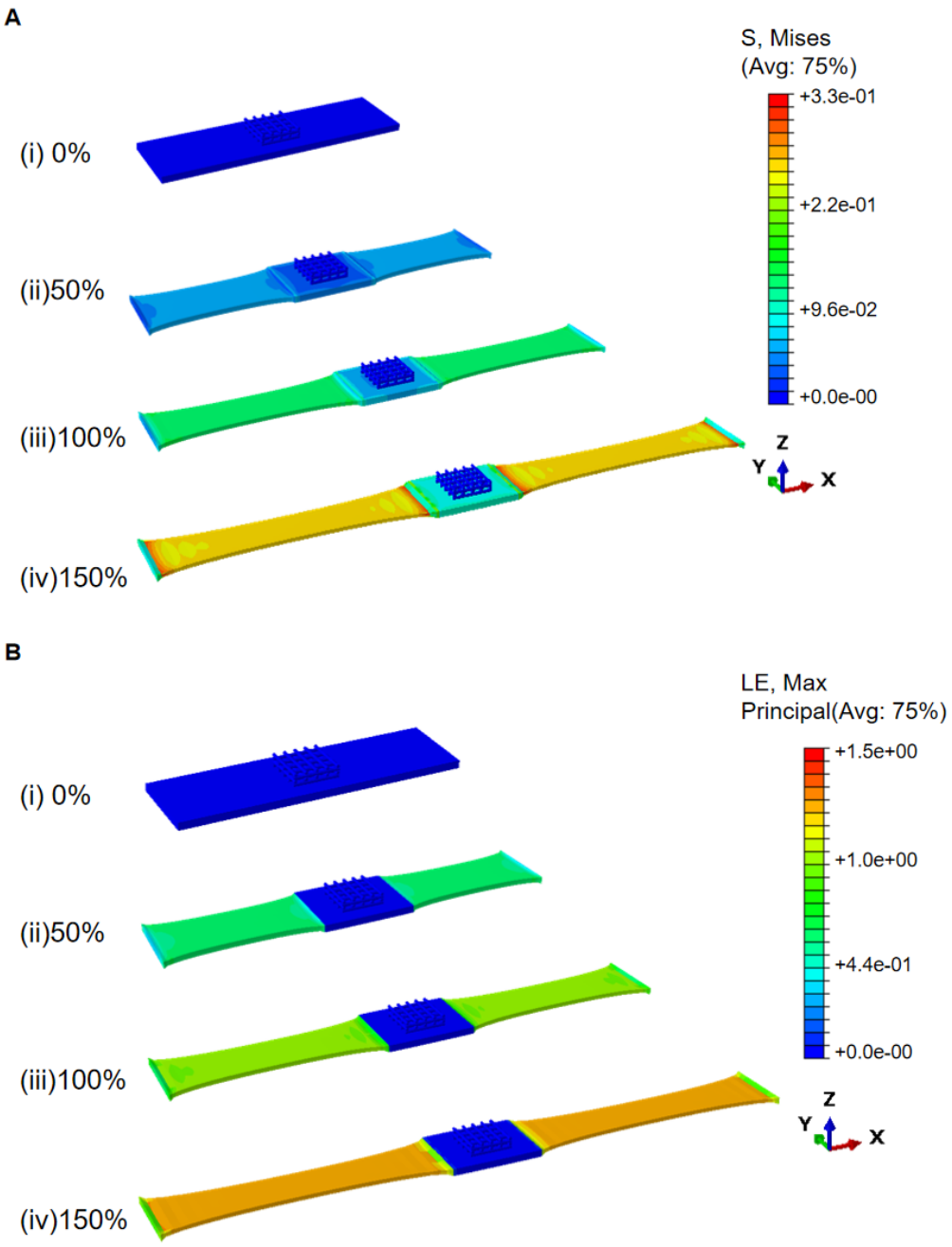

Figure 6.6 Finite-element simulation of stress distribution of the sensor from the oblique view. Oblique view of the finite-element simulation of (A) stress and (B) strain distribution of the sensor under stretching from 0% to 150%.

Besides pressure and stretching, convex and concave bending are also common motions in practical applications, especially in motion detection for humans and robots. To measure the bending sensing, the sensor was pasted on a PET substrate while the two ends of PET were clamped on the linear motor, as shown in Figure 6.7.

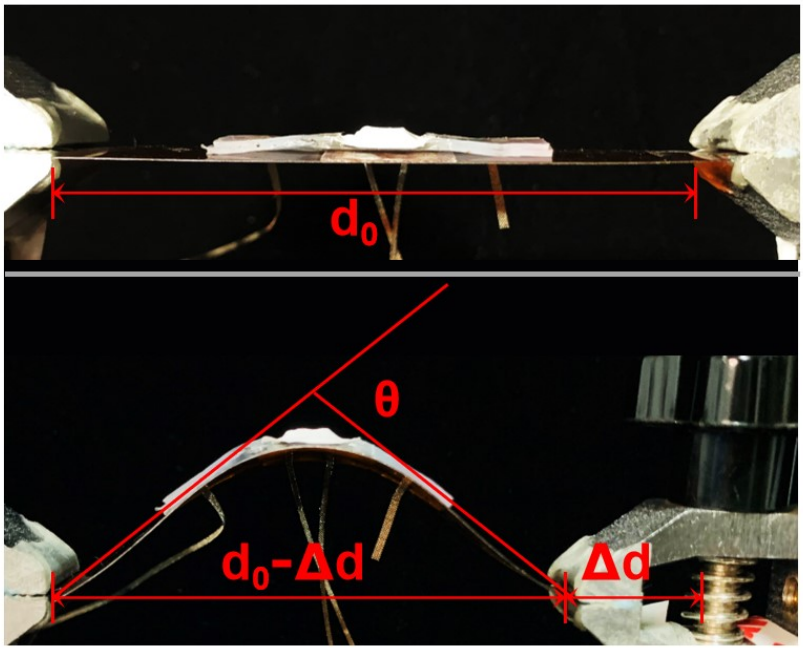

Δd(cm)	θ
0.15	22°
0.3	32°
0.6	45°
1	60°
1.5	72°

Figure 6.7 Schematic illustration of the bending measurement set up. The sensor is fixed on a PET substrate, while the two ends of PET are fixed on the linear motor. The initial length of the PET substrate was defined as d_0, the bending moving distance was defined as Δd. The bending angle θ was defined as the external angle of the two ends.

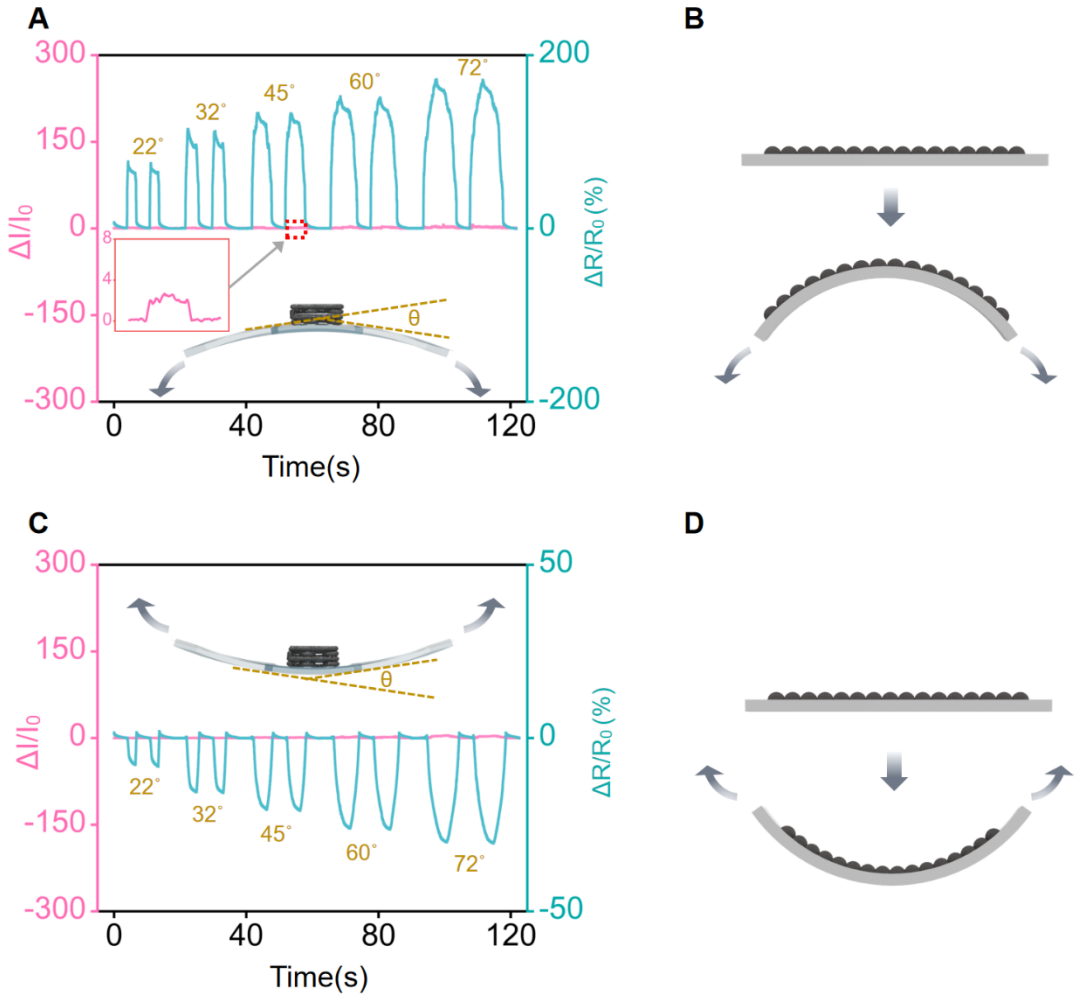

Figure 6.8 Relative resistance changes of stretch sensing module and current variation of pressure sensing module under (A) convex bending from 22° to 72° and (B) schematic illustration. Sensing signal under repeat (C) concave bending from 22° to 72° and (D) schematic illustration.

The bending of the sensor attached PET substrate was induced by adjusting the movement of the linear motor. The bending angle is defined as the external angle of the two ends shown in Figure 6.8. For convex bending shown in Figure 6.8A, the resistance increases with the increase in bending angle, while the current variation of pressure sensing module increases slightly due to the tighter contact between the

electrode and sensing layer during convex bending. As illustrated in Figure 6.8B and according to the interpretation of some research,[183–185] the increase in resistance is due to the separation and breakage of CNTs-Ag hybrid film, which hinders the electron transfer between conductive nanoparticles, resulting in an increase in resistance. Here, although the resistance changes exhibit the same increasing trend under stretching and convex bending, there is a large amplitude difference in resistance change between the stretch and the convex bending, coupled with the difference in the current change, which can differentiate between the stretching and the convex bending. Contrary to convex bending, the resistance decreased as the concave bending angle increased, as shown in Figure 6.8C. As schematically illustrated in Figure 6.8D, concave bending leads to overlap and contacts between conductive nanoparticles, which provide more conductive pathways and result in lower resistance.

6.5 Applications

6.5.1 Application of WMS in accurately body kinesthetic recognition

There are many flexible sensors that have been developed and demonstrated in body kinesthetic recognition; however, they cannot discriminate accurately among different mechanical stimuli because their sensors present the same electric signal tendency under different mechanical stimuli.[8,70,186–188] As shown in Figure 6.9A, Figure 6.9B and 6.9C, in order to detect multiple mechanical stimuli to finger joints,

the WMS is attached to the finger, where the pressure sensing module was fixed in the position of the middle knuckles. The resistance changes increased as the finger bent from a small angle (Figure 6.9C (iii)) to a large angle (Figure 6.9C (iv)), while the current variation exhibits a negligible change. When gently touching the knuckles in finger straightening state (Figure 6.9C(ii)) and finger flexion state (Figure 6.9C(v)), the current change increased significantly, while the resistance change in stretching sensing module remained constant. As a result, the actions of bending the finger, touching the knuckle, and touching the knuckle while bending are identified and differentiated. Here, a common pressure sensor and a stretch insensitive pressure sensor are fabricated and tested to further compare and demonstrate the sensing and differentiating capabilities of our WMS. The common pressure sensor exhibits the same tendency of current change during finger flexion and knuckle touch, making it impossible to differentiate between these two actions. The stretch insensitive sensor can accurately identify the knuckle touch regardless of the finger bending, but it fails to detect the bending finger.

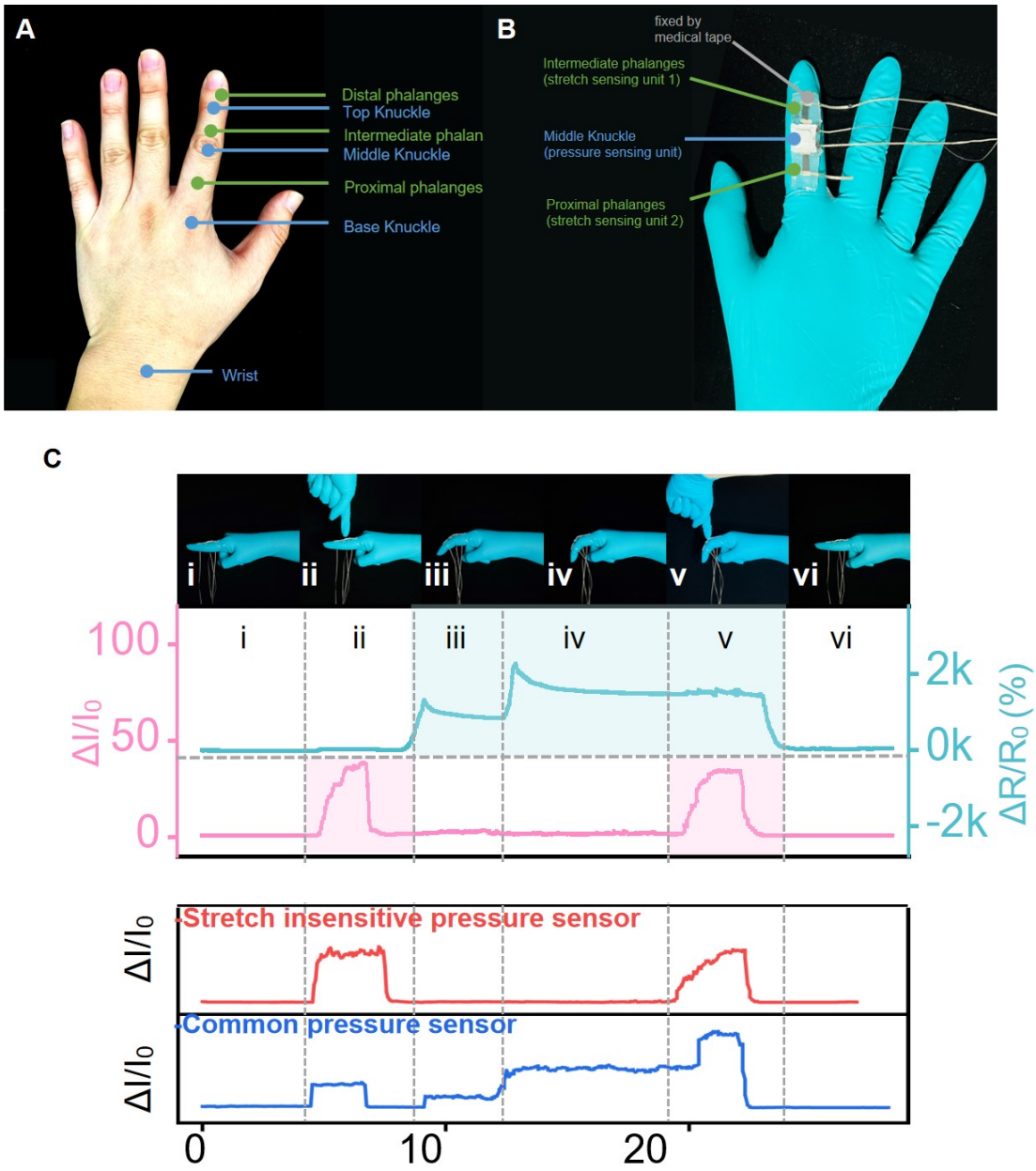

Figure 6.9 (A) Schematic structure of the hand. (B) Photograph of the sensor setup for detecting multiple mechanical stimuli to finger joints. (C) Perception and discrimination of multiple mechanical stimuli on finger joints, including finger flexing and gentle touch on the knuckles.

The processing of clenching and punching the fist is perceived and differentiated by attaching the WMS to the finger, where the pressure sensing module is fixed in the position of proximal phalanges, as shown in Figure 6.10A and Figure 6.10B. When clenching fist, the stretched stretch sensing module triggers an increase in resistance change (Figure 6.10B (iii, iv)), while the current variation remains stable. Then the current variation increases significantly when gently touching the finger (Figure 6.10B (ii)) and punching (Figure 6.10B (v)), while the resistance change in the stretching sensing module remains constant.

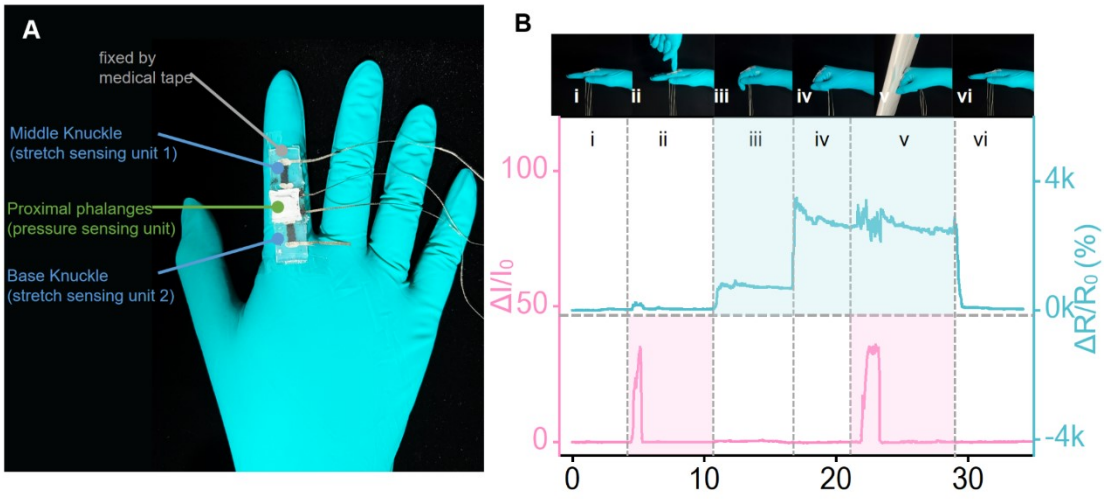

Figure 6.10 (A) Photograph of the sensor setup for detect multiple mechanical stimuli for the process of clenching fist and punching. (B) Perception and discrimination of multiple mechanical stimuli on the finger, including clenching and punching the fist.

During knee flexion, the resistance increased, while the current variation did not interfere with the knee bending (Figure 6.11A (iii, iv)). The resistance change is larger with knee flexion than with finger flexion and fist clenching due to a larger degree of stretch deformation in knee flexion. Then pressing the knee in the straightened and

bent leg states (Figure 6.11A (ii, v)) induces an increase in current variation while the resistance change remains constant.

Different from the kinesthetic tests described above, where the joint bending is measured by stretching of stretch sensing module, while the wrist bending is measured by bending of stretch sensing module, which is aimed to differentiate the bending of the wrist backwards and forwards. To measure the multiple mechanical stimuli on the wrist, the PET sheet pasted with the sensor is fixed to the wrist rather than directly attaching the sensor to the wrist. Bending the wrist backwards causes the stretch sensing module to bend concavely, resulting in a decrease in resistance change (Figure 6.11B (ii, iii)). Oppositely, the forward bending of the wrist results in a convex bending, which increases the resistance change. Furthermore, the gentle touches on the straight (Figure 6.11B (i)), bending backward (Figure 6.11B (iii)), and bending forward (Figure 6.11B (vi)) wrists resulted in an increase in current variation without affecting the resistance change signal.

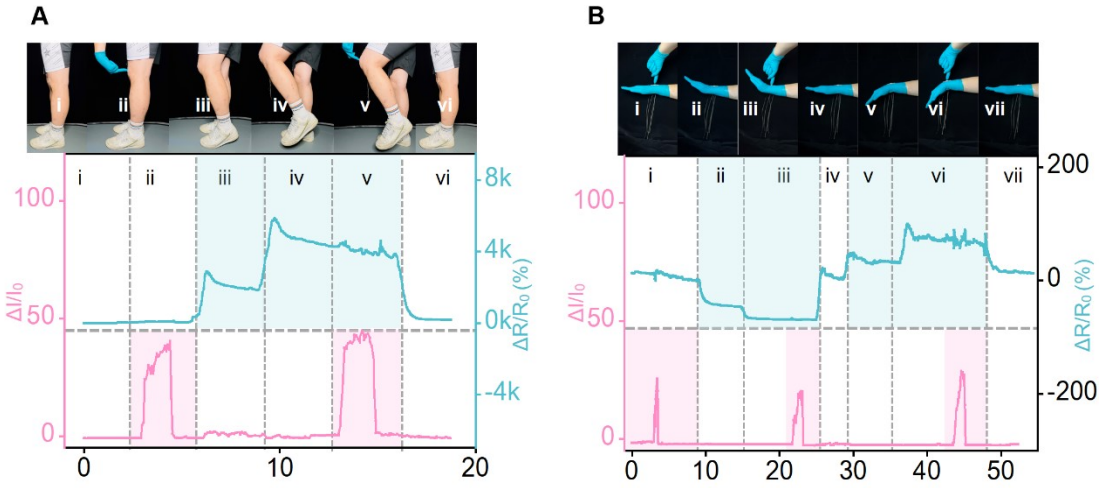

Figure 6.11 (A) Perception and discrimination of multiple mechanical stimuli on knee joint, including bending and touching the knee joint. (B) Perception and discrimination of multiple mechanical stimuli of wrist, including bending the wrist backward, forward, and touching the wrist.

6.5.2 Application of robotic gripper with integrated WMS in objects recognition

Although there are some reports of robotic hands with an integrated sensor that can identify objects through either material types, size or roughness, they cannot identify both size and material at the same time.[189–192] Benefiting from the multifunctional sensing capability of the sensor, we integrate the sensor on the inner side of the robotic gripper (Figure 6.12A) to identify and differentiate different material types and sizes simultaneously. The object recognition mechanism is interpreted in Figure 6.12B. The concave bending of the stretch sensing module identifies the size of the object, while the pressure applied by the object to the pressure sensing module identifies the material type of the object. As depicted in

Figure 6.12C, when the robotic gripper grips an object, the concave bending degree of the robotic gripper increases as the object size increases, resulting in a larger decrease in resistance change. Meanwhile, the object exerts pressure on the robotic gripper, and the harder material (hardness: glass > rubber > expanded polyethylene (EPE) foam > Ecoflex) provides a large pressure to the sensor, leading to a larger increase of current variation. As a result, the robotic gripper with the integrated WMS demonstrated the feasibility of simultaneously identifying different materials and sizes.

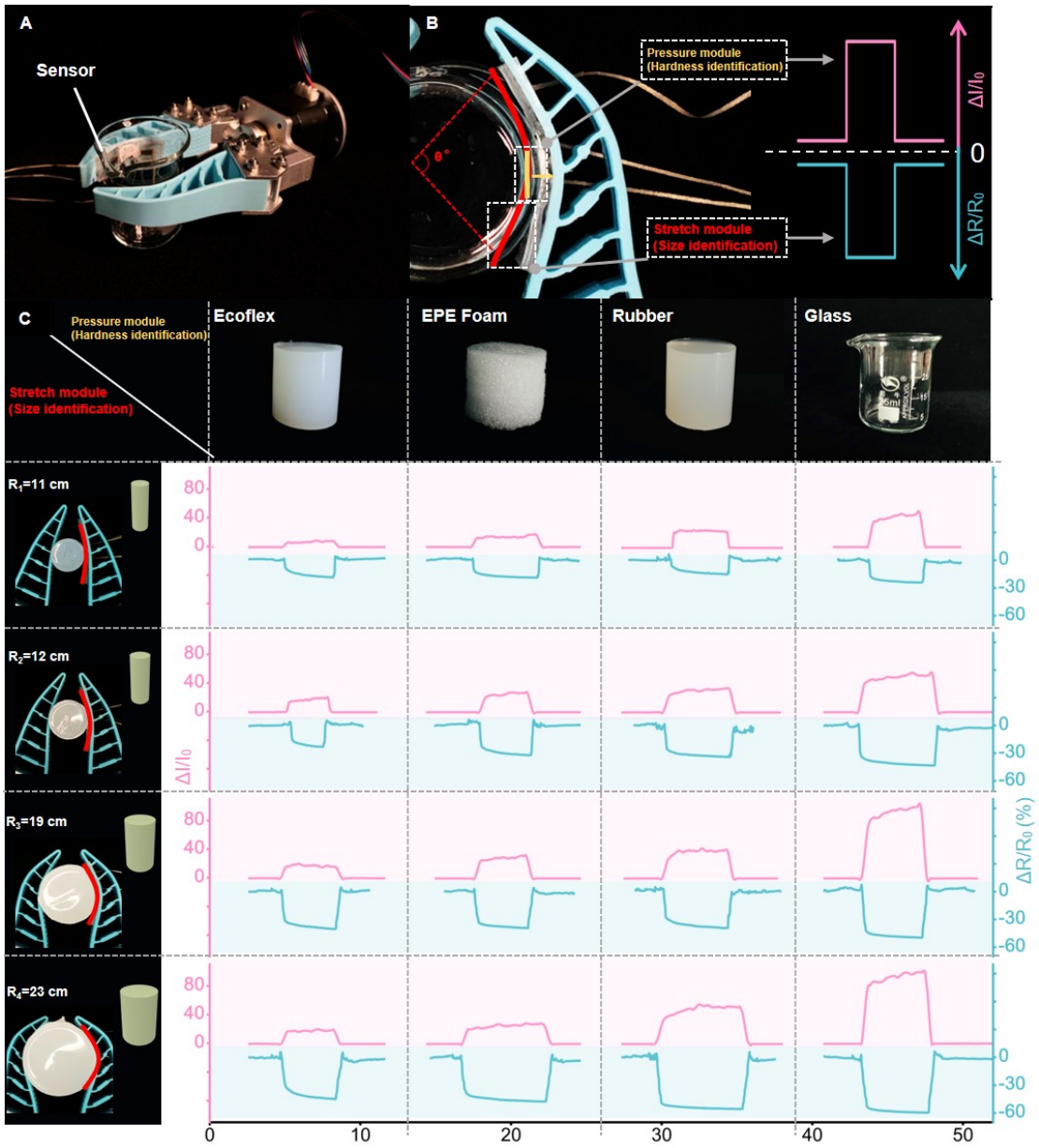

Figure 6.12 (A) Photograph of the robotic gripper with integrated WMS. (B) Object recognition mechanism of the WMS. (C) The current variation and resistance change for gripping objects with different materials (Ecoflex, EPE foam, rubber, and glass) and different sizes (22 cm, 25 cm, 38 cm, and 46 cm).

6.5.3 Demonstration of WMS for a crawling robot in locomotion monitoring and environment perception

Despite many progresses and innovations made in the structure design and actuation methods of soft robots, it is necessary to integrate the sensor system into the soft robot system to realize a conscious robot capable of motion monitoring and environmental perception.[193–195] Here, we demonstrate a WMS-integrated inchworm-type crawling robot that can perceive complex environments while crawling. The structure of the crawling robot and fabrication details are presented in Figure 6.13 and the experiment section.

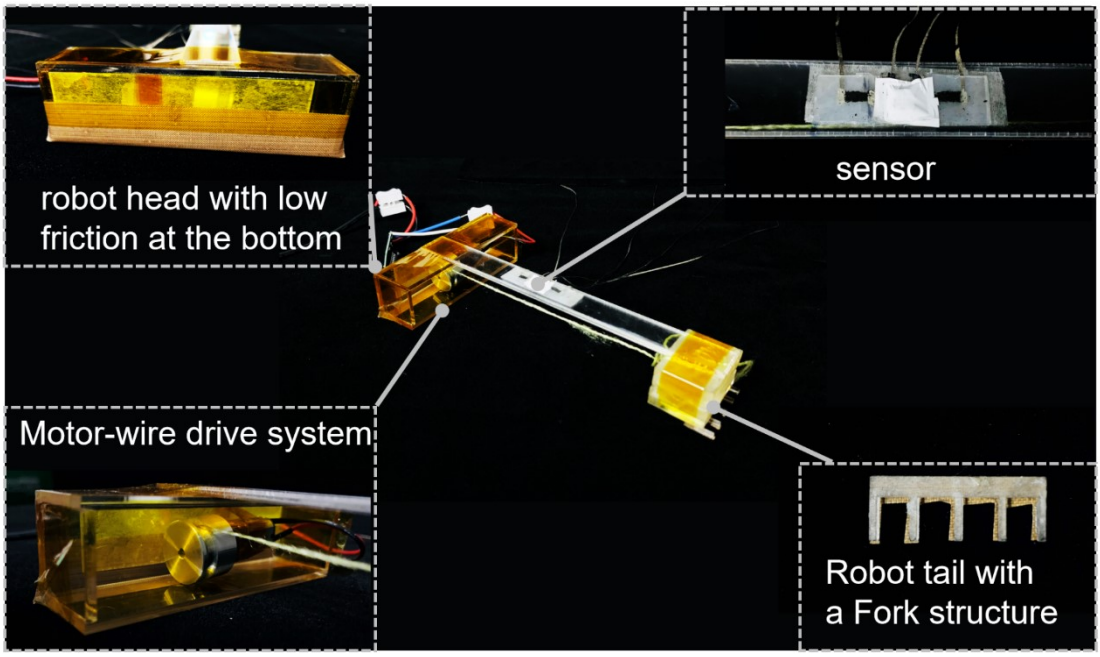

Figure 6.13 Schematic structure of the crawling robot.

The crawling robot's forward motion is driven by the motor pulling and releasing the string connected to the motor and the tail, causing the robot body to arch and restore. The sensor is fixed on the body of the crawling robot to perceive the

environment when the robot crawls. As shown in Figures 6.14A and 6.14B, the scenes of the robot crawling in an unknown channel and on an unknown surface are simulated and constructed. The bending degree during robot crawling can be monitored by measuring the resistance change; a larger bending degree results in a larger increase in resistance change, as depicted in Figure 6.14A (i) and (ii).

Then the robot crawls in a gradually narrowing tunnel, as shown in Figure 6.14A (iii) and (iv). In the phase of Fig. 6.14A (iii), the robot's body gently touches the relatively high ceiling of the tunnel, resulting in a slight increase in the current signal. As the crawling robot continues to crawl forward in the gradually narrowed channel (Figure 6.14A (iv)), the robot collides severely on the relatively low ceiling, causing a larger current signal, and the narrow tunnel limits the bending degree of robot, resulting in a lower resistance change compared with Figure 6.14A (iii). Thus, the crawling robot can perceive that it is crawling through a gradually narrowing channel based on the output signal of current variation and resistance change.

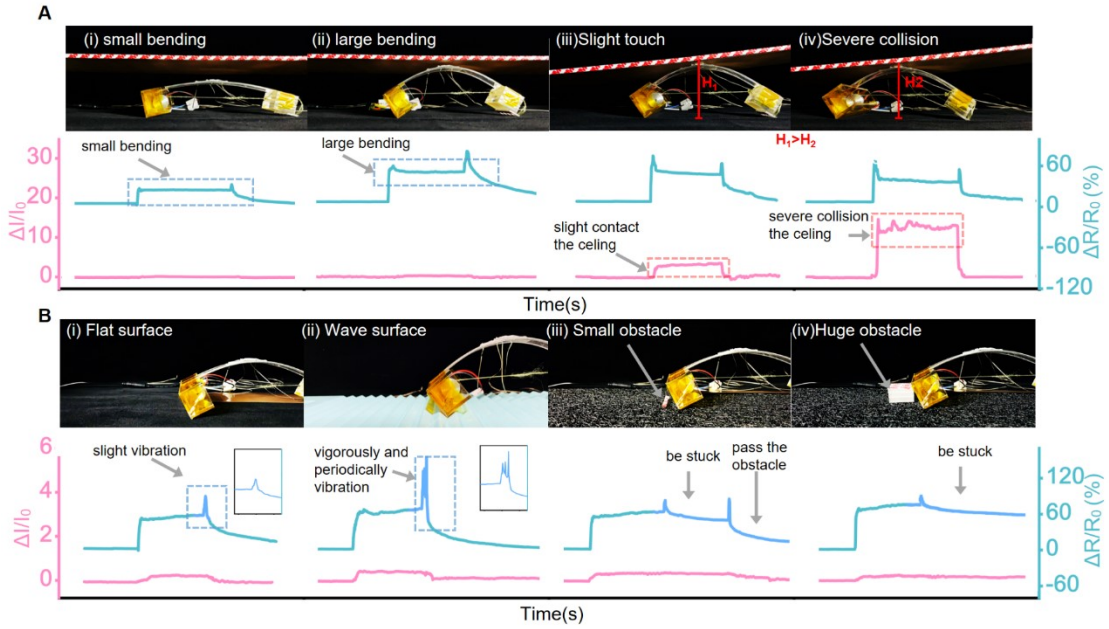

Figure 6.14 (A) The sensing signal of the WMS-integrated crawling robot during (i, ii) crawling with different bending degrees and (iii, iv) crawling in a gradually narrowing tunnel. (B) The sensing signal of the WMS-integrated crawling robot during crawling on the surface with (i) a flat structure, (ii) a waved structure, (iii) a small obstacle, and (iv) a huge obstacle.

The crawling robot can also perceive the crawling surface condition, as depicted in figure 6.14B. As the crawling robot crawls on a flat surface (Figure 6.14B (i) and inset), a small peak of resistance change is detected, which is mainly caused by vibrations generated when the robotic body suddenly straightens from the bent state as the robot moves forward. As the robot crawls on the wave surface, waveform peaks with a higher intensity of resistance change are generated, as shown in Figure 6.14B (ii) and inset. Each peak in the waveform signal is caused by small vibrations when the crawling robot crosses each small bump in the wave structure. In the process of crossing the small obstacle (Figure 6.14B (iii) and Figure 6.15), the robot's head is

first stuck by the small obstacle for a few seconds (Figure 6.15 (iii)), and the robot's body, with less bending, exhibits a slight reduction in resistance change. After the robot crosses the small obstacle (Figure 6.15(iv)), the robot's body goes from a bending state to straightening, resulting in the resistance change returning to the initial state. As the robot moves forward until it is blocked by a huge obstacle (Figure 6.14B (iv) and Figure 6.16), its body maintains a bent state, causing the resistance to change slightly initially (Figure 6.16 (ii)) and then remain constant (Figure 6.16 (iii)).

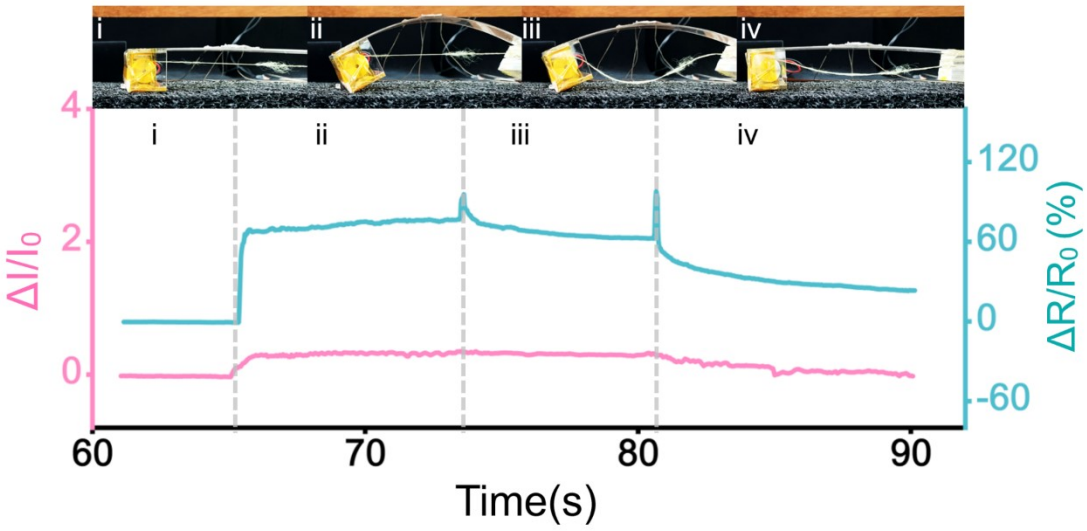

Figure 6.15 The detailed process of output sensing signal of the crawling robot during its pass through a small obstacle.

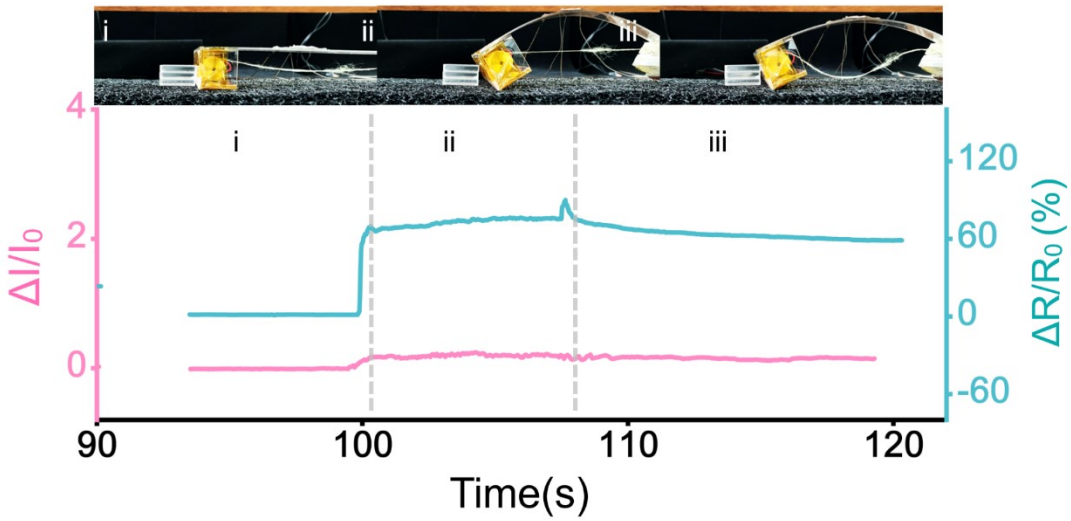

Figure 6.16 The detailed process of output sensing signal of the crawling robot during its pass through a large obstacle.

6.5.4 Demonstration of WMS for human-machine interaction

Human-machine interfaces, which interact physical information from the human body with virtual information in machine, have received increasing attention and are being applied in a lot of fields. However, most current research on e-skin human-machine interaction systems requires a sensor array integrated by several single-function sensing units to implement multiple human-machine command control.[160,196] Benefiting from the multifunctional and mutually independent sensing ability, multiple control commands in the human-machine interaction system can be simply realized by the WMS. In the human-machine interactive system, as shown in Figure 6.17A, the sensor is attached to the finger, wherein the pressure sensing module is fixed at the location of proximal phalanges, the stretch sensing module 1 is located at middle knuckle, and the stretch sensing module 2 is located at base knuckle.

A microprogrammed control unit (MCU) was used to process and code the electrical signals from the WMS. After data processing and comparison with thresholds, the different mechanical stimuli information received by the finger is translated into specific commands in the virtual game program, as depicted in flow chart of Figure 6.17B.

In the human-machine computer game shown in Figure 6.17C, the output signal generated by bending the finger at the middle knuckle controls the right turn; the output signal generated by bending the finger at the bottom knuckle controls the left turn; and the output signal generated by pressing the proximal phalanx controls the shooting. When a single specific finger action is executed, no other command is accidentally triggered, indicating there is no crosstalk among these three-sensing units. In addition, the combination command can be implemented by executing two finger actions simultaneously, such as bending at middle knuckle and pressing to control the turn right while shooting or bending at the base knuckle and pressing to control the turn left while shooting.

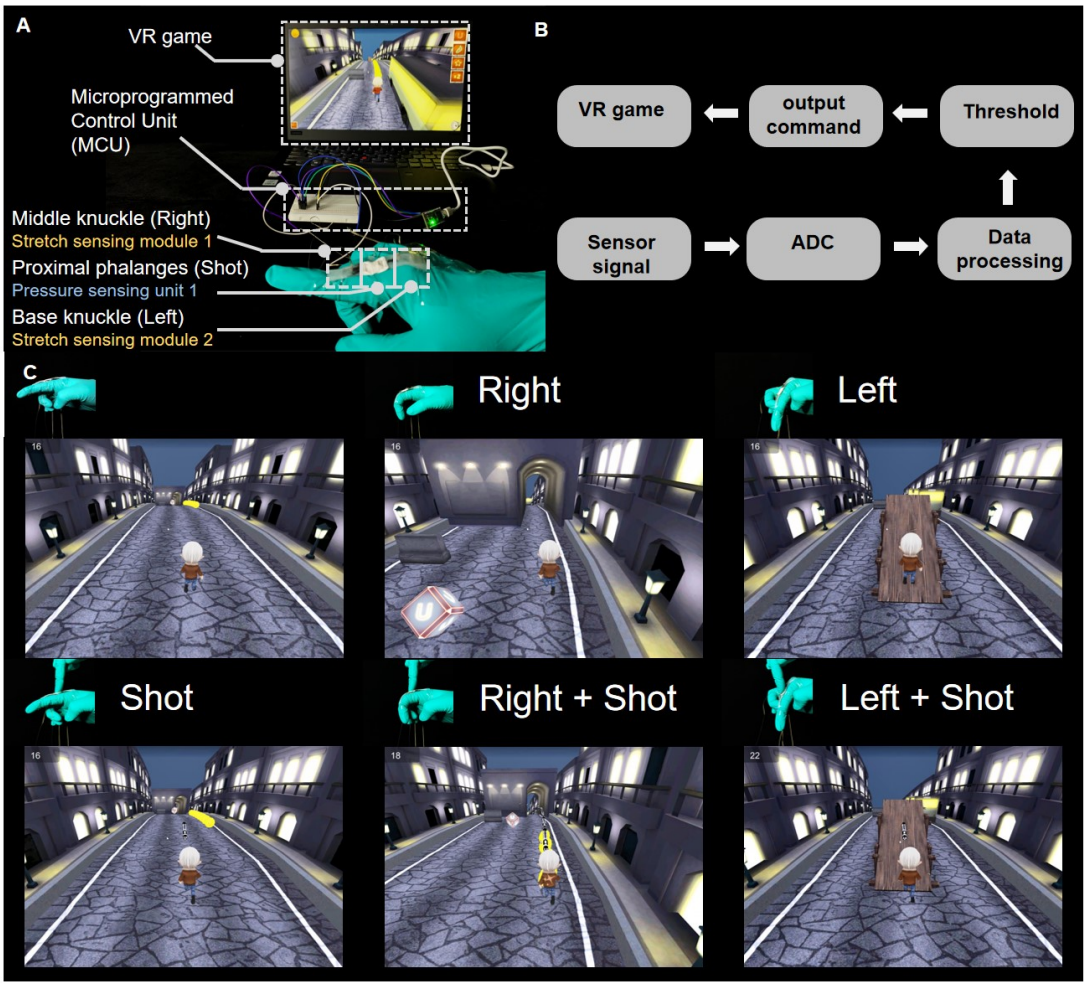

Figure 6.17 (A) Photograph of design and layout of human-machine interaction system. (B) The flow chart of human-machine interaction system. (C) Demonstration of real-time external stimuli received by the WMS interacting with the virtual gaming program.

6.6 Conclusion

Through a design strategy of a wing-like structure with the composition of different Yong's modulus pressure/stretch sensing modules, the WMS can accurately detect and differentiate multiple mechanical stimuli, including pressure, stretching,

convex and concave bending. The hierarchical in situ filling porous pressure sensing layer and wrinkled CNTs/Ag nanoflakes stretch sensing layer enable outstanding sensing performance in both pressure and stretching, including high sensitivity, fast response, low detection limitation, stability under various mechanical stimuli conditions, and long-term durability. Besides that, when measuring the stretching, the response of the stretch sensing module will not be interfered by the external perpendicular pressure due to the high thickness and compressibility of the hierarchical in situ filling porous sensing layer that withstands the entire pressure. For measuring the pressure, the signal of pressure sensing module is not disturbed by the external stretching process because both wings structure with a lower Young's modulus bears the entire strain. In addition, since the breakage and overlap of the CNTs/Ag nanoflakes conductive nanomaterial in stretch sensing module occur during convex and concave bending, the sensor is easy to differentiate and detect convex and concave bending. The WMS with detect and differentiate capabilities can be used to identify various mechanical stimuli in body kinesthesia, recognize objects of different types and sizes by robotic gripper, monitor locomotion and detect environment through a crawling robot, and human-machine interaction.

Chapter 7. Conclusion and perspective

7.1 Conclusion

In this work, we developed a piezoresistive pressure sensor with high sensitivity over a broad linear sensing range by 3D printing technique and emulsion template method. And we developed a wing-like multifunctional sensor with the capability of detect and differentiate multiple mechanical stimuli by structure design.

(1) A hierarchical in-situ filling porous pressure sensor with high sensitivity and high linearity over a broad sensing range is fabricated by DIW printing technique and emulsion template method. The hierarchical geometry has a broad sensing range because the multilayer lattice and internal porous structure increase contact area and distribute applied stress. The structure of in-situ formation of CNFs networks embedded inner porous structure, results in high sensitivity and high linearity. The effects of the porosity, CNFs mass ratio, structure types, stacked sensing layer numbers, and printed lattice types are thoroughly investigated. As a result, the 4-layer FCT hierarchical in situ filling porous structure with 60% porosity and 1 wt% CNFs, exhibits the highest sensitivity (4.7 kPa^{-1}) under the broad linear sensing range up to 1 MPa (R^2=0.99).

(2) In conclusion, the optimized HPPS is demonstrated to detect diverse stimuli from low pressure such as tiny object recognition, pulse detection and voice recognition, finger binding detection and human foot motion in medium pressure regimes, tire pressure monitoring in high pressure regions. The sensor is capable of detecting a low pressure change under high compression because of its high-pressure resolution. The sensor can be applied to personal electronics and biomedical

devices in the near future.

(3) A wing-like structured WMS is developed based on a hierarchical in situ filling porous and wrinkled CNT-Ag nanoflakes hybrid film as the active layer of the pressure sensing module and stretch sensing module, respectively. The hierarchical in situ filling porous is fabricated by emulsion template methods and DIW printing techniques, and the wrinkled CNT-Ag nanoflakes hybrid film is prepared by pre-stretch treatment and coating of CNTs-Ag nanoflakes conductive network. Different concentrations of CNF are studied to optimize the pressure sensing module, and different concentrations of CNTs and Ag nanoflakes, and the effect of pre-stretch treatment is investigated to optimize the stretch sensing module.

(4) The WMS can detect and differentiate multiple mechanical stimuli, including pressure, stretching, convex and concave bending due to the design strategy of a wing-like structure with different Yong's modulus pressure/stretch sensing modules. The high sensing performance, including high sensitivity, fast response, low detection limitation, stability under various mechanical stimuli conditions, and long-term durability in both stretch and pressure sensing, is achieved by the hierarchical in situ filling porous pressure sensing layer and the wrinkled CNTs/Ag nanoflakes stretch sensing layer. In addition, the response of the stretch sensing module will not be interfered by the external pressure because of the high thickness and compressibility of the hierarchical porous sensing layer that withstands the entire pressure. And the signal of pressure sensing module is not

disturbed by the lateral stretching process because both wings structure with a lower Young's modulus bears the entire strain. The sensor can also detect and differentiate the convex and concave bending caused by the breakage and overlap of the CNTs/Ag nanoflakes conductive nanomaterial in stretch sensing module. The WMS sensor is used to monitor body kinesthesia, identify objects of different types and sizes with a WMS-integrated robotic gripper, monitor locomotion and detect environment *via* a WMS-integrated crawling robot, and human-machine interaction.

7.2 Perspective

In this work, we focus on developing the resistive type of sensor with high sensing performance. Future work will be focused on developing functional material to prepare the sensor with different functionality to apply in different scenarios, developing a multimode wearable sensor, integrated with a Bluetooth module to achieve wireless transformation of the information.

(1) Functional material developing:

Most of the materials used in this work are based on commonly used materials such as PDMS, CNTs and CNFs. Next, we will utilize some functional material to fabricate wearable sensors with some other functionality, such as self-healing property, waterproofness, temperature or humidity stability to increase the robustness of wearable sensor.

(2) Multimode wearable sensor developing:

The wearable sensor developed in this work is only used to detect mechanical stimuli, including pressure, stretch and bending. It is important to develop the multimode wearable sensor with other sensing capabilities such as temperature, humidity, sweat, etc. This multimode wearable sensor can be used in human health monitoring to detect more physiological information.

(3) Wireless wearable sensor:

Most laboratory-developed wearable sensors require connection to a digital meter and a power source to conduct measurements. However, for real-time monitoring of the health condition, the sensor needs to be very small to be attached and carried by humans. Thus, there is more and more need to develop a wireless wearable sensor with a Bluetooth module and power module to transfer information directly into our phone.

Reference

1. Duking, P., Achtzehn, S., Holmberg, H. C. & Sperlich, B. Integrated Framework of Load Monitoring by a Combination of Smartphone Applications, Wearables and Point-of-Care Testing Provides Feedback that Allows Individual Responsive Adjustments to Activities of Daily Living. *Sensors (Basel)* **18**, (2018).

2. Yin, Ruiyang, et al. Wearable sensors-enabled human-machine interaction systems: from design to application. *Advanced Functional Materials* **31**, 2008936(2021).

3. Lim, H. R. et al. Advanced Soft Materials, Sensor Integrations, and Applications of Wearable Flexible Hybrid Electronics in Healthcare, Energy, and Environment. *Adv Mater* **32**, e1901924 (2020).

4. Liu, Y., Pharr, M. & Salvatore, G. A. Lab-on-Skin: A Review of Flexible and Stretchable Electronics for Wearable Health Monitoring. *ACS Nano* **11**, 9614–9635 (2017).

5. Gong, S. et al. A wearable and highly sensitive pressure sensor with ultrathin gold nanowires. *Nat Commun* **5**, 3132 (2014).

6. Huang, C. B. et al. Molecule-Graphene Hybrid Materials with Tunable Mechanoresponse: Highly Sensitive Pressure Sensors for Health Monitoring. *Adv Mater* **31**, e1804600 (2019).

7. Bai, N. et al. Graded intrafillable architecture-based iontronic pressure sensor with ultra-broad-range high sensitivity. *Nat Commun* **11**, 209 (2020).

8. Ji, B. et al. Bio-inspired hybrid dielectric for capacitive and triboelectric tactile sensors with high sensitivity and ultrawide linearity range. *Advanced Materials* **33**, 2100859 (2021).

9. Wang, Z. et al. Piezoelectric Nanogenerators Based on Zinc Oxide Nanowire Arrays. *Science* **312**, 242–246 (2006).

10. Shin, K.-Y., Lee, J. S. & Jang, J. Highly sensitive, wearable and wireless pressure sensor using free-standing ZnO nanoneedle/PVDF hybrid thin film for heart rate

monitoring. *Nano Energy* **22**, 95–104 (2016).

11. Zhu, X. X. et al. Triboelectrification-enabled touch sensing for self-powered position mapping and dynamic tracking by a flexible and area-scalable sensor array. *Nano Energy* **41**, 387–393 (2017).

12. Zhu, G. et al. Self-powered, ultrasensitive, flexible tactile sensors based on contact electrification. *Nano Lett* **14**, 3208–13 (2014).

13. Liu, Z. et al. Highly Breathable and Stretchable Strain Sensors with Insensitive Response to Pressure and Bending. *Advanced Functional Materials* **31**, 2007622 (2021).

14. Gao, J. et al. Ultra-Robust and Extensible Fibrous Mechanical Sensors for Wearable Smart Healthcare. *Adv Mater* **34**, e2107511 (2022).

15. Wang, L. et al. Highly Compressible, Thermally Stable, Light-Weight, and Robust Aramid Nanofibers/Ti(3)AlC(2) MXene Composite Aerogel for Sensitive Pressure Sensor. *ACS Nano* **14**, 10633–10647 (2020).

16. Wang, Z. et al. Flexible and Washable Poly(Ionic Liquid) Nanofibrous Membrane with Moisture Proof Pressure Sensing for Real-Life Wearable Electronics. *ACS Appl Mater Interfaces* **11**, 27200–27209 (2019).

17. Xu, J. et al. High sensitivity and broad linearity range pressure sensor based on hierarchical in-situ filling porous structure. *npj Flexible Electronics* **6**, (2022).

18. Xue, F. et al. An ultra-broad-range pressure sensor based on a gradient stiffness design. *Mater Horiz* **8**, 2260–2272 (2021).

19. Xu, H. et al. Flexible Waterproof Piezoresistive Pressure Sensors with Wide Linear Working Range Based on Conductive Fabrics. *Nanomicro Lett* **12**, 159 (2020).

20. Ma, L. et al. Ultra-sensitive, durable and stretchable ionic skins with biomimetic micronanostructures for multi-signal detection, high-precision motion monitoring, and underwater sensing. *Journal of Materials Chemistry A* **9**, 26949–26962 (2021).

21. Ruth, S. R. A., Feig, V. R., Tran, H. & Bao, Z. Microengineering Pressure Sensor Active Layers for Improved Performance. *Advanced Functional Materials* **30**, 2003491 (2020).

22. Shi, Z. et al. Morphological Engineering of Sensing Materials for Flexible

Pressure Sensors and Artificial Intelligence Applications. *Nanomicro Lett* **14**, 141 (2022).

23. Chen, W. & Yan, X. Progress in achieving high-performance piezoresistive and capacitive flexible pressure sensors: A review. *Journal of Materials Science & Technology* **43**, 175–188 (2020).

24. Mannsfeld, S. C. et al. Highly sensitive flexible pressure sensors with microstructured rubber dielectric layers. *Nat Mater* **9**, 859–64 (2010).

25. Luo, Y. et al. Flexible Capacitive Pressure Sensor Enhanced by Tilted Micropillar Arrays. *ACS Appl Mater Interfaces* **11**, 17796–17803 (2019).

26. Shuai, X. et al. Highly Sensitive Flexible Pressure Sensor Based on Silver Nanowires-Embedded Polydimethylsiloxane Electrode with Microarray Structure. *ACS Appl Mater Interfaces* **9**, 26314–26324 (2017).

27. Kim, J. O. et al. Highly Ordered 3D Microstructure-Based Electronic Skin Capable of Differentiating Pressure, Temperature, and Proximity. *ACS Appl Mater Interfaces* **11**, 1503–1511 (2019).

28. Amjadi, M., Kyung, K.-U., Park, I. & Sitti, M. Stretchable, Skin-Mountable, and Wearable Strain Sensors and Their Potential Applications: A Review. *Advanced Functional Materials* **26**, 1678–1698 (2016).

29. Nesser, H. & Lubineau, G. Strain Sensing by Electrical Capacitive Variation: From Stretchable Materials to Electronic Interfaces. *Advanced Electronic Materials* **7**, 2100190 (2021).

30. Qin, J. et al. Flexible and stretchable capacitive sensors with different microstructures. *Advanced Materials* **33**, 2008267 (2021).

31. Nur, R. et al. A Highly Sensitive Capacitive-type Strain Sensor Using Wrinkled Ultrathin Gold Films. *Nano Lett* **18**, 5610–5617 (2018).

32. Zhao, X. et al. Flexible, Stretchable and Wearable Multifunctional Sensor Array as Artificial Electronic Skin for Static and Dynamic Strain Mapping. *Advanced Electronic Materials* **1**, 1500142 (2015).

33. Hua, Q. et al. Skin-inspired highly stretchable and conformable matrix networks for multifunctional sensing. *Nat Commun* **9**, 244 (2018).

34. Cooper, C. B. et al. Stretchable Capacitive Sensors of Torsion, Strain, and Touch Using Double Helix Liquid Metal Fibers. *Advanced Functional Materials* **27**, 1605630 (2017).

35. Lei, H. et al. Advances in self-powered triboelectric pressure sensors. *Journal of Materials Chemistry A* **9**, 20100–20130 (2021).

36. Wang, H. et al. Triboelectric nanogenerators for human-health care. *Science Bulletin* **66**, 490–511 (2021).

37. Chen, S. et al. Hierarchical elastomer tuned self-powered pressure sensor for wearable multifunctional cardiovascular electronics. *Nano Energy* **70**, 104460 (2020).

38. Ha, M. et al. Skin-Inspired Hierarchical Polymer Architectures with Gradient Stiffness for Spacer-Free, Ultrathin, and Highly Sensitive Triboelectric Sensors. *ACS Nano* **12**, 3964–3974 (2018).

39. Ahmed, A., Hassan, I. & Zu, J. Design Guidelines of Stretchable Pressure Sensors-Based Triboelectrification. *Advanced Engineering Materials* **20**, 1700997 (2018).

40. Li, X. et al. Improved triboelectrification effect by bendable and slidable fish-scale-like microstructures. *Nano Energy* **40**, 646–654 (2017).

41. Yi, F. et al. Stretchable-Rubber-Based Triboelectric Nanogenerator and Its Application as Self-Powered Body Motion Sensors. *Advanced Functional Materials* **25**, 3688–3696 (2015).

42. Wang, F. et al. Self-Powered Sensor Based on Bionic Antennae Arrays and Triboelectric Nanogenerator for Identifying Noncontact Motions. *Advanced Materials Technologies* **5**, 1900789 (2019).

43. Jang, J., Lee, J., Jang, J. H. & Choi, H. A Triboelectric-Based Artificial Basilar Membrane to Mimic Cochlear Tonotopy. *Adv Healthc Mater* **5**, 2481–2487 (2016).

44. Wu, Y. et al. A Self-Powered Angle Measurement Sensor Based on Triboelectric Nanogenerator. *Advanced Functional Materials* **25**, 2166–2174 (2015).

45. Zhao, Z., Dai, Y., Dou, S. X. & Liang, J. Flexible nanogenerators for wearable electronic applications based on piezoelectric materials. *Materials Today Energy* **20**, 100690 (2021).

46. Wu, Y., Ma, Y., Zheng, H. & Ramakrishna, S. Piezoelectric materials for flexible and wearable electronics: A review. *Materials & Design* **211**, 110164 (2021).

47. Dagdeviren, C. et al. Recent progress in flexible and stretchable piezoelectric devices for mechanical energy harvesting, sensing and actuation. *Extreme Mechanics Letters* **9**, 269–281 (2016).

48. Chen, X. et al. Flexible fiber-based hybrid nanogenerator for biomechanical energy harvesting and physiological monitoring. *Nano Energy* **38**, 43–50 (2017).

49. Yildirim, A. et al. Roll-to-Roll (R2R) Production of Ultrasensitive, Flexible, and Transparent Pressure Sensors Based on Vertically Aligned Lead Zirconate Titanate and Graphene Nanoplatelets. *Advanced Materials Technologies* **4**, 1800425 (2019).

50. Persano, L. et al. High performance piezoelectric devices based on aligned arrays of nanofibers of poly(vinylidenefluoride-co-trifluoroethylene). *Nat Commun* **4**, 1633 (2013).

51. Liu, H. et al. Enhanced performance of piezoelectric composite nanogenerator based on gradient porous PZT ceramic structure for energy harvesting. *Journal of Materials Chemistry A* **8**, 19631–19640 (2020).

52. Kim, Y.-G., Song, J.-H., Hong, S. & Ahn, S.-H. Piezoelectric strain sensor with high sensitivity and high stretchability based on kirigami design cutting. *npj Flexible Electronics* **6**, (2022).

53. Sun, R. et al. Stretchable Piezoelectric Sensing Systems for Self-Powered and Wireless Health Monitoring. *Advanced Materials Technologies* **4**, 1900100 (2019).

54. Deng, W. et al. Cowpea-structured PVDF/ZnO nanofibers based flexible self-powered piezoelectric bending motion sensor towards remote control of gestures. *Nano Energy* **55**, 516–525 (2019).

55. Han, J. H. et al. Basilar membrane-inspired self-powered acoustic sensor enabled by highly sensitive multi tunable frequency band. *Nano Energy* **53**, 198–205 (2018).

56. He, J. et al. Recent advances of wearable and flexible piezoresistivity pressure sensor devices and its future prospects. *Journal of Materiomics* **6**, 86–101 (2020).

57. Cheng, M. et al. A review of flexible force sensors for human health monitoring. *J Adv Res* **26**, 53–68 (2020).

58. Peng, X. et al. A mechanically strong and sensitive CNT/rGO–CNF carbon aerogel for piezoresistive sensors. *Journal of Materials Chemistry A* **6**, 23550–23559 (2018).

59. Zhang, S. et al. Enhanced piezoresistive performance of conductive WPU/CNT composite foam through incorporating brittle cellulose nanocrystal. *Chemical Engineering Journal* **387**, 124045 (2020).

60. Wei, Y. et al. Flexible piezoresistive sensors based on "dynamic bridging effect" of silver nanowires toward graphene. *Carbon* **113**, 395–403 (2017).

61. Kim, K. et al. Highly Sensitive and Wearable Liquid Metal-Based Pressure Sensor for Health Monitoring Applications: Integration of a 3D-Printed Microbump Array with the Microchannel. *Adv Healthc Mater* **8**, e1900978 (2019).

62. Wang, J. C. et al. Miniaturized Flexible Piezoresistive Pressure Sensors: Poly(3,4-ethylenedioxythiophene):Poly(styrenesulfonate) Copolymers Blended with Graphene Oxide for Biomedical Applications. *ACS Appl Mater Interfaces* **11**, 34305–34315 (2019).

63. Arias-Ferreiro, G. et al. Flexible 3D Printed Acrylic Composites based on Polyaniline/Multiwalled Carbon Nanotubes for Piezoresistive Pressure Sensors. *Advanced Electronic Materials* **8**, 2200590 (2022).

64. Ma, C. et al. Robust Flexible Pressure Sensors Made from Conductive Micropyramids for Manipulation Tasks. *ACS Nano* **14**, 12866–12876 (2020).

65. Jung, Y. et al. Irregular Microdome Structure-Based Sensitive Pressure Sensor Using Internal Popping of Microspheres. *Advanced Functional Materials* **32**, 2201147 (2022).

66. Park, H. et al. Stretchable Array of Highly Sensitive Pressure Sensors Consisting of Polyaniline Nanofibers and Au-Coated Polydimethylsiloxane Micropillars. *ACS Nano* **9**, 9974–9985 (2015).

67. Shen, Y., Wang, Y., Luo, Z. & Wang, B. Durable, Sensitive, and Wide-Range Wearable Pressure Sensors Based on Wavy-Structured Flexible Conductive Composite Film. *Macromolecular Materials and Engineering* **305**, 2000206 (2020).

68. Wang, Y., Chao, M., Wan, P. & Zhang, L. A wearable breathable pressure sensor

from metal-organic framework derived nanocomposites for highly sensitive broad-range healthcare monitoring. *Nano Energy* **70**, 104560 (2020).

69. Zhao, T. et al. Highly Sensitive Flexible Piezoresistive Pressure Sensor Developed Using Biomimetically Textured Porous Materials. *ACS Appl Mater Interfaces* **11**, 29466–29473 (2019).

70. Yin, Y. M. et al. Facile Fabrication of Flexible Pressure Sensor with Programmable Lattice Structure. *ACS Appl Mater Interfaces* **13**, 10388–10396 (2021).

71. Wang, Z. et al. Full 3D Printing of Stretchable Piezoresistive Sensor with Hierarchical Porosity and Multimodulus Architecture. *Advanced Functional Materials* **29**, 1807569 (2019).

72. Zhang, L. et al. Thiolated Graphene@Polyester Fabric-Based Multilayer Piezoresistive Pressure Sensors for Detecting Human Motion. *ACS Appl Mater Interfaces* **10**, 41784–41792 (2018).

73. Wu, S., Peng, S., Yu, Y. & Wang, C. H. Strategies for Designing Stretchable Strain Sensors and Conductors. *Advanced Materials Technologies* **5**, 1900908 (2020).

74. Choi, S. et al. Highly conductive, stretchable and biocompatible Ag-Au core-sheath nanowire composite for wearable and implantable bioelectronics. *Nat Nanotechnol* **13**, 1048–1056 (2018).

75. Lin, Y. et al. Graphene-Elastomer Composites with Segregated Nanostructured Network for Liquid and Strain Sensing Application. *ACS Appl Mater Interfaces* **8**, 24143–51 (2016).

76. Yu, Y. et al. Flexible and transparent strain sensors based on super-aligned carbon nanotube films. *Nanoscale* **9**, 6716–6723 (2017).

77. Wang, Z. et al. Dually Synergetic Network Hydrogels with Integrated Mechanical Stretchability, Thermal Responsiveness, and Electrical Conductivity for Strain Sensors and Temperature Alertors. *ACS Appl Mater Interfaces* **10**, 14045–14054 (2018).

78. Yue, W. et al.A Highly Stretchable, Transparent, and Conductive Polymer. *Science Advances* **3.3**, e1602076(2017).

79. Cai, G. et al. Flexible and wearable strain sensing fabrics. *Chemical Engineering*

Journal **325**, 396–403 (2017).

80. Chen, J. et al. Superelastic, Sensitive, and Low Hysteresis Flexible Strain Sensor Based on Wave-Patterned Liquid Metal for Human Activity Monitoring. *ACS Appl Mater Interfaces* **12**, 22200–22211 (2020).

81. Li, S. et al. Contact-Resistance-Free Stretchable Strain Sensors with High Repeatability and Linearity. *ACS Nano* **16**, 541–553 (2022).

82. Gao, Y. et al. Winding-Locked Carbon Nanotubes/Polymer Nanofibers Helical Yarn for Ultrastretchable Conductor and Strain Sensor. *ACS Nano* **14**, 3442–3450 (2020).

83. Li, L. et al. Stretchable and ultrasensitive strain sensor based on a bilayer wrinkle-microcracking mechanism. *Chemical Engineering Journal* **437**, 135399 (2022).

84. Ma, J. et al. Highly Sensitive and Large-Range Strain Sensor with a Self-Compensated Two-Order Structure for Human Motion Detection. *ACS Appl Mater Interfaces* **11**, 8527–8536 (2019).

85. Xu, K. et al. Highly stable kirigami-structured stretchable strain sensors for perdurable wearable electronics. *Journal of Materials Chemistry C* **7**, 9609–9617 (2019).

86. Zhou, C. G. et al. Highly Stretchable and Sensitive Strain Sensor with Porous Segregated Conductive Network. *ACS Appl Mater Interfaces* **11**, 37094–37102 (2019).

87. He, F. et al. Recent Progress in Flexible Microstructural Pressure Sensors toward Human-Machine Interaction and Healthcare Applications. *Small Methods* **5**, e2001041 (2021).

88. Lu, Y. et al. An ultra-sensitive wearable multifunctional flexible sensor with a self-assembled dual 3D conductive network and yeast-foamed silicone rubber foam. *Journal of Materials Chemistry A* **10**, 22551–22560 (2022).

89. Ho, M. D. et al. Percolating Network of Ultrathin Gold Nanowires and Silver Nanowires toward “Invisible” Wearable Sensors for Detecting Emotional Expression and Apexcardiogram. *Advanced Functional Materials* **27**, 1700845 (2017).

90. Sun, R. et al. Magnetically induced robust anisotropic structure of multi-walled carbon nanotubes/Ni for high-performance flexible strain sensor. *Carbon* **194**, 185–196 (2022).

91. Kim, J. et al. Soft Wearable Pressure Sensors for Beat-to-Beat Blood Pressure Monitoring. *Adv Healthc Mater* **8**, e1900109 (2019).

92. Ning, C. et al. Helical Fiber Strain Sensors Based on Triboelectric Nanogenerators for Self-Powered Human Respiratory Monitoring. *ACS Nano* **16**, 2811–2821 (2022).

93. Deng, C. et al. Self-Powered Insole Plantar Pressure Mapping System. *Advanced Functional Materials* **28**, 1801606 (2018).

94. Ameri, S. K. et al. Imperceptible electrooculography graphene sensor system for human–robot interface. *npj 2D Materials and Applications* **2**, (2018).

95. He, Q. et al. Triboelectric vibration sensor for a human-machine interface built on ubiquitous surfaces. *Nano Energy* **59**, 689–696 (2019).

96. Shen, S. et al. Human Machine Interface with Wearable Electronics Using Biodegradable Triboelectric Films for Calligraphy Practice and Correction. *Nanomicro Lett* **14**, 225 (2022).

97. Lee, H. J. et al. Hetero-Dimensional 2D Ti(3)C(2)T(x) MXene and 1D Graphene Nanoribbon Hybrids for Machine Learning-Assisted Pressure Sensors. *ACS Nano* **15**, 10347–10356 (2021).

98. Guo, Y. et al. Recent Advances in Carbon Material-Based Multifunctional Sensors and Their Applications in Electronic Skin Systems. *Advanced Functional Materials* **31**, 2104288 (2021).

99. Qi, K. et al. A Highly Stretchable Nanofiber-Based Electronic Skin with Pressure-, Strain-, and Flexion-Sensitive Properties for Health and Motion Monitoring. *ACS Appl Mater Interfaces* **9**, 42951–42960 (2017).

100. He, F. et al. Stretchable, Biocompatible, and Multifunctional Silk Fibroin-Based Hydrogels toward Wearable Strain/Pressure Sensors and Triboelectric Nanogenerators. *ACS Appl Mater Interfaces* **12**, 6442–6450 (2020).

101. Park, H. et al. Microporous Polypyrrole-Coated Graphene Foam for

High-Performance Multifunctional Sensors and Flexible Supercapacitors. *Advanced Functional Materials* **28**, 1707013 (2018).

102. Cheng, Y., Wang, R., Zhai, H. & Sun, J. Stretchable electronic skin based on silver nanowire composite fiber electrodes for sensing pressure, proximity, and multidirectional strain. *Nanoscale* **9**, 3834–3842 (2017).

103. Won, S. M. et al. Multimodal Sensing with a Three-Dimensional Piezoresistive Structure. *ACS Nano* **13**, 10972–10979 (2019).

104. Sun, K. et al. Hybrid Architectures of Heterogeneous Carbon Nanotube Composite Microstructures Enable Multiaxial Strain Perception with High Sensitivity and Ultrabroad Sensing Range. *Small* **14**, e1803411 (2018).

105. Lee, J. H. et al. Highly Aligned, Anisotropic Carbon Nanofiber Films for Multidirectional Strain Sensors with Exceptional Selectivity. *Advanced Functional Materials* **29**, 1901623 (2019).

106. Schwartz, G. et al. Flexible polymer transistors with high pressure sensitivity for application in electronic skin and health monitoring. *Nat Commun* **4**, 1859 (2013).

107. Son, D. et al. Multifunctional wearable devices for diagnosis and therapy of movement disorders. *Nat Nanotechnol* **9**, 397–404 (2014).

108. Chen, G. et al. Electronic Textiles for Wearable Point-of-Care Systems. *Chem Rev* **122**, 3259–3291 (2022).

109. Meng, K. et al. Wearable Pressure Sensors for Pulse Wave Monitoring. *Adv Mater* **34**, e2109357 (2022).

110.Libanori, A. et al. Smart textiles for personalized healthcare. *Nature Electronics* **5**, 142–156 (2022).

111.Rus, D. & Tolley, M. T. Design, fabrication and control of soft robots. *Nature* **521**, 467–75 (2015).

112. Kim, Y. et al. A bioinspired flexible organic artificial afferent nerve. *Science* **360** (2018).

113.Jung, S. et al. Reverse-micelle-induced porous pressure-sensitive rubber for wearable human-machine interfaces. *Adv Mater* **26**, 4825–30 (2014).

114.Jeong, J. W. et al. Materials and optimized designs for human-machine interfaces

via epidermal electronics. *Advanced Materials* **25**, 6839–6846 (2013).

115. Araromi, O. A. et al. Ultra-sensitive and resilient compliant strain gauges for soft machines. *Nature* **587**, 219–224 (2020).

116. Gorissen, B. et al. Elastic Inflatable Actuators for Soft Robotic Applications. *Adv Mater* **29**, 1604977 (2017).

117. Kim, J. et al. Stretchable silicon nanoribbon electronics for skin prosthesis. *Nat Commun* **5**, 5747 (2014).

118. Liu, W. et al. Piezoresistive pressure sensor based on synergistical innerconnect polyvinyl alcohol nanowires/wrinkled graphene film. *Small* **14**, 1704149 (2018).

119. Choong, C. L. et al. Highly stretchable resistive pressure sensors using a conductive elastomeric composite on a micropyramid array. *Advanced materials* **26**, 3451–3458 (2014).

120. Park, J. et al. Giant Tunneling Piezoresistance of Composite Elastomers with Interlocked Microdome Arrays for Ultrasensitive and Multimodal Electronic Skins. *Acs Nano* **8.5,** 4689–97 (2014):.

121. Ghosh, R. et al. Fabrication of piezoresistive Si nanorod-based pressure sensor arrays: A promising candidate for portable breath monitoring devices. *Nano Energy* **80**, 105537 (2021).

122. Pang, C. et al. A flexible and highly sensitive strain-gauge sensor using reversible interlocking of nanofibres. *Nat Mater* **11**, 795–801 (2012).

123. Zhou, K. et al. Template-Directed Growth of Hierarchical MOF Hybrid Arrays for Tactile Sensor. *Advanced Functional Materials* **30**, 2001296 (2020).

124. Li, X. et al. Ultracomfortable Hierarchical Nanonetwork for Highly Sensitive Pressure Sensor. *ACS Nano* **14**, 9605–9612 (2020).

125. Yang, T. et al. Hierarchically Microstructure-Bioinspired Flexible Piezoresistive Bioelectronics. *ACS Nano* **15**, 11555–11563 (2021).

126. Kim, S. et al. Wearable, ultrawide-range, and bending-insensitive pressure sensor based on carbon nanotube network-coated porous elastomer sponges for human interface and healthcare devices. *ACS applied materials & interfaces* **11**, 23639–23648 (2019).

127. Lee, Y. et al. Flexible ferroelectric sensors with ultrahigh pressure sensitivity and linear response over exceptionally broad pressure range. *Acs Nano* **12**, 4045–4054 (2018).

128. Turco, A. et al. An innovative, fast and facile soft-template approach for the fabrication of porous PDMS for oil-water separation. *Journal of Materials Chemistry A* **5**, 23785–23793 (2017).

129. Zhang, L. et al. Paraffin oil based soft-template approach to fabricate reusable porous pdms sponge for effective oil/water separation. *Langmuir* **35**, 11123–11131 (2019).

130. Xu, J. et al. Selective coaxial ink 3D printing for single-pass fabrication of smart elastomeric foam with embedded stretchable sensor. *Additive Manufacturing* **36**, 101487 (2020).

131. Zou, B. et al. Repurposed Leather with Sensing Capabilities for Multifunctional Electronic Skin. *Adv Sci (Weinh)* **6**, 1801283 (2019).

132. Bae, G. Y. et al. Linearly and Highly Pressure-Sensitive Electronic Skin Based on a Bioinspired Hierarchical Structural Array. *Adv Mater* **28**, 5300–6 (2016).

133. Liu, M. et al. Large-Area All-Textile Pressure Sensors for Monitoring Human Motion and Physiological Signals. *Adv Mater* **29**, 1703700 (2017).

134. Shi, J. et al. Multiscale Hierarchical Design of a Flexible Piezoresistive Pressure Sensor with High Sensitivity and Wide Linearity Range. *Small* **14**, e1800819 (2018).

135. Guo, Y. et al. A Wearable Transient Pressure Sensor Made with MXene Nanosheets for Sensitive Broad-Range Human-Machine Interfacing. *Nano Lett* **19**, 1143–1150 (2019).

136. Yu, T. et al. Graphene foam pressure sensor based on fractal electrode with high sensitivity and wide linear range. *Carbon* **182**, 497–505 (2021).

137. Chao, M. et al. Breathable Ti(3)C(2)T(x) MXene/Protein Nanocomposites for Ultrasensitive Medical Pressure Sensor with Degradability in Solvents. *ACS Nano* **15**, 9746–9758 (2021).

138. Li, W. et al. Synergy of Porous Structure and Microstructure in Piezoresistive

Material for High-Performance and Flexible Pressure Sensors. *ACS Appl Mater Interfaces* **13**, 19211–19220 (2021).

139. Zheng, Y. et al. Conductive MXene/cotton fabric based pressure sensor with both high sensitivity and wide sensing range for human motion detection and E-skin. *Chemical Engineering Journal* **420**, 127720 (2021).

140. Wu, Q. et al. Triode-Mimicking Graphene Pressure Sensor with Positive Resistance Variation for Physiology and Motion Monitoring. *ACS Nano* **14**, 10104–10114 (2020).

141. Zhao, T. et al. Pollen-Shaped Hierarchical Structure for Pressure Sensors with High Sensitivity in an Ultrabroad Linear Response Range. *ACS Appl Mater Interfaces* **12**, 55362–55371 (2020).

142. Zhu, G. et al. 3D Printed Skin-Inspired Flexible Pressure Sensor with Gradient Porous Structure for Tunable High Sensitivity and Wide Linearity Range. *Advanced Materials Technologies* **7**, 2101239 (2021).

143. Bae, K. et al. Large-Area, Crosstalk-Free, Flexible Tactile Sensor Matrix Pixelated by Mesh Layers. *ACS Appl Mater Interfaces* **13**, 12259–12267 (2021).

144. Yue, Z. et al. Sponge Graphene Aerogel Pressure Sensors with an Extremely Wide Operation Range for Human Recognition and Motion Detection. *ACS Applied Electronic Materials* **3**, 1301–1310 (2021).

145. Bai, N. et al. Graded Interlocks for Iontronic Pressure Sensors with High Sensitivity and High Linearity over a Broad Range. *ACS Nano* **16**, 4338–4347 (2022).

146. Zhang, Y. et al. Highly stable flexible pressure sensors with a quasi-homogeneous composition and interlinked interfaces. *Nat Commun* **13**, 1317 (2022).

147. Lee, Y. et al. Bioinspired Gradient Conductivity and Stiffness for Ultrasensitive Electronic Skins. *ACS Nano* **15**, 1795–1804 (2021).

148. Park, J. et al. Tailoring force sensitivity and selectivity by microstructure engineering of multidirectional electronic skins. *NPG Asia Materials* **10**, 163–176 (2018).

149. Kim, Y. R. et al. Binary Spiky/Spherical Nanoparticle Films with

Hierarchical Micro/Nanostructures for High-Performance Flexible Pressure Sensors. *ACS Appl Mater Interfaces* **12**, 58403–58411 (2020).

150. Pyo, S. et al. Multi-Layered, Hierarchical Fabric-Based Tactile Sensors with High Sensitivity and Linearity in Ultrawide Pressure Range. *Advanced Functional Materials* **29**, 1902484 (2019).

151. Nie, B. et al. Textile-Based Wireless Pressure Sensor Array for Human-Interactive Sensing. *Advanced Functional Materials* **29**, 1808786 (2019).

152. van Schie, C. H. A review of the biomechanics of the diabetic foot. *Int J Low Extrem Wounds* **4**, 160–70 (2005).

153. Pang, Y. et al. Epidermis Microstructure Inspired Graphene Pressure Sensor with Random Distributed Spinosum for High Sensitivity and Large Linearity. *ACS Nano* **12**, 2346–2354 (2018).

154. Boutry, C. M. et al. Biodegradable and flexible arterial-pulse sensor for the wireless monitoring of blood flow. *Nat Biomed Eng* **3**, 47–57 (2019).

155. Chung, H. U. et al. Binodal, wireless epidermal electronic systems with in-sensor analytics for neonatal intensive care. *Science* **363**, eaau0780 (2019).

156. Tang, H. et al. In Situ Forming Epidermal Bioelectronics for Daily Monitoring and Comprehensive Exercise. *ACS Nano* **16**, 17931–17947 (2022).

157. Zhao, S. & Zhu, R. Electronic Skin with Multifunction Sensors Based on Thermosensation. *Adv Mater* **29**, 1606151 (2017).

158. Cao, J. et al. Ultra-robust stretchable electrode for e-skin: In situ assembly using a nanofiber scaffold and liquid metal to mimic water-to-net interaction. *InfoMat* **4**, e12302 (2022).

159. Kim, K. K. et al. Evolvable Skin Electronics by In Situ and In Operando Adaptation. *Advanced Functional Materials* **32**, 2106329 (2021).

160. Li, L. et al. Dual sensing signal decoupling based on tellurium anisotropy for VR interaction and neuro-reflex system application. *Nat Commun* **13**, 5975 (2022).

161. Yu, X. et al. Skin-integrated wireless haptic interfaces for virtual and augmented reality. *Nature* **575**, 473–479 (2019).

162. Sun, Z., Zhu, M., Shan, X. & Lee, C. Augmented tactile-perception and

haptic-feedback rings as human-machine interfaces aiming for immersive interactions. *Nat Commun* **13**, 5224 (2022).

163. Oh, Hongseok, et al. Scalable tactile sensor arrays on flexible substrates with high spatiotemporal resolution enabling slip and grip for closed-loop robotics. *Science advances* **6.46**, eabd7795(2020).

164. Yin, Y. et al. A flexible dual parameter sensor with hierarchical porous structure for fully decoupled pressure–temperature sensing. *Chemical Engineering Journal* **430**, 133158 (2022).

165. Kong, H. et al. Skin-Inspired Hair-Epidermis-Dermis Hierarchical Structures for Electronic Skin Sensors with High Sensitivity over a Wide Linear Range. *ACS Nano* **15**, 16218–16227 (2021).

166. Oh, J. et al. Pressure Insensitive Strain Sensor with Facile Solution-Based Process for Tactile Sensing Applications. *ACS Nano* **12**, 7546–7553 (2018).

167. Su, Qi, et al. A stretchable and strain-unperturbed pressure sensor for motion interference–free tactile monitoring on skins. *Science advances* **7.48**, eabi4563(2021).

168. Park, S. et al. Stretchable energy-harvesting tactile electronic skin capable of differentiating multiple mechanical stimuli modes. *Adv Mater* **26**, 7324–32 (2014).

169. Li, X. et al. Differentiation of Multiple Mechanical Stimuli by a Flexible Sensor Using a Dual-Interdigital-Electrode Layout for Bodily Kinesthetic Identification. *ACS Appl Mater Interfaces* **13**, 26394–26403 (2021).

170. Chen, H. et al. Human skin-inspired integrated multidimensional sensors based on highly anisotropic structures. *Materials Horizons* **7**, 2378–2389 (2020).

171. Lei, M. et al. Breathable and Waterproof Electronic Skin with Three-Dimensional Architecture for Pressure and Strain Sensing in Nonoverlapping Mode. *ACS Nano* **16**, 12620–12634 (2022).

172. Zhao, P. et al. Strain-Discriminable Pressure/Proximity Sensing of Transparent Stretchable Electronic Skin Based on PEDOT:PSS/SWCNT Electrodes. *ACS Appl Mater Interfaces* **12**, 55083–55093 (2020).

173. Shi, X. et al. Lowering Internal Friction of 0D-1D-2D Ternary Nanocomposite-Based Strain Sensor by Fullerene to Boost the Sensing Performance.

Advanced Functional Materials **28**, 1800850 (2018).

174. Cai, Y. et al. Stretchable Ti(3)C(2)T(x) MXene/Carbon Nanotube Composite Based Strain Sensor with Ultrahigh Sensitivity and Tunable Sensing Range. *ACS Nano* **12**, 56–62 (2018).

175. Wang, Y. F. et al. Printed Strain Sensor with High Sensitivity and Wide Working Range Using a Novel Brittle-Stretchable Conductive Network. *ACS Appl Mater Interfaces* **12**, 35282–35290 (2020).

176. Liu, Q., Chen, J., Li, Y. & Shi, G. High-Performance Strain Sensors with Fish-Scale-Like Graphene-Sensing Layers for Full-Range Detection of Human Motions. *ACS Nano* **10**, 7901–6 (2016).

177. Sun, H. et al. A Highly Sensitive and Stretchable Yarn Strain Sensor for Human Motion Tracking Utilizing a Wrinkle-Assisted Crack Structure. *ACS Appl Mater Interfaces* **11**, 36052–36062 (2019).

178. Zhang, H. et al. Anisotropic, Wrinkled, and Crack-Bridging Structure for Ultrasensitive, Highly Selective Multidirectional Strain Sensors. *Nanomicro Lett* **13**, 122 (2021).

179. Gu, J., Kwon, D., Ahn, J. & Park, I. Wearable Strain Sensors Using Light Transmittance Change of Carbon Nanotube-Embedded Elastomers with Microcracks. *ACS Appl Mater Interfaces* **12**, 10908–10917 (2020).

180. Yi, Q. et al. All-3D-Printed, Flexible, and Hybrid Wearable Bioelectronic Tactile Sensors Using Biocompatible Nanocomposites for Health Monitoring. *Advanced Materials Technologies* **7**, 2101034 (2021).

181. Tee, B. C. K. et al. Tunable Flexible Pressure Sensors using Microstructured Elastomer Geometries for Intuitive Electronics. *Advanced Functional Materials* **24**, 5427–5434 (2014).

182. Johnston, I. D. et al. Mechanical characterization of bulk Sylgard 184 for microfluidics and microengineering. *Journal of Micromechanics and Microengineering* **24.3**, 035017 (2014).

183. Dai, Z. et al. Optimization of bidirectional bending sensor as flexible ternary terminal for high-capacity human-machine interaction. *Nano Energy* **97**, 107173

(2022).

184. Zhou, Y. et al. Asymmetric Structure Based Flexible Strain Sensor for Simultaneous Detection of Various Human Joint Motions. *ACS Applied Electronic Materials* **1**, 1866–1872 (2019).

185. Xu, X.-L. et al. High-performance strain sensor for detection of human motion and subtle strain by facile fabrication. *Measurement* **189**, 110658 (2022).

186. Yan, J. et al. Bionic MXene based hybrid film design for an ultrasensitive piezoresistive pressure sensor. *Chemical Engineering Journal* **431**, 133458 (2022).

187. Shu, Q. et al. Magnetic flexible sensor with tension and bending discriminating detection. *Chemical Engineering Journal* **433**, 134424 (2022).

188. Feng, H. et al. Triboelectric nanogenerator based on direct image lithography and surface fluorination for biomechanical energy harvesting and self-powered sterilization. *Nano Energy* **98**, 107279 (2022).

189. Li, Y. et al. Multifunctional biomimetic tactile system via a stick-slip sensing strategy for human–machine interactions. *npj Flexible Electronics* **6**, (2022).

190. Song, Z. et al. A flexible triboelectric tactile sensor for simultaneous material and texture recognition. *Nano Energy* **93**, 106798 (2022).

191. Zhang, S. et al. Nondestructive Dimension Sorting by Soft Robotic Grippers Integrated with Triboelectric Sensor. *ACS nano* **16,** 3008–3016 (2022).

192. Qu, Xuecheng, et al. Artificial tactile perception smart finger for material identification based on triboelectric sensing. *Science Advances* **8.31**, eabq2521(2022).

193. Liu, Z. et al. Somatosensitive film soft crawling robots driven by artificial muscle for load carrying and multi-terrain locomotion. *Mater Horiz* **8**, 1783–1794 (2021).

194. Luo, X. J. et al. Multifunctional Ti3C2Tx MXene/Low-Density Polyethylene Soft Robots with Programmable Configuration for Amphibious Motions. *ACS applied materials & interfaces* **13,** 45833–45842 (2021).

195. Zhang, P. et al. Integrated 3D printing of flexible electroluminescent devices and soft robots. *Nat Commun* **13**, 4775 (2022).

196. Liao, X. et al. Hetero-contact microstructure to program discerning tactile

interactions for virtual reality. *Nano Energy* **60**, 127–136 (2019).

Biography

[1] Xu, J., Li, H., Yin, Y., Li, X., Cao, J., Feng, H., ... & Zhu, G. (2022). High sensitivity and broad linearity range pressure sensor based on hierarchical in-situ filling porous structure. npj Flexible Electronics, 6(1), 1–12.

[2] Feng, H., Li, H., Xu, J., Yin, Y., Cao, J., Yu, R., ... & Zhu, G. (2022). Triboelectric nanogenerator based on direct image lithography and surface fluorination for biomechanical energy harvesting and self-powered sterilization. Nano Energy, 98, 107279.

[3] Yin, Y. M., Li, H. Y., Xu, J., Zhang, C., Liang, F., Li, X., ... & Zhu, G. (2021). Facile fabrication of flexible pressure sensor with programmable lattice structure. ACS Applied Materials & Interfaces, 13(8), 10388–10396.

[4] Yin, Y., Wang, Y., Li, H., Xu, J., Zhang, C., Li, X., ... & Zhu, G. (2022). A flexible dual parameter sensor with hierarchical porous structure for fully decoupled pressure–temperature sensing. Chemical Engineering Journal, 430, 133158.

[5] Cao, J., Liang, F., Li, H., Li, X., Fan, Y., Hu, C., ... & Li, R. W. (2022). Ultra-robust stretchable electrode for e-skin: In situ assembly using a nanofiber scaffold and liquid metal to mimic water-to-net interaction. InfoMat, 4(4), e12302.

[6] Visaveliya, N. R., Kelestemur, S., Khatoon, F., Xu, J., Leo, K., Peter, L. S., ... & Eisele, D. M. (2022). Microfluidic-supported synthesis of anisotropic polyvinyl methacrylate nanoparticles via interfacial agents. Polymer Chemistry, 13(32), 4625–4633.